

**Determining tissue optical properties with
optical coherence tomography**
A novel approach for improving diagnosis
of tissue pathology

David Levitz

Master's Thesis
Lund Reports on Atomic Physics, LRAP-326
Lund, June 2004

Table of contents

Abstract	4
List of papers	5
1. Introduction	6
1.1 <i>Scope of this thesis</i>	7
1.2 <i>Organization of this thesis</i>	8
1.3 <i>Contribution of author to thesis</i>	8
2. Tissue optical properties	9
2.1 <i>Scattering</i>	9
2.1.1 The scattering coefficient μ_s	9
2.1.2 The scattering phase function and anisotropy factor g	9
2.2 <i>Absorption and the absorption coefficient μ_a</i>	11
2.3 <i>Additional parameters</i>	12
2.4 <i>Scattering regimes</i>	13
3. Modeling an implementation	14
3.1 <i>Previous OCT models</i>	14
3.1.1 The single-scattering model	14
3.1.2 Multiple-scattering models	15
3.2 <i>Our extended Huygens-Fresnel based OCT model</i>	15
3.2.1 Principles and assumptions	15
3.2.2 Final equations from the scattering case only	17
3.2.3 Inclusion of absorption effects	18
3.3 <i>The OCT system</i>	19
3.4 <i>Transforming the model to a computer-based algorithm</i>	20
3.4.1 General order of the algorithm	20
3.4.2 Input and output	22
3.4.3 The old algorithm	23
3.4.4 Physical considerations for extending the algorithm	24
3.4.5 Mathematical considerations for extending the algorithm	26
3.4.6 Making the algorithm user-friendly	27
3.4.7 The new algorithm	28
4. Validation of computer model with phantoms	30
4.1 <i>Epoxy phantoms</i>	30
4.1.1 Recipe	30
4.1.2 Characterization and calibration	31
4.1.2.1 Integrating sphere	31
4.1.2.2 Inverse adding-doubling	32
4.1.3 Comparison with OCT	32
4.2 <i>Numerical phantoms using the Monte Carlo method</i>	34
4.2.1 Why Monte Carlo?	35
4.2.2 Essentials of GMCML	35
4.2.3 Methods and results	36
4.2.4 Discussion	37

Table of contents

Abstract	4
List of papers	5
1. Introduction	6
1.1 <i>Scope of this thesis</i>	7
1.2 <i>Organization of this thesis</i>	8
1.3 <i>Contribution of author to thesis</i>	8
2. Tissue optical properties	9
2.1 <i>Scattering</i>	9
2.1.1 The scattering coefficient μ_s	9
2.1.2 The scattering phase function and anisotropy factor g	9
2.2 <i>Absorption and the absorption coefficient μ_a</i>	11
2.3 <i>Additional parameters</i>	12
2.4 <i>Scattering regimes</i>	13
3. Modeling an implementation	14
3.1 <i>Previous OCT models</i>	14
3.1.1 The single-scattering model	14
3.1.2 Multiple-scattering models	15
3.2 <i>Our extended Huygens-Fresnel based OCT model</i>	15
3.2.1 Principles and assumptions	15
3.2.2 Final equations from the scattering case only	17
3.2.3 Inclusion of absorption effects	18
3.3 <i>The OCT system</i>	19
3.4 <i>Transforming the model to a computer-based algorithm</i>	20
3.4.1 General order of the algorithm	20
3.4.2 Input and output	22
3.4.3 The old algorithm	23
3.4.4 Physical considerations for extending the algorithm	24
3.4.5 Mathematical considerations for extending the algorithm	26
3.4.6 Making the algorithm user-friendly	27
3.4.7 The new algorithm	28
4. Validation of computer model with phantoms	30
4.1 <i>Epoxy phantoms</i>	30
4.1.1 Recipe	30
4.1.2 Characterization and calibration	31
4.1.2.1 Integrating sphere	31
4.1.2.2 Inverse adding-doubling	32
4.1.3 Comparison with OCT	32
4.2 <i>Numerical phantoms using the Monte Carlo method</i>	34
4.2.1 Why Monte Carlo?	35
4.2.2 Essentials of GMCML	35
4.2.3 Methods and results	36
4.2.4 Discussion	37

**Determining tissue optical properties with
optical coherence tomography**
A novel approach for improving diagnosis
of tissue pathology

David Levitz

Master's Thesis
Lund Reports on Atomic Physics, LRAP-326
Lund, June 2004

5. Clinical Studies using the extraction algorithm	39
5.1 <i>Coronary artery disease and atherosclerosis</i>	39
5.2 <i>Intravascular OCT today</i>	40
5.3 <i>Feasibility study</i>	41
5.3.1 Sample handling and imaging	41
5.3.2 Curve-fitting	41
5.3.3 Results and discussion	41
5.4 <i>Endarterectomy study</i>	43
5.4.1 Initial results	44
5.4.2 Discussion	45
5.4.3 Utility of the new algorithm	47
6. Conclusion and outlook	48
6.1 <i>Perspectives</i>	48
Appendix A: Derivation of the OCT signal	49
Appendix B: The extraction algorithm at present	51
B.1 <i>Description of the algorithm</i>	51
B.2 <i>Codes of the extraction algorithm</i>	54
Appendix C: Epoxy phantom recipe	63
Appendix D: GMCML input file	66
Appendix E: A beginner's guide to atherosclerosis	67
E.1 <i>The Endarterectomy procedure</i>	68
Acknowledgements	70
Paper I	71
Paper II	81
References	93

Abstract

We developed a new algorithm that fits optical coherence tomography (OCT) signals as a function of depth to a general theoretical OCT model which takes into account multiple scattering effects. With use of this algorithm, it was possible to extract both the scattering coefficient and anisotropy factor from a particular region of interest in an OCT image. The extraction algorithm was evaluated against measurements from an integrating sphere on a set of tissue phantoms and yielded valid results. Additionally, a preliminary *ex vivo* OCT investigation on human aortic specimen indicated that the algorithm may contribute importantly to differentiation between normal and atherosclerotic arteries.

Following confirmation that our algorithm can be used to extract the optical scattering properties, we then extended the model to include absorption effects. Based on this new model, a novel semi-automatic extraction algorithm was devised that was capable of extracting the absorption coefficient in addition to the scattering properties. This new algorithm was tested on numerical phantoms, and showed that at low albedo values, absorption not only affects the OCT signal but also degrades the accuracy of the extracted scattering parameters. By adding the absorption coefficient as a third fitting parameter, it is possible to reduce these fitting errors introduced by absorption. In testing the new algorithm on carotid plaques, absorption effects were found to have influenced the OCT signal in 13% of the examined regions of interest. These results indicate that in some cases, including absorption effects in curve-fitting may improve the diagnostic utility of the extracted scattering properties.

We are currently working on verifying these assertions by experimentally characterizing new low-albedo epoxy tissue phantoms and conducting a more detailed clinical investigation on carotid plaques.

Based on these results, we conclude that extracting optical properties may facilitate tissue characterization by OCT.

List of Papers

- I. D. Levitz, C. B. Andersen, M. H. Frosz, L. Thrane, P. R. Hansen, T. M. Jørgensen, and P. E. Andersen "Assessing blood vessel abnormality via extracting scattering properties from OCT images" in European Conference in Biomedical Optics (ECBO), W. Drexler, ed. Proc. SPIE **5140**, 12-19 (2003).
- II. D. Levitz, L. Thrane, M.H. Frosz, P. E. Andersen, C. B. Andersen, J. Valanciunaite, J. Swartling, S. Andersson-Engels, and P. R. Hansen. "Determination of optical scattering properties in highly-scattering media in optical coherence tomography images". Opt Expr. **12**, 249-259 (2004).

1. Introduction

Over the last few decades there has been a continuing search for high-resolution imaging modalities that can quickly and accurately measure the optical properties of layered tissue *in vivo*. Here, the optical properties of interest are those that primarily guide light transport inside the tissue, namely, the scattering coefficient μ_s , the anisotropy factor g , and the absorption coefficient μ_a [1]. A valid method with which these measurements can be done have many important biomedical implications, such as identifying vulnerable atheromatous lesions during percutaneous coronary interventions [2] or distinguishing a tumor from the surrounding healthy tissue for photodynamic treatment [3].

Many high-resolution optical imaging technologies (i.e., microscopy) have one major drawback- a tradeoff between the axial and transverse resolution, both of which are controlled by the numerical aperture of the optical system. Additionally in these systems, light scattering is considered an impediment to image quality. One new high-resolution technology where this tradeoff may be overcome is optical coherence tomography [4]. Optical coherence tomography (OCT) is an imaging modality that is analogous to ultrasound pulse-echo imaging [5], except light is tomographically scanned instead of sound. And contrary to microscopy, in OCT light scattering is vital for imaging of tissue microstructures.

The principle driving OCT is low-coherence interferometry, where an interference signal can arise only if the pathlength difference between light returning from two arms of a Michelson interferometer is within the temporal coherence length of the source [6]. In OCT, the axial resolution Δz is defined as $\Delta z = (2 \ln 2 / \pi) \times (\lambda_c^2 / \Delta \lambda)$, where λ_c is the center wavelength and $\Delta \lambda$ is the 3 dB bandwidth of the source*. Thus, with a broadband source it is possible to attain axial resolutions on the micrometer scale. Changing the delay in the reference arm enables probing different depths in the sample; tomographically translating the sample arm provides a non-invasive† cross-sectional map of light backscattered or backreflected from the probed medium. Importantly, in OCT the axial and lateral resolutions are independent of one another.

The basic OCT setup (see Figure 1) consists of a broadband light source, a fiber optic Michelson interferometer, a photodetector, and some signal processing electronics. Light from the source is split at a 50/50 fiber coupler and is guided to the reference and sample arms, respectively. In the reference arm light is retroreflected off of a scanning mirror providing the delay. The sample arm consists of a laterally scanning optics that focuses the beam on the sample. Light from both arms is recombined at the coupler and is relayed to a photodetector. An electronic signal emerges from the photodetector that is then amplified, filtered, digitized, and stored on a computer [4]. Technological advances in sources [7], scanning optics [8], and computers enable real-time imaging at up to 38 frames per second [9]. And because the sample arm unit is fiber-based, OCT can be readily integrated into catheter-based endoscopic applications [10].

* A Gaussian source spectrum is assumed for this relation to hold.

† The term ‘non-invasive’ is only relative, describing the nature of light-tissue interaction. Some applications of OCT (i.e., intravascular imaging) are implicitly invasive.

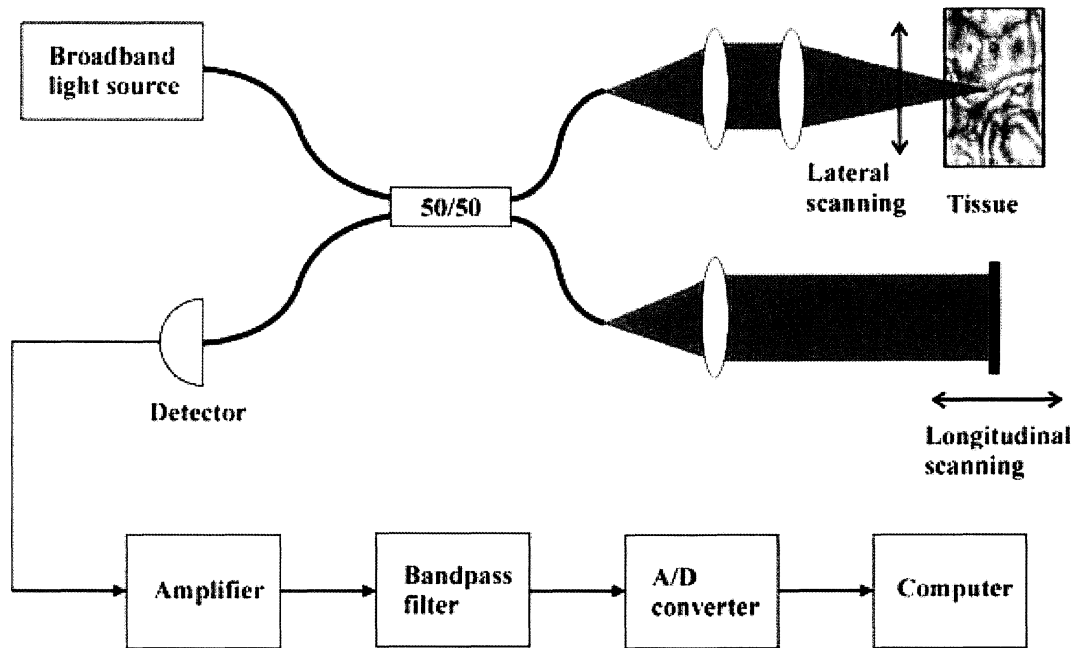


Figure 1: The generic OCT setup.

Still, OCT does have certain limitations. One major drawback of the technique is its short penetration depth (2 mm at best), although the negativity of this aspect varies between applications. Another limitation is speckle, an insidious form of noise that always accompanies coherent imaging systems and degrades image quality [11]. However, the obstacle that probably prevents OCT from being integrated into many clinical procedures remains a lack of objective interpretation of tissue morphology in OCT images. When clinicians look at optical coherence tomograms, they are not sure what exactly they are seeing. Although there have been studies correlating OCT with histopathology, for the average clinician at present objective characterization of tissue by OCT is not yet feasible.

To address this problem, our group has opted for an alternative approach. Consider: OCT signals are mainly influenced by the optical properties of the examined sample. These are macroscopic physical properties unique to the tissue, which play a vital role in the modeling of OCT signals. By properly modeling an OCT signal as a function of depth so that multiple scattering events are included, and fitting the depth profile of coherent backscattered light in an OCT image (also called depth-scan or A-scan) to such model, it is possible to extract out μ_s , μ_a , and g . The principal aim of this thesis is to present this novel new method by which optical properties data can be extracted from OCT images.

1.1 Scope of this thesis

To move a technique from the research lab to the clinic, certain issues need to be resolved and milestones met. For the extraction algorithm, these issues and milestones include: Proper modeling, creating a user-friendly and scientifically valid algorithm, testing the algorithm on phantoms, and proving feasibility and safety on real tissues in patients. And while in many medical fields OCT has not yet gained clinical acceptance, we believe that improving the extraction technique and

demonstrating its ability to diagnose tissue pathology will greatly assist OCT in advancing towards this goal.

This thesis deals primarily with validating the technique of extracting optical properties from tissues, and considers all the aspects needed to do so correctly. As this research is still a work in progress, not all the experiments have been completed and some of the results are as of yet not published. Parts of experiments that remain to be carried out are pointed out; the remainder of the work should be completed in the summer of 2004.

The research for this thesis was conducted at Risø National Laboratory, Denmark, and in the Physics Department at Lund University, Sweden during a year and a half of studies from the spring 2003 to the spring 2004 semesters. Of note, this research is a team effort, and other members of the group contributed to this work. As a consequence, not all the work presented here is original work by the author, and unpublished work by colleagues and collaborators is properly noted throughout the thesis.

1.2 Organization of this thesis

The work in this thesis is organized as follows: Chapter 2 gives a review of the tissue optical properties and specifically defines the terminology used in this thesis. Chapter 3 presents the theoretical modeling used in this investigation, first neglecting and then including bulk tissue absorption. Also explained is the manner in which these models were transformed into a computer-based algorithm that extracts optical properties, and which steps were taken to semi-automate the algorithm. A discussion regarding validating the algorithm experimentally and numerically is found in Chapter 4, presented with results that establish this point. In Chapter 5 the extraction technique is applied on postmortem aortic and excised carotid biopsies, and its results are presented and utility assessed. Finally, a conclusion is given in Chapter 6.

1.3 Contribution of author to thesis

The author contributed to this research effort as follows: In Chapter 3, the author took the initial extraction algorithm written by Michael H. Frosz, reprogrammed it to include absorption effects, and semi-automated it. In Section 4.1, the author carried out part of the integrating sphere experiments and subsequent analysis. Also in Section 4.1, the author imaged the phantoms, performed the Mie calculation, and processed that data. The author ran the Monte Carlo simulations, and carried out related fits and analyzed the results in Section 4.2. As for Chapter 5, the author did practically all of the imaging and fitting, as well as summarize the data into a presentable form.

2. Tissue optical properties

Tissue is a turbid medium, characterized by many small random fluctuations in refractive index caused by the ultrastructure of the tissue, i.e., by cells and organelles. As a consequence of these refractive index fluctuations, light incident on tissue is deflected or scattered off these particles. Additionally, tissue also contains chromophores, molecules that can absorb incoming photons. Because these scattering particles and chromophores are complexly distributed in the tissue, describing the interaction between light and tissue can be a rather laborious task on the microscopic level. However, by making some assumptions on the macroscopic level, some general observations can be made to amply characterize the turbid medium. Below a review of scattering and absorption of light in tissue is given.

2.1 Scattering

Scattering is the most common event that will occur when tissue is illuminated with light. It is caused by small local variations in the mean real refractive index n_R of the medium (note refractive index n is complex). Mathematically, a local real refractive index n_R can be expressed as $n_R = \langle n_R \rangle + n_{Rf}$, where $\langle n_R \rangle$ is the mean refractive index of the medium and $n_{Rf} (\ll 1)$ is a small fluctuating local variation. This approximation has been found to be generally valid for tissue [12].

There are two general theories that describe light scattering by a single particle, whose validity is determined by the wavelength of the incident light and the size of the particle. The particle is assumed to be spherical, the only shape with an exact solution to the scattered electromagnetic field/energy* [1]. When the sphere is approximately the same size scale as the wavelength of the incident light, the scattering is best described by Mie theory and is often called Mie scattering. On the other hand, when the size is much smaller than the wavelength of the incident light, the scattering may be characterized by the Rayleigh approximation to Mie scattering, which is frequently referred to as simply Rayleigh scattering. For the case of tissue where the scattering structures are on the μm scale, Mie scattering dominates.

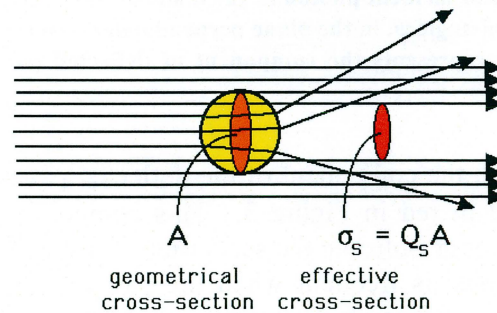


Figure 2: Pictorial definition of the effective scattering cross-section σ_s and scattering efficiency Q_s from [14].

2.1.1 The scattering coefficient μ_s

Considering a case where light is incident on a spherical particle with geometrical cross-sectional area A [L^2] (see Figure 2), an effective scattering cross-section σ_s [L^2] can be defined as $\sigma_s = Q_s \times A$, where Q_s [dimensionless] is the scattering efficiency [14]. For a volume where many such particles are homogeneously distributed, a

* Note an exact solution for the energy scattered off an infinitely long cylinder also exists

scattering coefficient is then defined as $\mu_s = \rho_s \times \sigma_s$, where ρ_s represents the density of particles per volume [L^{-3}] and μ_s has a units of [L^{-1}] [1,14]. The scattering coefficient can also be thought of as the reciprocal of the average distance a photon travels between scattering events. Note that while the scattering cross-section σ_s is a microscopic property of a particle, the scattering coefficient μ_s is a macroscopic average of a medium.

2.1.2 The scattering phase function and anisotropy factor g

Additionally, the direction of the scattered field can also be characterized. Consider light incident on a scattering particle as shown in Figure 3. The directionality of the scattered wavefront can be characterized by angles θ and ψ , in the plane of the paper and perpendicular to it, respectively. For a spherical particle, one can assume symmetry over the azimuthal angle ψ , measured over 2π radians [1]. The in-plane deflection angle is slightly more complicated; a function $p(\theta)$ * defines the distribution of the energy in this plane over π radians [1,14]. The function $p(\theta)$ is called the scattering phase function, and is often normalized such that $\int_0^\pi p(\theta) 2\pi \sin \theta d\theta = 1$.

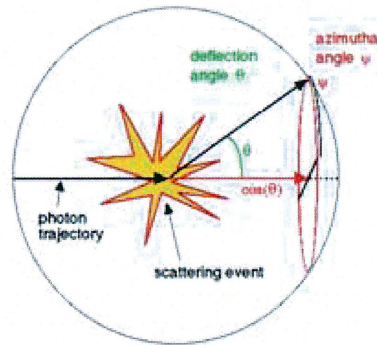


Figure 3: Graphical description of a scattering event. The deflection angle θ is formed between the paths of the scattered and incident photon in the plane of the paper. Deflection is considered independent over azimuthal angle ψ , in the plane perpendicular to the incident photon path. The red arrow denoted $\cos(\theta)$ represents the component of deflected path in the direction of the original photon. From [14].

Since $p(\theta)$ is normalized, the component of the deflected path parallel to the incident path is $\cos(\theta)$, labeled in red in Figure 3. This component is important, since it describes how isotropic or anisotropic the scattering is. Isotropic scattering, i.e., equal scattering in all directions, is frequent when the particle is much smaller than the wavelength of light as in Rayleigh scattering. With a large particle size however, scattering tends to be rather anisotropic, that is, most of the scattered energy is in the forward direction [1]. Additionally, one can also define the anisotropy factor g (also called asymmetry parameter or simply g -factor) as the expectation value of $\cos(\theta)$, or $g = \langle \cos(\theta) \rangle$, where the angular brackets denote ensemble averaging over π radians. $g = 1$ indicates all the scattering is in the forward direction. This definition of g is very

* In the literature, $p(\theta)$ is sometimes denoted $p(s,s')$, i.e., the scattering phase function from direction s into direction s' , or $p(\cos(\theta))$ to denote the angular dependence. In the definition used here, θ is only in the plane of the paper.

common in the literature [1,13]; however, the exact definition of anisotropy will be reconsidered below.

Performing exact manual calculations of the scattering phase function is rather cumbersome in practice. A code in FORTRAN is given in Reference [1], which performs a Mie calculation of the energy distribution off a spherical particle and is available on the internet, see Reference [14]. Here, the sphere size and refractive indices of sphere and surroundings are user-defined. The output from this code will be taken as the “literature value” in the discussions below.

There are short and simple approximations to the scattering phase function $p(\theta)$. One such simplification is called the Henyey-Greenstein function, originally used for describing light scattering in the atmosphere by clouds and dust, but since adapted for tissue optics. While other scattering functions exist, this function is widely used in many places in the literature [1,13]. The function is

$$p(\theta, g) = \frac{1}{4\pi} \frac{1 - g^2}{(1 + g^2 - 2g \cdot \cos(\theta))^{3/2}}, \quad (1)$$

where g is the anisotropy factor as defined above.

In this thesis however, scattering is defined otherwise; scattering is assumed to be only forward-directed, characterized by a root-mean-square scattering angle θ_{rms} . The bulk backscattering is neglected, and is instead modeled as a diffuse reflection (more on this in Chapter 3). θ_{rms} is the half-width at 1/e maximum of a Gaussian fit to the main frontal lobe of the scattering phase function as determined by a Mie calculation [15]. The resulting expression for the scattering phase function is then [16]

$$p(\theta) = c_n \exp\left(-\left(\frac{\theta}{\theta_{rms}}\right)^2\right), \quad (2)$$

where c_n is a normalization constant. An example is given in Figure 4, where both the Gaussian and Henyey-Greenstein approximations are compared to a Mie calculation done with the code in Reference [1]. It is clearly seen that at small angles, the Mie calculation closely resembles a Gaussian function, but that at larger angles the Henyey-Greenstein appears to be a better match. An effective anisotropy parameter g_{eff} can then be defined as $g_{eff} = \cos(\theta_{rms})$. In tissue, $g_{eff} > g$. One should be careful as to not confuse g and g_{eff} in the subsequent chapters, for it is g_{eff} and θ_{rms} that are used in the OCT modeling and thus in the remainder of this thesis.

2.2 Absorption and the absorption coefficient μ_a

Certain molecules found in tissues called chromophores absorb light if it is at the correct wavelength. Absorption is a complicated process, and generally speaking, for absorption of electromagnetic energy to occur, the frequency of the light generally needs to match an atomic or molecular frequency. There are many types of transitions that result in absorption, most of which are beyond the scope of this thesis. A more detailed discussion of the behavior of chromophores is given in Reference [17].

Comparison of Gaussian and Henyey-Greenstein phase functions to Mie Calculation

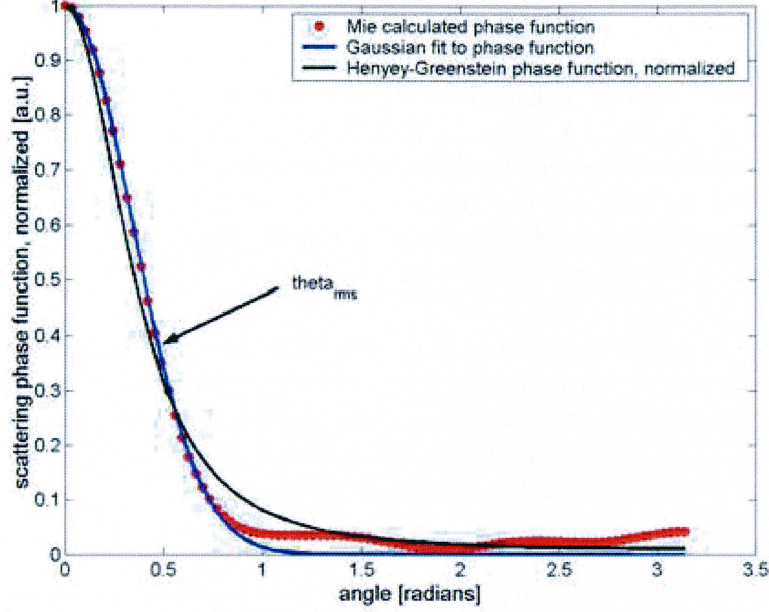


Figure 4: A comparison of the Henyey-Greenstein and Gaussian approximations to the scattering phase function as determined with a Mie calculation for 1 μm spherical TiO_2 particles embedded in epoxy. Note that in the main frontal lobe, the Gaussian fit (blue) is almost identical to the Mie calculation, but that at larger angles it is not. The corresponding Henyey-Greenstein function (black) does not match the Mie calculation as well. θ_{rms} is defined at the HWe^{-1}M angle.

Analogous to the scattering case for a sphere, an effective absorption cross-section σ_a [L^2] can be defined, related to the geometrical cross-section by the absorption efficiency Q_a [dimensionless] [1]. Likewise, in the macroscopic case the absorption coefficient μ_a [L^{-1}] can be defined as $\mu_a = \rho_a \times \sigma_a$, where ρ_a is the density of absorbers in the medium [L^{-3}]. And while scattering effects are caused by fluctuations of the real refractive index, absorption is caused by a negative imaginary component to the refractive index, i.e., $n = n_R - in_I$. In electromagnetic theory the absorption coefficient has been defined as $\mu_a = 2k \times n_I$ [18]. It is through the complex refractive index that absorption effects have been included in the OCT modeling [19].

2.3 Additional parameters

Aside from μ_s , g , and μ_a , there are some other parameters that can be used to describe turbid media such as tissue and are relevant in this thesis. First is the total attenuation coefficient μ_t [L^{-1}], which defined as $\mu_t = \mu_s + \mu_a$. Because in general $\mu_s \gg \mu_a$, one can approximate $\mu_t \cong \mu_s$. The unscattered and unabsorbed component of the light can also be called the ballistic component. The inverse of μ_t is called the mean free path, which is the average distance a photon travels between scattering or absorption events.

One more tissue optical property to describe that is used at times in the literature, and the backscattering coefficient μ_b [L^{-1}]. It measures how much light is scattered back in the direction opposite to the initial photon trajectory, i.e., $\mu_b = \mu_s(\pi)$ [1]. This parameter has been used in some earlier OCT models and curve fitting studies [20,21]. However, μ_s values are more readily available in the literature.

Finally, two more dimensionless parameters that are useful are the optical depth and albedo. The optical depth τ is defined as $\tau = \mu_t \times z$, where z is the distance traveled by the beam. It is a measure of how much of the turbid medium the light has traversed. The albedo a is a ratio of the scattering coefficient to the total attenuation coefficient, i.e., $a = \mu_s / (\mu_s + \mu_a)$. Albedo values close to unity indicate that the scattering is much greater than the absorption, as is frequently the case with tissue.

2.4 Scattering regimes

The optical depth described above in the previous subsection is also a measure of how light is transported in the medium. Assuming that $\mu_t \cong \mu_s$ as above, light that has traversed an optical depth below unity ($\tau < 1$) in the medium is said to be in the single-scattering regime, that is, detected photons have only undergone a single scattering event or less. For the case where $1 < \tau < 10$, the light is said to be in the multiple-scattering regime, meaning that light has undergone several scattering events before being detected. OCT signals are predominantly made up of light from the single- and multiple-scattering regimes, and each regime is characterized differently in OCT modeling and results in a different shape of the OCT signal. For completeness, above the limit where $\tau > 10$, light is said to be in the diffusion regime, meaning that light travels through the medium by means of a random walk [13]. Of note, these regimes are not sharply delineated, and there are ‘transition periods’ in optical depths near one and ten.

3. Modeling and Implementation

This is the chapter that connects previous work to the research carried out in this thesis. It begins with a review of the theoretical modeling of the OCT signal that was used to extract optical properties, both by others (Section 3.1) and by our group (Section 3.2). A description of the OCT system modeled is given in Section 3.3. The principal focus of this chapter (Section 3.4) concerns translating this model from a theoretical description to a semi-automated computer-based algorithm that extracts the optical properties from a particular region of interest in an OCT image.

In this thesis there are two described models that were translated into extraction algorithms, one neglecting absorption effects [22] and one including them [19]. Thus, Section 3.4 begins with a discussion of algorithms used for extractions in the broader sense. It then describes the old algorithm (by Michael H. Frosz), which was the ‘starting point’ for this thesis, explaining what needed to be improved altogether and what could be improved at the moment. Moreover, it considers the optimization process on both the mathematical and physical levels. In the last part of Section 3.4 the new algorithm is given and its practicality is assessed.

3.1 Previous OCT models

Over the years, there have been a plethora of theoretical OCT models [20-27], all aimed at improving our understanding of light-tissue interaction as well as system optimization to improve image quality. The first models were based on single-scatter theory [20,21]; subsequent models that explored multiple-scattering were based on experimental analyses [23], solving the radiative transport equation using small angle approximation [24], a linear systems theory analysis [25], Monte Carlo simulations [26], and modeling using the extended Huygens-Fresnel principle [22,27]. What these previous models omitted was the shower curtain effect [28,29] and its influence on the OCT signal; indeed, this is the novelty with our model [22]. Moreover, to our knowledge, no model describing the effects of absorption on the OCT signal has been published, and work presented in Section 3.2.3 represents the first novel steps taken in this direction. Note that our model employed extended Huygens-Fresnel formalism [30] and will be denoted the EHF model below, and that the term ‘EHF model’ covers both schemes in the absence and presence of absorption effects.

Our aim in this section is to review models that were used to extract optical properties and their relative successes and shortcomings. This forms the basis of discussions in the next two subsections, divided into single-scattering and multiple-scattering theories.

3.1.1 The single-scattering model

Single-scattering theory is, as the name indicates, only valid in the single-scattering regime that is found in superficial tissue layers. In this model the detected OCT signal is entirely made up of ballistic photons that underwent a single backscattering event in the tissue and returned to the photodetector, which requires that the optical depth be under unity. For such shallow depths, the OCT signal as a function of depth is proportional to $\exp(-2 \times \mu_t z)$ and is characterized by a steep slope [20,21]. Hence, extractions can be made to obtain μ_t utilizing a linear regression to which the log of the OCT signal is fit. Also included in the model is the aperture function that accounts for focusing and the backscattering contribution [20,21]. In fact, the μ_b has

also been fitted as a second parameter* [20,21]. Given today's understanding of multiple-scattering, this may seem simplistic; nonetheless, it was an important first step towards the work described in this thesis.

3.1.2 Multiple-scattering models

It soon became apparent that multiple-scattered light contributed to the OCT signal, and a model that can effectively characterize the OCT signal in both the single- and multiple scattering regimes was sought after. As shown by previous studies [22-27], multiple-scattering lessens image contrast and the resolution of the system, causing only a moderate decline in signal at large depth as opposed to the sharp decline in the single-scattering regime. Of all these multiple-scattering models, only two are used for extractions: the radiative transport model [24] used by the Nizhny Novgorod group and the extended Huygens-Fresnel model [22] used by our group.

The group in Nizhny Novgorod has made significant advances in extractions [31]. Topping their list of accomplishments is an algorithm that can extract the scattering coefficient and a scattering directionality parameter by defining a window with the mouse, and implementing it to diagnose cervical cancer in patients [31]. Moreover, their algorithm (which takes seconds to run) can handle two-layer geometry. Their primary limitation is that the model they use [24] is cumbersome and is restricted in its ability to handle complex geometries. Also vague is exactly how the focusing conditions were modeled and implemented [31]. Nonetheless, their progress in this field is taken as another indication that extracting optical properties is a promising functional OCT technique.

3.2 Our extended Huygens-Fresnel based OCT model

This section provides an overview of our OCT modeling scheme. It begins by describing some of the principles on which the modeling is based, and presents the key equations used by the extraction algorithm. A derivation for these equations is found in Appendix A, for a detailed version the reader is referred to References [22, 32]. Additionally, an extension of the model used for extraction in the first part of this thesis to include absorption effects [19] is given.

3.2.1 Principles and Assumptions

What drives this entire model is the extended Huygen-Fresnel (EHF) principle [30], which describes the amplitude and phase fluctuations of an electric field propagating through a medium characterized by small random refractive index changes. As implied by the name, the EHF principle states that the field emanating from a complex aperture can be calculated in the far-field by superimposing point sources radiating spherical wavelets over the whole aperture [30].

Translating this principle to the OCT sample arm geometry of interest (see Figure 5), consider a lens of focal length f probes a tissue discontinuity arising from a (real) refractive index mismatch at a depth z inside the tissue that is a distance d away from the lens. The diffusely backreflected beam is the 'aperture' described in the previous paragraph. Rotational symmetry of the sample arm is assumed. Furthermore, the delay in the reference arm matches optical path lengths with the focal plane that

* This should be viewed with caution because in most tissues $\mu_t \approx \mu_s$ and $\mu_b = \mu_s (\pi)$ [1], thus both parameters actually relate back to μ_s .

coincides with the tissue discontinuity. For simplicity, the mixing plane is presumed to be directly in front of an infinitely long lens plane. Note that polarization effects are not included.

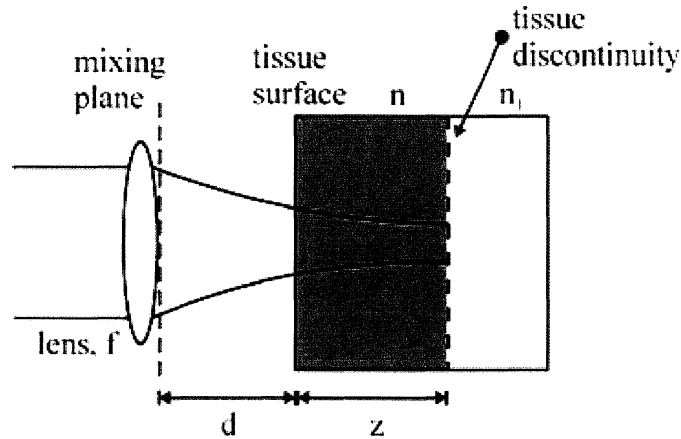


Figure 5: The sample arm geometry of the OCT system.

In the wavelength region of interest, scattering in tissue (i.e., skin^{*}) is predominantly in the forward direction [33]. Put in another way, the rms scattering angle θ_{rms} of tissue in the wavelength of interest is typically small, i.e., $\theta_{\text{rms}} < 0.5$ radians or 30° , and thus $g_{\text{eff}} > 0.877$. This assumption states that light propagates in tissue at small angles with respect to the optical axis, i.e., tissue can be described as a paraxial optical system. The sample arm geometry being within the paraxial approximation is a crucial assumption for ensuing analyses in this thesis[†]. Moreover, light propagation through paraxial systems is frequently described using ABCD matrices [34]. ABCD formalism is particularly advantageous because it can be rather easily applied to multiple-layer geometry, such as is frequently the case with tissue.

A final note in this subsection concerns the focusing in the sample. Normally, OCT systems employ focusing in the sample arm to attain a high lateral resolution. In general there are two types of focusing schemes, a fixed focus and dynamic focusing. Dynamic focusing means that the focal plane is matched with the discontinuity plane, resulting in optimal lateral resolution for all probing depths z . Fixing the focal plane on, i.e., the surface of the tissue, requires less moving components and is easier to implement experimentally. Because ABCD formalism is used here, the focusing conditions affect the B element. Specifically, for a lens with focal length f , $B = f$ for dynamic focusing and $B = f + z / n_R$ for light focused on the tissue surface. While fixed focusing is used in our experimental setup (Section 4.1 and Chapter 5), dynamic focusing is used in our numeric Monte Carlo simulations (Section 4.2). The ability to handle both focusing conditions with such ease is yet another advantage of our robust modeling scheme [22].

^{*} Of note, the predominant molecule that gives rise to scattering in both skin and the superficial arterial wall is collagen.

[†] In case where $\theta_{\text{rms}} > 0.5$, this model serves as a good first order approximation to light propagation through the tissue.

3.2.2 Final equations from the scattering case only

This section presents the modeling outcomes from our established model [22], and details the equations used in the extraction algorithm [35]. Note that in this subsection absorption effects are neglected. Of primary interest is the mean square heterodyne signal current $\langle i^2(z) \rangle$, defined as

$$\langle i^2(z) \rangle = \langle i^2 \rangle_0 \Psi_S(z) = \frac{\alpha^2 P_R P_S \sigma_b}{\pi w_H^2} \left[e^{-2\mu_S z} + \frac{4e^{-\mu_S z} [1 - e^{-\mu_S z}]}{1 + (w_S^2 / w_H^2)} + (1 - e^{-\mu_S z})^2 \frac{w_H^2}{w_S^2} \right]. \quad (3)$$

Here $\langle i^2 \rangle_0$ (the fraction in front) is the mean square heterodyne signal current in the absence of scattering, and $\Psi_S(z)$ (in the square brackets) is the heterodyne efficiency factor describing the signal degradation due to the scattering (note $\Psi_S(z) \neq \Psi_{SA}(z)$, which includes absorption effects). $\Psi_S(z)$ is divided into three terms, the first representing the contribution from single-scattering, the third being the multiple-scattering term, and the second the cross term. This model is valid for both single- and multiple-scattering regimes, and can therefore be used to extract both the scattering coefficient and the effective anisotropy factor via θ_{rms} .

Also, P_R and P_S are the power of the reference and input sample arm beams, α the power to current conversion ratio, σ_b the backscattering cross-section, and w_H and w_S the 1/e irradiance radius at the probing depth in the absence and presence of scattering, respectively*. More precisely, w_H and w_S are defined as

$$w_H^2 = w_0^2 \left(A - \frac{B}{f} \right)^2 + \left(\frac{B}{kw_0} \right)^2, \text{ and} \quad (4)$$

$$w_S^2 = w_0^2 \left(A - \frac{B}{f} \right)^2 + \left(\frac{B}{kw_0} \right)^2 + \left(\frac{2B}{k\rho_0} \right)^2. \quad (5)$$

The quantity w_0 represents the 1/e intensity radius of the sample arm beam incident on the lens plane, and A and B are ray matrix elements. A derivation of the lateral coherence length ρ_0 [22,36] shows that

$$\rho_0 = \sqrt{\frac{3}{\mu_S z}} \frac{\lambda}{\pi \theta_{rms}} \left(1 + \frac{n_R d(z)}{z} \right). \quad (6)$$

The factor on the right, at times denoted $(n_R \times B / z)$, is the so-called ‘shower curtain effect’[†] [28,29], a significant effect omitted from previous OCT models [20,21,23-27]. More details are available in Appendix A and in Reference [22].

* Strictly speaking, w_H is the 1/e beam waist unaltered by neither scattering nor absorption effects.

[†] The shower curtain effect [28,29] states that the lateral coherence length increases if the scattering medium is closer to the source than the observer. This is the case here; the diffusely reflecting discontinuity is considered a point source embedded in the turbid medium and observing is done in the lens plane, which is a distance d away from the medium, see Figure 5. The physical reason giving rise to this effect is that a distorted spherical wave approaches a plane wave as it propagates through a nonscattering medium (i.e., the air between the lens and the tissue). Of note, in the case of a specular reflection the wavefront would be nonspherical and thus ρ_0 would be different.

The above four equations constitute the model used in our old fitting algorithm. It should be pointed out that the calculation of the OCT signal was carried out from closed-form expressions, which is another major advantage of our extraction algorithms: The measured depth-profile may be fitted to a closed-form expression, thereby reducing computational burden.

3.2.3 Inclusion of absorption effects

This section describes modeling the effects that absorbing media have on optical coherence tomography systems. The bulk of the work presented here is unpublished at the moment carried out by Hal T. Yura of the Aerospace Corp., USA and Lars Thrane of Risø National Laboratory, Denmark. It is presented for completeness, as a large portion of this thesis has been dedicated to validating this new model by using it to extract optical properties.

To extend the model to include absorption effects, the imaginary component of a complex refractive index n ($n = n_R - in_I$) need to be accounted for, where $n_I = \mu_a / 2k$ [18]. In general, the derivation is quite similar to the above case neglecting absorption, with a few minor differences mentioned in Appendix A. The ABCD system in question is no longer real and the B element becomes complex. In both dynamic and fixed focusing*, $B = d + z / n$; also, in dynamic focusing, $\text{Re}[B] = f$ [19].

Performing the integration in Equation (13) in Appendix A yields a long and unpleasantly looking equation. Some additional indispensable simplifications are: For all practical OCT systems, $d \sim f \sim 10$ mm, 0.1 mm $\leq w_0 \leq 1.0$ mm, $z \leq 1.0$ mm, and $\text{Re}[k] \gg \mu_a \leq 1$ mm⁻¹. As a consequence, first order μ_a terms are much greater than second order μ_a terms [19]. The ensuing equation for the heterodyne efficiency factor Ψ_{SA} that includes absorption effects is

$$\Psi_{SA} = e^{-2\mu_a z} \left[e^{-2\mu_a z} + \frac{4e^{-\mu_a z} (1 - e^{-\mu_a z})}{(1 + \mu_a \Delta z_D)(1 + w_{SA}^2 / w_H^2)} + \frac{(1 - e^{-\mu_a z})^2 w_H^2}{(1 + \mu_a \Delta z_D)^2 w_{SA}^2} \right], \quad (7)$$

where (below $B \equiv \text{Re}[B]$ and $k \equiv \text{Re}[k]$):

$$w_{SA}^2 = (1 + \mu_a \Delta z_D)^{-1} \left[w_0^2 \left(A - \frac{B}{f} \right)^2 + \left(\frac{B}{kw_0} \right)^2 + \left(\frac{2B}{k\rho_0} \right)^2 (1 + \mu_a \Delta z_N) \right], \quad (8)$$

$$\Delta z_N = \frac{z(w_0^2 + \rho_0^2 / 2)}{4n_R^2 B^2}, \text{ and} \quad (9)$$

$$\Delta z_D = \frac{z}{2n_R^2} \left[\left(\frac{w_0}{f} \right)^2 + \left(\frac{1}{kw_0} \right)^2 + \left(\frac{2}{k\rho_0} \right)^2 \right]. \quad (10)$$

Note that the beam waist in the absence of scattering and absorption w_H and lateral coherence length remain unchanged from the non-absorbing case and are given by Equations (4) and (6), respectively. The quantity w_{SA} is the beam waist in the

* If the beam was focused on the tissue surface, $B = f + z / n$. The formula given above holds for an arbitrary focal plane.

presence of both scattering and absorption. Δz_N and Δz_D are nameless quantities at the moment, describing how absorption affects off-axis beam propagation.

Upon close examination, it can be discerned that $\Delta z_D > \Delta z_N$, indicating that $w_{SA} < w_S$ and $\Psi_{SA} < \Psi_S$ at large optical depths. It is the relatively small reduction on the heterodyne efficiency factor from these equations that governs the second algorithm described in later sections. This is in theory; in practice the difference is often negligible. In other words, a low-albedo medium is necessary for absorption effects to have a noticeable influence the OCT signal, as indeed was expected. Because the effect is so small, extracting two parameters should at times adequately characterize the tissue. Still, it is our intention to show that in those cases where absorption effects do influence the OCT signal, extracting μ_a may improve the diagnostic value of the fitted μ_s and g_{eff} .

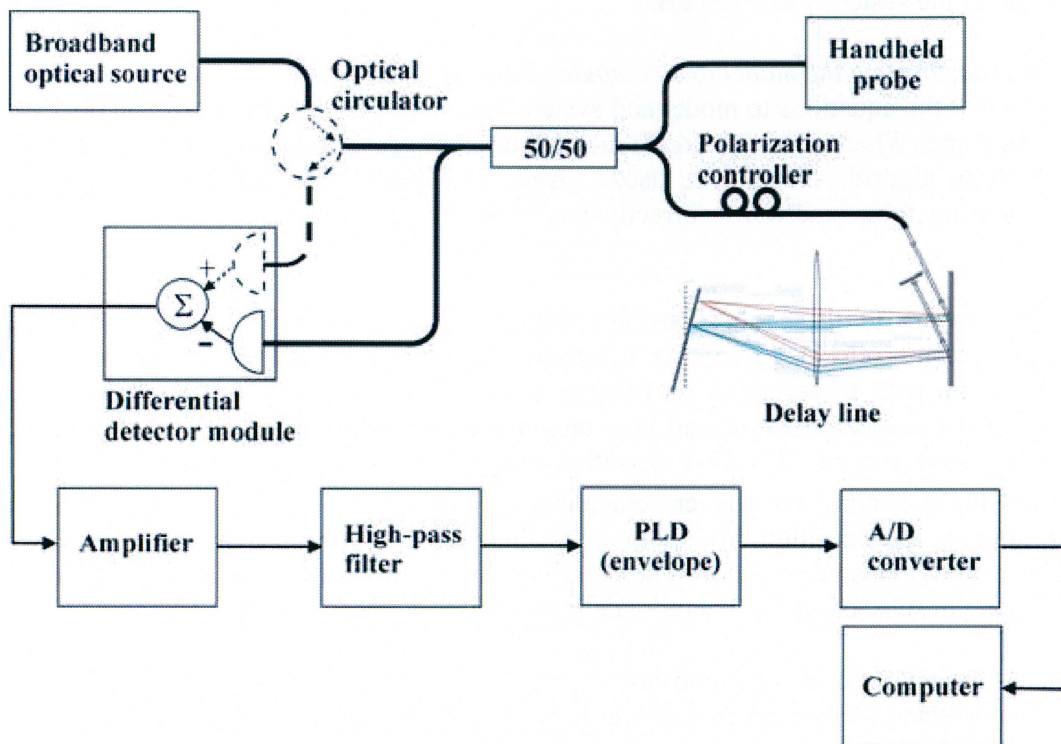


Figure 6: The OCT system. The optical circulator and a second detector (dashed line) were only used in some parts of the study. PLD: programmable logic device. From [35].

3.3 The OCT system

The OCT system used for this study and modeled in the extraction algorithms is shown in Figure 6 and explained here. It employed a broadband source with a center wavelength of 1300 nm (AFC, Inc., model BBS 1310), providing a subsequent axial resolution of $\sim 10 \mu\text{m}$ in tissue. The sample arm unit consisted of a handheld probe that the user holds in contact with the sample. A computer controlled transverse scanning module and an integrated digital video camera were incorporated into the probe unit. The digital video camera was used to visually assist transverse scanning. In the reference arm, fast scanning was achieved with use of a Fourier domain rapid-scanning optical delay line [8]. An InGaAs (New Focus, Inc., model 2017) detector measured the interference pattern between the two arms of the interferometer. During some parts of the study (August 2003- present), an optical circulator between the

source and the 50/50 beam splitter was included in the setup, which was also connected to a second detector to allow for dual balanced detection that increased signal-to-noise ratio (SNR) [37]. The electronic signal emerging from the detector was amplified and high-pass filtered. Detection of the interferometric envelope was implemented in hardware using a programmable logic device. Thereafter, the signal was digitized and stored on a computer.

The OCT system was used to capture depth interferometric information from the investigated samples resulting in images with 690 axial (z) pixels (4.16 μm spacing) and 400 transverse (x) pixels (10 μm spacing). In all the images, the probing beam ($w_0 = 0.8$ mm) was focused ($f = 16$ mm) on the surface of the scattering medium. These values served as constants in the algorithm. Corresponding digital photographs of the sample and the scanned region were automatically taken along with every OCT image. Image acquisition time from start of scanning was 5-6 seconds. The dynamic range of the system was >100 dB.

3.4 Transforming the model to a computer-based algorithm

Now that the equations to model and system parameters have been given, the difficult tasks come: What needs to be done in order to obtain data points to fit on? What type of fitting algorithm should be used? And how should the results be interpreted? Answering these questions correctly has been the primary challenge of this thesis work.

The answers to these questions are found in the subsections below, which are organized as follows: First is an illustrative physical overview of our curve-fitting algorithm, with a discussion on relating the physics with Matlab codes*. Next the essential variables involved and how they are used to relay information between the codes are discussed. The first algorithm that fits μ_s and g_{eff} is then described, with areas for potential improvement elucidated. Following this are two subsections on optimizing the algorithm, from both the mathematical and physical perspectives. User friendliness is also discussed. A summary of the new algorithm and its improvements is found in subsection 3.4.7; a more detailed review is found in Appendix B.

3.4.1 General order of the algorithm

To understand the engineering task at hand clearly, one needs to dissect the problem. In other words, given:

- An OCT image and
- A theoretical model describing OCT signals

What are the optical properties of the sample at a given point?

Seems simple enough: These optical coherence tomograms are composed of individual A-scans, which are described by the theoretical model. All that is needed are the values of the constants, the position representing the surface of the medium, and then fitting could be done on the subsequent pixels, right? Well...

* In principle, this thesis work could have been done in any programming language; Matlab was chosen because of its relative robustness and user-friendliness. While many programming issues discussed below are Matlab-related, every programming language has its drawbacks and some problems would inevitably arise.

First, a key point to remember: The optical properties μ_s , g_{eff} , and μ_a are macroscopic properties, or in other words, an average over a certain volume. The cross-sectional area covered by a single A-scan approaches the order of the wavelength, and optical properties of volumes this small lose meaning without some spatial (i.e., lateral) averaging. Defining a volume with homogeneous optical properties in the image is hence of utmost importance. Such a task is not at all trivial; tissue is quite heterogeneous and often layered and in some complex geometry, thus delineating the volume both laterally and longitudinally can be quite arduous.

And then there are the practical considerations. As these are Matlab-based algorithms that employ built-in functions, pre-processing is needed to make the data compatible with these functions to enable Matlab to execute the fitting correctly. One such Matlab restriction is that the function to fit to (i.e., the rms OCT signal) only have two arguments- a vector of unknowns and a vector of X points*. Additionally, the fitting function needs Y data and an initial value guess vector to begin the iteration process. In other words, the codes need to be designed in such a way that utilizes vector inputs and outputs.

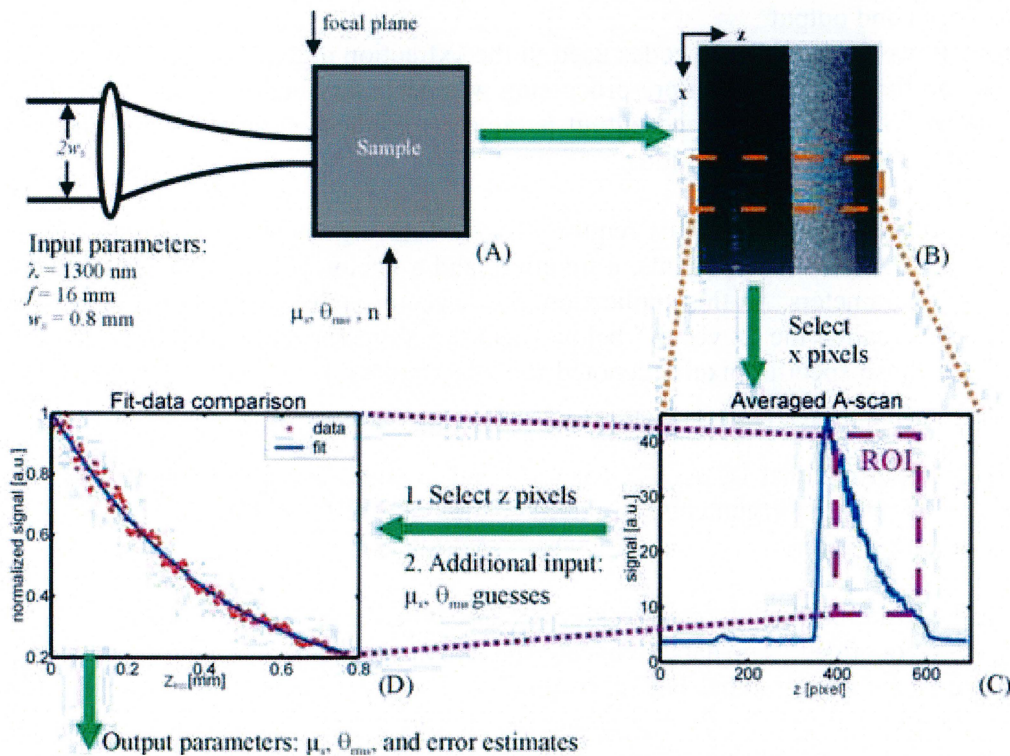


Figure 7: A schematic representation of the principles of the extraction algorithm. The sample arm geometry and input parameter values from our OCT setup are shown in (A). These parameters were used to generate an image (B) and were also employed during curve fitting (C-D). A transverse ROI was selected in (B, inset), averaged, smoothed, and plotted in (C). The axial pixels of the ROI were chosen in (C, inset), and shown as points in (D). z_{ROI} represents the probing depth within the region of interest in (D). The fit was performed on the resulting data-points using μ_s and θ_{rms} initial value guesses as additional input. The algorithm returned μ_s , θ_{rms} , the fit's error estimates, and a plot comparing the fit to the data points (D). From [35].

* Note that the usage of X and Y data points is only figuratively, and that X should not be confused with the lateral imaging direction, denoted x.

So, to build a computer-model that extracts optical properties from OCT images, the above points need to be combined with Equations (3-6). What this results in is a general algorithm whose principles are illustrated in Figure 7 [35]. Figure 7(A) shows a detailed geometry of the sample arm unit during measurements, and Figure 7(B) presents a typical raw OCT image of a tissue phantom. First, the user selects a transverse region of interest (ROI, orange dashed inset in Figure 7(B)) from a given image, consisting of several adjacent depth-scans. Averaging and smoothing is performed, yielding a curve with a high SNR that is given in Figure 7(C). The number of longitudinal pixels to which the model would be fit to was chosen from this curve (magenta dashed inset in Figure 7(C)). At this point, the iteration process begins using initial value guesses for the optical properties (μ_s and θ_{rms}) as additional input. A least squares fit of the data to the theoretical model is then computed. Finally, Figure 7(D) shows a comparison of data points fit to $\sqrt{\langle i^2(z) \rangle}$, returned along with the scattering coefficient μ_s , the root-mean-square scattering angle, θ_{rms} ($g_{eff} = \cos \theta_{rms}$), and error estimates. Of note, the same general algorithm can be used to extract μ_a also, except Equations (3) and (5) are replaced with Equations (7-11).

3.4.2 Input and output

Above it was stated that the codes used in the extraction algorithm consisted of built-in Matlab functions, and that pre-processing was necessary before initiating the fitting iterations. Thus the input and output parameters of these codes likewise had to be tailored to these built-in functions.

Matlab curve-fitting algorithms require at least four arguments: A vector of X data points, a vector of Y data points, a function, and a vector of initial value guesses for the fitted parameters. In this application, the X vector is the vector of depth positions or z pixels (called the “z vector” below), and the Y vector is the pre-processed OCT signal at those specific pixels (denoted the “data points”). The function fit to is the rms OCT signal $\sqrt{\langle i^2(z) \rangle}$ described in Section 3.2, and the fitting parameters are the optical properties, that is, μ_s , θ_{rms} (or g_{eff}), and in some cases μ_a . Because of these restrictions on input arguments, an intermediate output file is needed for the codes to ‘talk’ to one another.

As curve fitting in Matlab requires nice vectors, other input parameters are needed for them to be obtained. The data points are found by averaging laterally over an ROI, so the lateral and longitudinal boundary pixels (x_1 , x_2 , z_1 , and z_2 , respectively) are of course a prerequisite. Furthermore, there is another physical restriction complicating the z vector: Light returning from the air-tissue interface has undergone a specular reflection, and the lateral coherence length from a specular reflection is different than that for diffuse reflection [22,32]*. Excluding the part of the OCT signal that correspond to the specular reflection is done by adding an offset parameter z_{peak} , so that the ROI starts a few microns ($= z_1 - z_{peak}$) into the tissue. Altogether, there are eight input parameters: the OCT data file, the intermediate file, x_1 , x_2 , z_1 , z_2 , z_{peak} , and the initial value guess vector.

* The difference in lateral coherence length between specularly reflected light and diffusely reflected light arises because the shower curtain effect is not present in the case of a specular reflection, as opposed to the diffuse reflection which occurs inside the tissue [22,32].

In contrast to the input parameters that are restricted mathematically and physically, the output parameters of the algorithm have no such constraints. Basically, what is needed are the iterated optical properties (μ_s , θ_{rms} , and possibly μ_a), a “goodness of fit” parameter, and a graphical comparison of the fit to the data points. All of these can be easily implemented in the algorithm, as shown in Figure 7. To measure the “goodness of fit” parameter, the average deviation (or error) of the fit from the data was calculated, as well as the maximum deviation. The former is considered more seriously, as the latter is susceptible to outliers. Of note, it is possible that the iteration procedure does not converge to a single solution, or converges to a solution that is physically meaningless (i.e., $\theta_{rms} = 2$); thus the user needs to screen the results and make the final interpretation on whether or not the solution is reasonable.

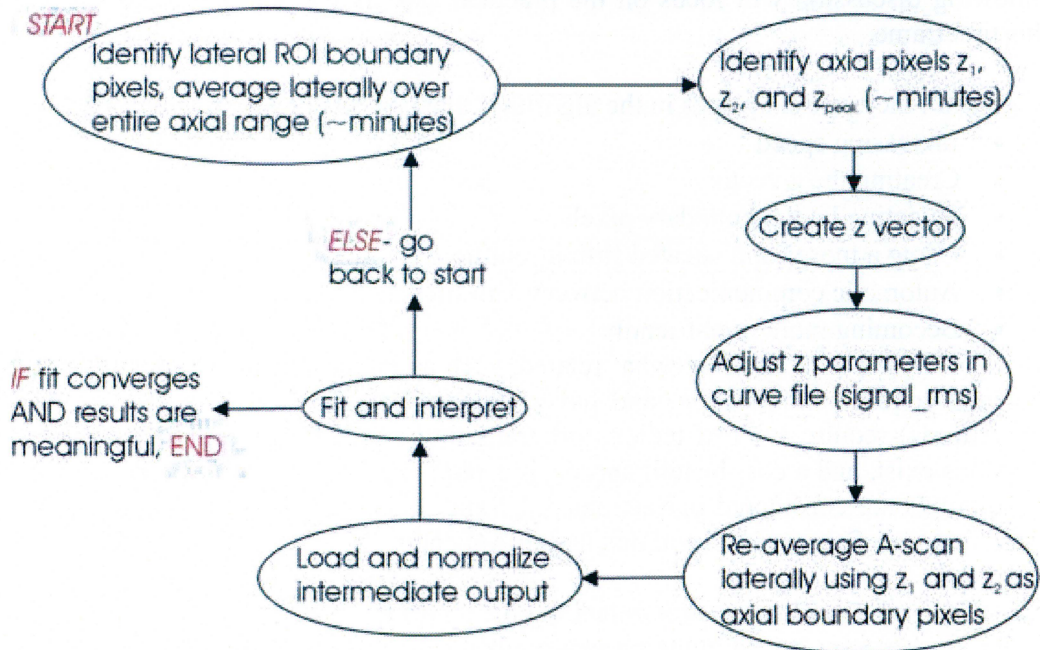


Figure 8: A schematic detailed overview of the old extraction algorithm. Note every step requires manual user input, particularly the first two that can take several minutes. Also central to the algorithm is the IF-ELSE clause, which governs whether or not the procedure needs to be repeated.

3.4.3 The first algorithm: What can be improved?

This section explains the initial extraction algorithm (written by Michael H. Frosz). We used this algorithm in our initial extractions, experimentally validating the technique of extracting optical properties from OCT images [35] and applying it on tissue [35,38]. With one of the principal objectives of this thesis being semi-automation of the extraction algorithm, this was the starting point. Below the description is a discussion of what needs to be improved, and what can be improved within the scope of this thesis.

A detailed schematic of the old algorithm is given in Figure 8. The user begins by selecting the lateral ROI boundaries, which are used to compute an averaged A-scan of all 690 pixels. Next, the user needs to manually select the three axial pixels, z_1 , z_2 , and z_{peak} . Typically, these first two steps take several minutes. A z vector representing the physical length of the ROI inside the tissue is then manually created, and the essential z pixels are inserted into the file representing the rms OCT signal

(`signal_rms.m`). Once again the user needs to perform averaging, this time using z_1 and z_2 to longitudinally truncate the A-scan. The intermediate output is loaded and the fitting algorithm executes. Finally, as stated above, the user must assess the physical validity of the results (assuming they converged to a solution), and decide if tweaking one of the transverse or axial input parameters is necessary.

Since every step in this algorithm is manual, the ideal extraction algorithm would be completely automated and ‘smart’, i.e., the computer would assess the results and characterize the tissue based on *a priori* knowledge. But writing such an algorithm would require years of investigation in a plethora of research fields, hence the following discussion will focus on the practical aspects that can be improved given this timeframe.

In general, there are six places in the algorithm that can be improved, which are:

- Increasing speed
- Creating the z vector
- Selecting lateral boundary pixels
- Using a more sophisticated fitting routine
- Automatic communication between *.m files
- Becoming more user-friendly

Some of these points are somewhat related, such as increasing speed and automating the inter-code communication, and have engineering solutions. Others, (i.e., user-friendliness) require a lot of tedious programming. Still for other cases, no simple solutions exist, and a cost-benefit approach is required to maximize efficiency. All of these points are considered in Sections 3.4.4 and 3.4.5, and the solution arrived at is summarized in Section 3.4.6 and detailed in Appendix B.

3.3.4 Physical considerations for extending the algorithm

Of the six concerns raised in the previous subsection, the most perplexing problem is, given the complex geometry of tissue, how can an ROI be correctly and efficiently delineated? Consider a case where the outer surface of the tissue forms an oblique angle with respect to the transverse and longitudinal directions. In the subsequent averaged A-scan, each point will have contributions from different optical depths (depending on the angle of course) and the resulting fit will be prone to errors. Likewise, the specular reflection point will be blurred out, so locating the correct delimiting pixels is not at all trivial.

Another problem arises when the ROI is histologically heterogeneous in either the longitudinal or lateral directions. The question of how to handle stratified tissue where the two layers have similar optical properties (i.e., collagenous and elastic tissue in arteries) is a complicated mission all on its own. For such tasks, many sophisticated morphological and segmentation algorithms could be implemented, i.e. from Reference [39]. This problem becomes even more laborious when the tissue composition changes in the less sampled lateral direction. Clearly, a cost-benefit analysis is crucial for coding a practical and scientifically valid algorithm that accounts for such common tissue heterogeneity.

The problems depicted above are solved by assuming and approximating, and there is a trade-off between accuracy and speed. One should realize that at this stage,

efficiently using the entire image for fitting is NOT feasible. Aside from tissue heterogeneity and complex geometry, there are cases where the fit just cannot converge to a single solution (this is frequently the case with fibrocalcific arterial plaques). In other words, smart segmentation algorithms do not necessarily guarantee a good fit, and some of the fit results must inevitably be disregarded. As a consequence of user assessment of the results still being imperative and inevitable, increasing speed was given the highest priority in the present algorithm.

Next, it is assumed that the angle made between the tissue and the lateral direction is small enough; or, that at a specified axial position, the optical depth in an A-scan at one ROI boundary is similar to that from an A-scan on the other side. There are many times that this assumption does not hold true, but personal experience in extractions [35,38] has indicated that there is strong overlap between large oblique angles and non-converging solutions. Similarly, the tissue within the ROI is also assumed to be histologically homogeneous, and again there is overlap between heterogeneous ROIs and non-converging fits.

Aside from identifying ROIs correctly, there is also the issue of implementing the extended model and fitting for μ_s , θ_{rms} , and μ_a . Trying to fit μ_a is tricky because on the one hand, too small of a μ_a value have absolutely no effect on the signal and thus be susceptible to computational errors; on the other, if the albedo is too low, some of the approximations made no longer hold true. Still, one point to this investigation is to search for an albedo range in which extracting μ_a has diagnostic utility.

More often than not, μ_a is rather small ($< 1 \text{ mm}^{-1}$) and thus prone to errors. Particularly, because the effects of μ_a and g_{eff}^* on the rms OCT signal offset one another, curves where μ_a effects are negligible frequently yield inconceivably large fitted μ_a or θ_{rms} values. To Matlab these variables have no assigned physical meaning. One way to overcome this dilemma is to implement both a 2-parameter (i.e., μ_s and g_{eff}) fit and a 3-parameter (i.e., μ_s , g_{eff} , and μ_a) fit on the same ROI and compare the results. If μ_a is so small that the computation yields unrealistic results, μ_s and θ_{rms} results in the 2-parameter and 3-parameter fits would be entirely different. However, if μ_a has some effect on the OCT curve, the fitted μ_s in both fits would be similar and the θ_{rms} would be somewhat lower in the 3-parameter fit. This is an important point; it implies that an analogous 2-parameter fit could be used to check if absorption influenced the OCT signal.

To improve fitting speed, the above approach was opted for. Both a 3- and a 2-parameter fit would be carried out on each ROI, with both results displayed on the same graph which contains the data points. The user would then compare the μ_s and θ_{rms} from the two fits, and if μ_s was similar and θ_{rms} slightly lower in the 3-parameter fit, the user could deduce that absorption influenced the OCT signal. Conversely should μ_s and θ_{rms} differ greatly between the two fits or the returned μ_a be implausibly high, the 3-parameter fit will be rejected.

* Of note, errors in estimating μ_a affect μ_s as well, however the effect is more pronounced in θ_{rms} . This results from θ_{rms} being determined only from pixels in the multiple-scattering regime, while μ_s is determined in both the single-scattering and multiple-scattering regimes and thus less prone to errors.

Summarizing the points of this section is as follows: To maximize efficiency, a "fit to everything and then disqualify" approach was taken. ROIs spanning the entire image would be delineated; the averaged A-scan would be fit to both models, with the user assessing the validity of both results. Should the results from the 3-parameter fit be physically meaningless, they would be disallowed. If neither model converges to a solution, if the fit does not match the data-points well, or if the ROI is heterogeneous, both results from this ROI would be excluded. As described below, lateral boundary pixels would be automatically determined, but each ROI's axial boundary pixels would require some fast graphical user input.

3.4.5 Mathematical considerations for extending the algorithm

Curve fitting can be a rather complicated task, particularly when the function to fit to is highly complex and nonlinear. The general equation is described as $Y = f(\beta, X)$, where β is a vector of the fitting parameters, f is a function, and X and Y are the independent and dependent variable vectors, respectively. Typically a least squares approach is taken, that is, minimizing the expression [40]

$$\min_j \sum_{j=1}^M \left[\frac{f(\beta, X_j) - Y_j}{SD} \right]^2, \quad (11)$$

for M data points, where SD is the standard deviation and often approximated to one. Most algorithms function by starting at a point in input parameter space (β_0) typically entered by the user and iterating new values of β until the value of the summation in the expression in Equation (11) is below a certain threshold. Iteration steps involve calculating gradients (i.e., steepest descent in parameter space) or the diagonal of the second derivative or Hessian matrix (i.e., jumping to a local minimum) [40,41]. Which type of iteration step the algorithm takes depends on one dimensionless variable as in the Levenberg-Marquardt method, or several dimensionless variables, as in robust or large-scale methods [40,41].

In the initial algorithm, the nonlinear function `nlinfit` (statistics toolbox) was used to fit the OCT signal to the theoretical model [22,38]. `nlinfit` is based on the Gauss-Newton method, whereby the second derivative matrix is only estimated. While this approximation to the Levenberg-Marquardt method is suitable in cases where only μ_s and θ_{rms} are fit, adding the error prone μ_a as a fitting parameter has a propensity for complicating the fitting procedure, resulting in non-convergent or erroneous results.

In the optimization toolbox in Matlab, one finds more robust fitting algorithms that could be rather easily implemented to improve extractions*. What is appealing about these functions is that in addition to the four standard input parameters (X and Y data, function, and guess), many other fitting parameters and returned results could be optimized to match specific applications. These include setting bound constraints on fitting variables, altering the fitting method or the maximum number of iterations, outputting diagnostics describing the fit, and many other options.

* There is also the curve fitting toolbox that is available in more recent versions, but not with Matlab 6.1, the version used in this thesis.

When analyzing the challenge of optical properties extractions, a couple of observations are evident. First, this is an over-determined problem, i.e., the number of data points is bigger than the number of fitting parameters. Second, the scattering and absorption coefficients have a lower bound of 0^* , and θ_{rms} is bound between $\pm(\pi/2)$. To solve such a problem, Matlab recommends [41] using the large-scale algorithm, whereby the problem is approximated to a two-dimensional trust region subproblem[†]. Aside from these optimizations, the maximum number of iterations and function evaluations has also been increased to 500.

3.4.6 Making the algorithm more user friendly

This section is primarily concerned with building a semi-automated algorithm that is fast and efficient, robust enough to handle the current model yet easily expandable to keep up with future modeling improvements. A special focus will be paid to optimization routines and user-friendliness.

But first, there is one self-imposed restriction: Only one command should be typed. Of course additional input will be needed from the user, but it should be obtained interactively, and preferably through mouse clicks. Ideally, this could be done with a graphical user interface, which could appropriately process and relay information between the respective *.m files, as well as display the results in an efficient manner. Designing a functioning robust graphical user interface that could meet all the objectives of the code would take months, and hence would not be possible within this thesis. Instead, simple built-in interactive dialog boxes from Matlab 6.1 were used to guide the user through the extraction program.

In conjunction with the predefined dialog boxes, there are additional Matlab functions and figure properties that could be used for amending the extraction algorithm. For example, enlarging the figures could further enhance visualization. Furthermore, the function `ginput` allows the user to click on a figure several times, and returns the X- and Y- coordinates of the last position where the mouse was clicked [41]. Combining this function with the zoom options available for normal Matlab figures can therefore be used to greatly accelerate obtaining z inputs. It is this mixture of graphical input and zoom options that is at the core of the new algorithm.

* In theory, neither μ_s nor μ_a have upper bounds, but because of approximations made during the modeling, μ_a has an upper bound of one. However, with this upper boundary limit imposed returned μ_a values frequently matched this limit more often than without it, indicating a physically meaningless solution was obtained. This may be a consequence of the altered trust region (see below).

† The trust region is ellipsoidal in shape and the two variables are redefined preconditioned conjugate gradients of the fitting variables. Consequently, the resulting minimization equation becomes

$$\min \left\{ \frac{1}{2} s^T H s + s^T \nabla \right\} \text{ such that } \|Ds \leq \Delta\|.$$

Here s is the iteration step, H is the Hessian matrix, ∇ is the gradient matrix, D is a diagonal scaling matrix, and Δ is a positive scalar. The superscript T denotes transposition, and $\|\cdot\|$ is the two-dimensional norm. This method utilizes principles similar to those of the Levenberg-Marquardt algorithm described above, with the additional estimation that s is within the defined trust region. Of note, adding constraints can alter the shape of the trust region, which may in turn affect the fitting results [41].

3.4.7 The new algorithm

Amalgamating all the points from the previous sections, and taking advantage of the concept of a FOR loop, a new fast algorithm was coded that is schematically outlined in Figure 9. To initiate the algorithm, the user simply types 'extract' in the Matlab command prompt. First, the user selects a data file from an 'open-file' dialog box. Next, the image is displayed and the user is prompted for a number N (default = 13) of lateral segments or ROIs that the algorithm will generate from the image (analogous to Figure 7B). This initiates a FOR loop of N cycles. During each loop cycle, the averaged A-scan is plotted and the user has to zoom and click on the positions corresponding to z_{peak} , z_1 , and z_2 (corresponding to Figure 7C). The 3-parameter model and the 2-parameter model are both fit to the data points (as in Figure 7D), and the results returned are stored for display in intermediate output *.txt files. Initial value guesses remain constant for each curve-fitting attempt. For the case of a non-converging solution to a particular fit, a vector of zeros replaces the last iteration results returned for that fit. An output display routine reads the data, then plots both fit results, adds labels, and exports the graphs from each ROI as a *.jpg. Finally, the algorithm re-displays the original image with all the ROIs highlighted to facilitate user assessment of the results. An example of an OCT image where the ROIs are highlighted is found on the cover.

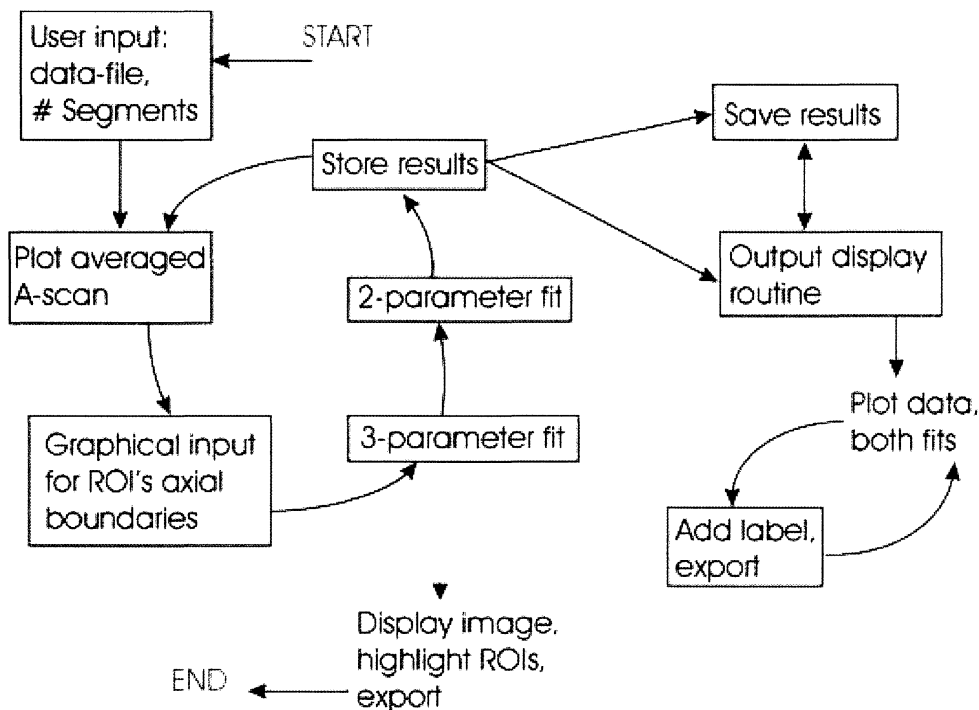


Figure 9: A schematic of the new extraction algorithm. The user begins by clicking an OCT file and entering the number of segments or ROIs that the image will be divided into. A FOR loop is initiated, where the user has to graphically click on the three key z pixels (z_{peak} , z_1 , and z_2) axially delineating the ROI on the average A-scan curve of each segment. Both 3- and 2-parameter fits are carried out on the specified ROI, and the results are stored. A secondary routine is initiated that reads the results and for each ROI segment displays both fits compared to the data points. Finally, the algorithm re-displays the image, with all the ROIs highlighted.

With this new algorithm, entire OCT images can be processed in approximately ten minutes, i.e., repeating the scheme outlined in Figure 7 N times. In the previous

algorithm, this took an entire workday. Instructions guiding the user throughout the process appear as message boxes at each step of the algorithm, making it quite self-explanatory. Table 1 below summarizes all the input parameters in both the old and new algorithm, their purpose, and outlines the improvements that came with semi-automation. A more detailed description of the new algorithm and its sub-codes is found in Appendix B.

Table 1: Automation improvements in the extraction algorithm. In the old algorithm, all the input parameters were entered manually as commands or inserted into *.m files, while in the new algorithm only dialog boxes and graphical input via mouse clicks were used. Some unnecessary input parameters were eliminated.

<i>Input parameter</i>	<i>Purpose</i>	<i>Old algorithm input</i>	<i>New algorithm input</i>
Input filename	File to process on	Manual input parameter in <code>average_a_scan.m</code>	“Open file” dialog box
x_1 x_2	Transverse ROI delimiters	Manual input parameter in <code>average_a_scan.m</code>	“User input” dialog box prompts user for N, a new variable used to calculate these values
z_1 z_2	Axial ROI delimiters	Interactively determined in figure, then re-inserted into <code>average_a_scan.m</code> , <code>signal_rms.m</code> , and defined in command prompt	One-time graphical input using mouse clicks and pressing enter
z_{peak}	Determines signal offset		
Intermediate ‘output’ filename	Transfer information between *.m files	Manual input parameter in <code>average_a_scan.m</code>	Variables remain constant for all fits, user input no longer required
Initial value guesses	Starting point for iterations	Manual input parameter in <code>fitforme.m</code>	

4. Experiments with phantoms

Once new diagnostic techniques claiming to make measurements with improved accuracy are developed, they need to verify their claim on phantoms where the properties in question are well-controlled. Typically, these ‘validation sets’ of experiments compare the new technique to a well-established existing technique by making measurements on the same phantoms. In this application, the extraction algorithms discussed above needed to be tested on phantoms with optical properties similar to those of tissue. To accomplish this feat we used solid epoxy phantoms that had titanium dioxide and dye embedded in them to mimic tissue scattering and absorption, respectively. Section 4.1 describes the production and characterization of these epoxy tissue phantoms.

In addition to creating real tissue phantoms for evaluating the new algorithm, numeric tissue phantom were also used. Numeric phantoms are created using Monte Carlo simulations of the OCT sample arm geometry [42,43] which generates a sample A-scan, on which curve fitting was performed. Section 4.2 will review the OCT Monte Carlo model and give more detail about these experiments and results.

4.1 Epoxy tissue phantoms

In order to establish the reliability of the OCT extraction algorithm, comparative experiments with integrating sphere measurements [44] evaluated with inverse adding-doubling [45] were carried out on a set of solid tissue phantoms, accompanied by a Mie calculation [1]. Because there are two extraction algorithms, experimental validation on phantoms needed to be carried out twice. Furthermore, the latter algorithm required highly absorbing phantoms that were unavailable and thus needed to be produced. The general recipe and ingredients for both phantom sets was identical, as were the characterization methods. For clarity, phantom production will be described first in Subsection 4.1.1, followed by an overview of the characterization methods in Subsection 4.1.2. Concluding this section will be the results comparing these methods to OCT extractions and the corresponding discussion, presented in Subsection 4.1.3.

4.1.1 Recipe

So exactly what are tissue phantoms and how does one make them? To mimic tissue, phantoms need to replicate their optical properties, i.e., μ_s , g , μ_a , and n . While phantoms need only be a background medium filled with scattering and absorbing agents, good phantoms require the user have a high degree of control over these properties during preparation. The ideal phantom material would be homogeneous with easily controllable optical properties, have a long lifetime, could effortlessly be formed into complex shapes [46,47], and have a reproducible design that is straightforward to prepare [48].

When searching for a stable robust solid background medium, curing plastics (i.e., polyester or epoxy resins) are frequently considered because they have stable optical and mechanical properties and adding scattering and absorbing materials during preparation is relatively easy [46-48]. Epoxy resins are slightly easier to handle when preparing large volumes of phantoms [48]. Scattering materials are typically polystyrene microspheres, TiO_2 , or Al_2O_3 particles, all of which result in anisotropic scattering common to tissue. Dyes having a flat absorption spectrum at the investigated wavelength region are used for absorption.

The phantoms used in this investigation were made of DGEBA (Diglycidyl ether of bisphenol A) hardened with an aliphatic amine; the scattering and absorption materials were TiO_2 and copy machine toner, respectively. As mentioned above, two sets of phantoms was needed, a high-albedo set for the first algorithm and a low-albedo for the second. A high-albedo phantom set was available from a previous investigation [49], but a separate set of low-albedo phantoms was needed for evaluating the new extraction algorithm. Preparing a new set of phantoms meant starting from a recipe left by Johannes Swartling, who made the previous phantom set during his PhD research with LTH. He left a recipe for making such phantoms, which was used and modified during this thesis. Clarifications were made to his recipe and a specific step-by-step instruction manual (titled ‘Epoxy phantoms for dummies’) was devised for making phantoms in polypropylene cups and 1 mm thick slabs. The addendum notes to his formula are found in Appendix C.

4.1.2 Characterization and calibration

Experimentally verifying our OCT extraction algorithm involves measurement on several phantoms with optical properties spanning a large range, obtained with a well-established method for attaining optical properties from such samples, i.e., the integrating sphere method [44] and inverse adding-doubling (IAD) [45]. Both techniques are reviewed in the following two sub-subsections. However, IAD returns the anisotropy factor g , yet the OCT extraction algorithm returns g_{eff} . To adequately compare the g_{eff} values extracted from phantom images the scattering phase function of 1300 nm light in those phantoms needs to be calculated using basic principles from Mie theory [1].

Of note, as there were two phantom sets, measurements on the high-albedo set and subsequent data processing were done in the spring of 2003 for validating the old extraction algorithm [38]. These methods and results from that phantom set are discussed throughout the remainder of this section. As a consequence of the relatively limited time allotted for a plethora of activities in this thesis work, the low-albedo phantom set has yet to be evaluated. Nevertheless the calibration procedure would be identical to Sub-subsection 4.1.2.1 and 4.1.2.2.

4.1.2.1 Integrating sphere

Using the integrating sphere setup, it is possible to measure transmission through and reflection from a thin slab by collecting the corresponding light flux within a sphere [13]. As shown in Figure 10, in transmittance measurements the sample investigated is placed at the entrance port of the sphere, while in reflectance measurements it the opposite port is used. The novelty of the setup is that it enables measurements of light globally propagating from a sample integrated over all solid angles using one detector on the inner sphere wall [13]. This is made possible by the highly reflecting inner sphere surface, and with the spherical geometry the reflected power is homogeneously distributed over the entire inner sphere surface. Accordingly the power registered by the detector is proportional to the total reflected/transmitted power, which can be calculated by relating to a reference measurement.

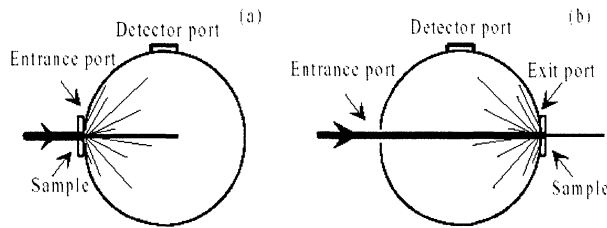


Figure 10: A Schematic sketch of an integrating sphere measuring transmittance (A) and reflectance (B) of a sample. From [50].

Our measurements of the diffuse reflectance and transmittance were performed using an integrating sphere (Labsphere model RT-060-SF) with the broadband source (AFC) operating at a center wavelength of 1300 nm also used for OCT imaging. Light was guided to the sphere using a single-mode optical fiber and collected by an IR detector supplied by the sphere manufacturer. The beam arriving at the transmission port was 2.3 mm in diameter, with a port diameter of 25.4 mm. A chopper rotating at 730 Hz modulated the beam, and was synchronized with a lock-in amplifier on the detector side to increase SNR. Both diffuse reflectance and diffuse transmittance measurements were done three times each with sample orientation randomized.

4.1.2.2 Inverse adding-doubling

The adding-doubling algorithm attempts to evaluate light distribution in turbid media by analyzing only the total reflection off and transmission through the sample [13]. This method takes known reflection and transmission profiles from a very thin homogeneous slab and determines the reflection and transmission profiles of a slab layer twice as thick by juxtaposing two identical copies of the original slab and summing up the contributions from each*. This process of doubling the layer's thickness by adding an identical slab and computing the new reflection and transmission profiles for this new layer is repeated until the desired (i.e., arbitrary) layer thickness is reached, and its reflection and transmission profiles are found [13]. Inverse adding-doubling [45] attempts to solve the reverse problem, where a slab of finite width with measured reflected, transmitted, and unscattered components has unknown optical properties. IAD works by guessing the dimensionless albedo and optical depth and iterating until forward adding-doubling yields the measured input parameters. Our integrating sphere data was processed in version 1 of the IAD code [45] using four fluxes per iteration.

4.1.3 Comparison with OCT

Each phantom was imaged twice, with five ROIs per image. In the fitting routine, the number of z pixels in an ROI was maximized and kept constant. A random number generator determined the transverse boundary pixels for each ROI. The fitted length was chosen to be 0.77 mm (186 pixels), the maximum that could be used in all the images accounting for phantoms imaged at a small angle. There were fifteen[†] curve-

* The word 'profile' is used because light is scattered in many directions and is not simply determined by the Fresnel coefficient formulae.

[†] Based on experience, the true scattering parameters of a phantom are most accurately and reliably determined by thoroughly exploring input parameter space, i.e., by performing multiple fits on the same ROI using different combination sets of μ_s and θ_{rms} guesses in each (Figure 7(C-D)).

fitting attempts in each ROI. Phantoms whose optical depth did not exceed 1.3 as determined with the integrating sphere and thus did not definitively enter the multiple-scattering regime were excluded.

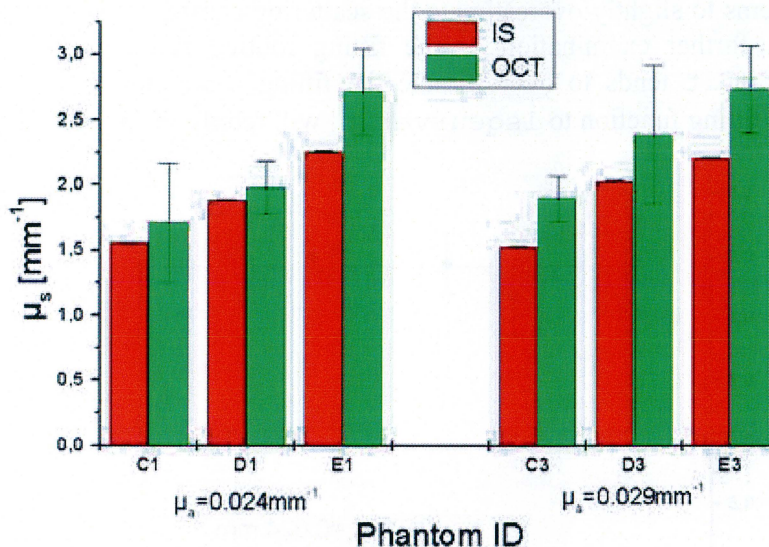


Figure 11: A comparison of μ_s values (means \pm standard deviation) obtained from measurements on tissue phantoms with OCT extractions (green) and the integrating sphere (IS, in red). Note a step-wise increase on two separate sets of 3 phantoms purposely prepared to exhibit such an increase. Details about phantom nomenclature can be found in Reference [49]. From [35].

A graphical comparison of μ_s obtained from OCT extractions and from the IAD code is shown in Figure 11. Error bars representing the standard deviation on the measurements are not readily visible on the sphere data since the standard deviation did not exceed 0.25% of the mean. A Mie calculation using the code from Reference [1] for homogeneously shaped spherical particles was performed to obtain a theoretical $g_{\text{eff}} = 0.885$. The Gaussian fit to the scattering phase function with θ_{rms} identified was shown earlier in Figure 4. A comparison of g_{eff} derived from OCT extractions to the theoretical result is shown in Figure 12.

As shown in Figure 11 and Figure 12, the extraction algorithm generated consistent and reliable results for the tissue phantoms investigated. Every value of g_{eff} extracted overlapped with the 0.885 obtained from the Mie calculation within the error bars (Figure 12). Moreover, a step-wise increase in μ_s was clearly observed with two different phantom sets (3 phantoms/set) using *both* techniques (Figure 11). While the error bars in three of six phantoms overlapped with the value returned from the IAD algorithm, the difference in the remaining three did not exceed 13% of the IAD returned value.

In examining the potential sources of error in the OCT extractions, the following should be considered: The integrating sphere measures optical properties of scattering media on a macroscopic scale as an average throughout the sample, while optical property extractions from an OCT image involves averaging over a much smaller region. Thus, inevitable phantom inhomogeneities on a μm scale could have affected our results. Also, IAD does not take wavelength as one of its inputs [45], or in other words, is designed for monochromatic light where samples exhibit uniform optical properties. The source used in this experiment had a 3 dB bandwidth of 60 nm, which

could have an influence on the experiments and thus the returned IAD data. Furthermore, phantom albedos (~ 0.97) were slightly outside the recommended range of 0.4-0.95 for achieving the highest accuracy with the IAD algorithm [51], and this too could have slightly offset the IAD data points. One can notice also that the OCT-technique seems to slightly overestimate the scattering coefficient for these particular samples. A further examination of the fitting routine revealed that the Matlab function `nlinfit` tends to overestimate the fitting parameters. We believe that changing the fitting function to `lsqcurvefit` will rectify this problem*.

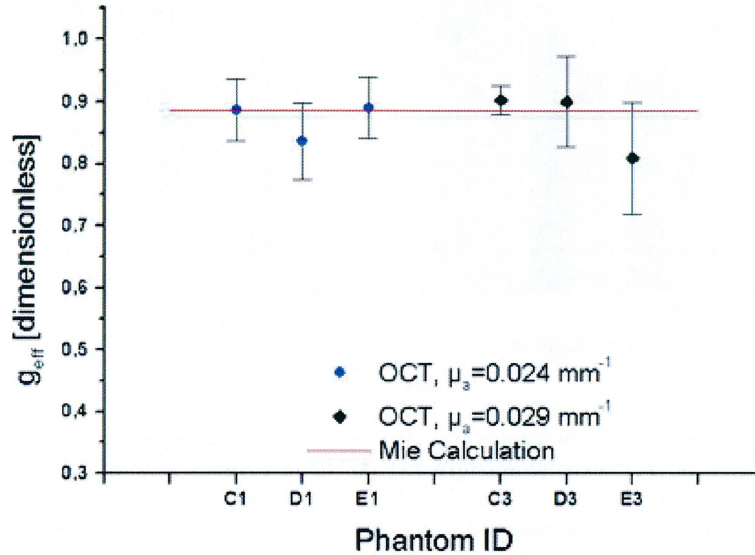


Figure 12: A comparison of g_{eff} value (means \pm standard deviations) from OCT extractions (points) and the Mie calculation (line). Overlap in results is seen for every phantom. Details regarding phantom nomenclature can be found in Reference [49]. From [35].

Considering the fine overall agreement between extracted values using our algorithm and the IAD algorithm, we concluded that our algorithm was capable of extracting optical properties with sufficient reliability.

4.2 Numeric phantoms using the Monte Carlo method

As demand for phantoms increased and the desired complexity level became impractical, numerical experiments have gained wide acceptance as a suitable alternative. Biomedical optics in particular makes use of computer-based Monte Carlo (MC) models [52,53], serving as a numerical phantom simulating light propagation in tissue. This section explains numerical experiments with a Monte Carlo based OCT model [42,43] as a means for validating the ability to extract μ_a using the new extraction algorithm. Subsection 4.2.1 reviews the MC method, detailing some of the advantages and disadvantages and Subsection 4.2.2 describes the basics of the OCT-based model. An overview of the simulations run and the

* As explained in Section 3.4, `nlinfit` uses the Gauss-Newton method for fitting the data, while `lsqcurvefit` uses the trust region method. One of the observed peculiar errors resulting from estimating the diagonal of the Hessian matrix, as `nlinfit` does, are that the fitted parameters tend to be overestimated. As overestimation is not as prominent in `lsqcurvefit`, it is believed that switching routines would result in improved parameter estimation.

corresponding results is given in Subsection 4.3.3, and finally, the section concludes with a discussion in Subsection 4.2.4.

4.2.1 Why Monte Carlo?

The name ‘Monte Carlo’ refers to a general technique for applying a stochastic approach in a situation where several outcomes are possible, i.e., using a random (or pseudorandom) number generator to determine a particular outcome of one or more variables [54]. In biomedical optics, Monte Carlo refers to solving the radiative transfer equation [13] by tracing an tremendously large amount of small energy packets called photons^{*}, each carrying a proportional amount of the total light energy [52]. Summing up all the contributions from all these small energy packets result in a desired average. The user simply specifies the geometry and optical properties (μ_s , g , μ_a , and n_R) as well as the number of photons, and the computer code determines their propagation path in the medium and the overall flux [53]. Using a Monte Carlo model has several advantages, chiefly, that these experiment are ‘clean’ and thus not prone to errors during preparation, calibration, and measurements as real phantoms are. Moreover, the optical properties and the geometry are very easily controlled [53].

One of the primary motivations for developing an OCT model based on Monte Carlo was to serve as an alternative model to the analytical model based on the extended Huygens-Fresnel principle. Because light propagation is modeled differently in the MC and EHF models, one may be used as a check to the results of the other and vice versa. Of note, and some discrepancies do exist. Recently, the MC model has been used by Thrane *et al.* [55] to confirm a 2-layer analytical model and corresponding extraction algorithm[†]. Physically constructing a 2-layer phantom would be rather cumbersome, thus illustrating the utility of this numerical method.

4.2.2 Essentials of GMCML

A Monte Carlo method for modeling heterodyne detection in OCT has been developed by Tycho *et al.* [42,43]. This code, abbreviated GMCML (Gaussian Monte Carlo Multi-layer), is an extension of the original MCML code by Wang *et al.* [52,53] applied to the OCT sample arm geometry. The theoretical basis for this model comes from the modeling the diffusely reflecting tissue discontinuity as part of a 4F optical system (see Figure 13). Propagating the mutual coherence function Γ_S (see Equation (14) in Appendix A) from the discontinuity (q) plane to the left lens (p) plane results in a delta-correlated sample field U_S . Because the p and q planes are 1:1 conjugates, it follows that the heterodyne efficiency factor at the p plane (Ψ_p) can be computed from intensity distributions at the q plane only [42,43]. In other words $\Psi_p = \Psi_q$, which is not an inherently trivial result: This means that the MC simulation does not have to account for the finite spatial coherence of the light [42,43] to obtain a relevant heterodyne efficiency factor! Specifically, the efficiency factor can be defined as [42]

^{*} Note these are not photons in the quantum mechanical sense, but simply small bundles of energy propagating in a manner similar to light. The word photons will be used to describe these packets in the following discussions.

[†] Although the 2-layer model was not part of this thesis and thus not discussed in the report, it is very relevant to the work described here and represents a big step forward in terms of demonstrating the reliability of using OCT to extract optical properties.

$$\Psi_{MC} = \frac{\langle i^2 \rangle}{\langle i^2 \rangle_0} = \frac{\int I_R(\mathbf{p}) \langle I_S(\mathbf{p}) \rangle d^2\mathbf{p}}{\int I_R(\mathbf{p}) \langle I_S(\mathbf{p}) \rangle_0 d^2\mathbf{p}}. \quad (12)$$

As previously, the efficiency factor is defined as the intensity ratio of the sample beam in the presence of scattering to the case with no scattering*. However, contrary to normal OCT systems where the root mean square heterodyne signal current $\sqrt{\langle i^2 \rangle}$ is detected, GMCML records the mean square current $\langle i^2 \rangle$ [42,43], and this difference was implemented in the appropriate fitting algorithm. Of note, one MC simulation means one value for the heterodyne efficiency factor at a particular depth. To generate a nice curve for fitting, several runs are needed.

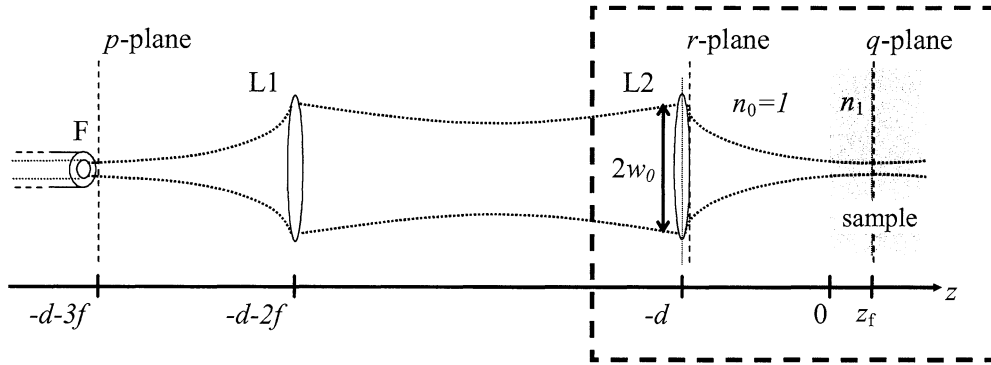


Figure 13: MC setup figure to get from Andreas. Here the q plane is demarks the discontinuity, and r plane is right lens plane. Of note, lenses are infinite in the transverse direction. From [42].

To simulate the OCT signal from a discontinuity, the GMCML code works in the following manner [42,43]: A photon is launched from the right lens (r) plane towards the tissue (see Figure 13) in the shape of a Gaussian beam. Tracing through the turbid media until the discontinuity is done via the MCML code[†] [52,53]. At the discontinuity, both the azimuthal angle ψ and deflected angle θ are (indirectly) stochastically determined and stored along with its position. These values are used to determine the photon's direction of propagation back through the 4F system. Like forward propagation, photons would backpropagate through the turbid medium using the MCML code until reaching a position in the p lens plane. Finally, the weights of photons hitting the p plane within the extent of the reference beam are summed to obtain the intensity ratio in the presence of scattering [42,43]. A similar run is needed to find the signal in the absence of the scattering medium. A more detailed explanation of the code and its comparison to the EHF model is found in References [42,43].

4.2.3 Methods and results

Overall, there were three curves generated with ten data points in each curve, spanning a probing depth of 1 mm in intervals of 100 μm . The three curves were identical in all aspects except the absorption coefficient μ_a , which was set to 0.5, 0.25,

* Absorption effects, although not included in the model [42], are included in the GMCML code, and the derivation presented should still hold true should absorption be present.

[†] However, a Gaussian scattering phase function is used here, whereas the Henyey-Greenstein phase function is used in the original MCML [52,53].

and 0.12 mm^{-1} , respectively. As for the rest of the parameters, they were set to emulate the OCT system used for imaging, that is: $w_0 = 0.8 \text{ mm}$, $f = 16 \text{ mm}$, $\Delta\lambda = 60 \text{ nm}$, $\lambda_c = 1.31 \text{ }\mu\text{m}$, $\mu_s = 5 \text{ mm}^{-1}$, and $g_{\text{eff}} = 0.97$, and $\text{Re}[n] = 1^*$. An additional MC simulation was made for normalization purposes, with the turbid medium omitted. An example of an input *.mci file is found in Appendix D.

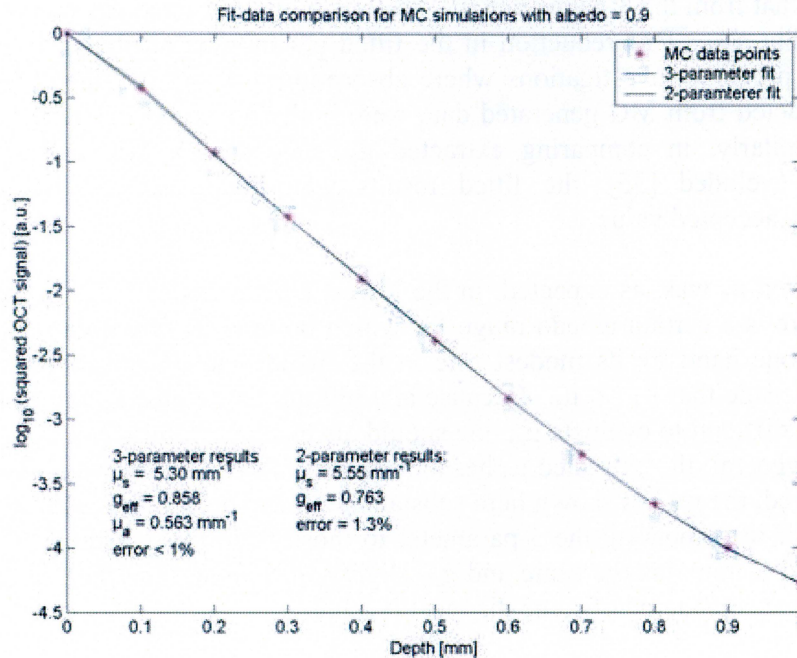


Figure 14: An example of processing the Monte Carlo results. Note the 3- and 2-parameter fits are indistinguishable by eye. For numerical results, see Table 2.

All the data was read and processed in Matlab, in a manner similar to that described above. Both a 3-parameter fit and a 2-parameter fit were fit to each generated curve. An example of the resulting curves is given in Figure 14. The fit results are summarized in Table 2.

Table 2: Extraction results from the Monte Carlo simulations using 3- and 2-parameter fits. The only variable between the curves was μ_a . Error is defined as the deviation from the fit to the data points as determined by the MC simulation. Recall $\mu_s = 5 \text{ mm}^{-1}$ and $g_{\text{eff}} = 0.97$ were used as input.

Input μ_a [mm^{-1}]	3-parameter fit results				2-parameter fit results		
	μ_s [mm^{-1}]	g_{eff}	μ_a [mm^{-1}]	Error [%]	μ_s [mm^{-1}]	g_{eff}	Error [%]
0.5	5.30	0.858	0.563	< 1	5.55	0.763	1.3
0.25	5.26	0.873	0.139	< 1	5.29	0.855	< 1
0.12	5.21	0.889	0.003	< 1	5.21	0.889	< 1

4.2.4 Discussion

As can be seen in Table 2, both 3- and 2- parameter fits yielded satisfactory results when absorption was included in the simulations used to generate the curve. In five

* The reason for setting the refractive index to unity was more for computational than physical purposes. When modeling turbid media that closely resembles real tissue, i.e., $\text{Re}[n] = 1.4$, many photons are lost in the specular reflection of the air-tissue interface. Moreover, such a background refractive index would introduce aberrations into the beam, which are not covered neither by the MC [42] nor EHF [22] models.

of six cases, μ_s was 6% off the MC input value, and was 11% off in the remaining case. As expected, absorption effects primarily altered the OCT signal in the multiple-scattering regime. This is because absorption primarily affects photons that have traversed long distances, i.e., off-axis multiple-scattered photons [19]. In other words, at large optical depths μ_a and g_{eff} offset one another, which is what is shown here- when absorption effects were present, the g_{eff} from the 2-parameter fit was lower than that from the 3-parameter fit. Moreover, the extracted g_{eff} was much lower than the input g_{eff} . This reduction in the fitted g_{eff} may be attributed to absorption because in previous investigations where absorption was not included [55], the g_{eff} values extracted from MC generated data were both above and below the input MC value. Similarly, in comparing extracted g_{eff} values to a Mie calculation with absorption excluded [35], the fitted results were again above and below the theoretically accepted value.

The best-fitted μ_a was, as expected, in the lowest albedo case. These results indicate that there is a certain albedo range for which optimal μ_a fitting can be achieved, limited on one hand by its modest role in the model and on the other by the key assumption made that $\mu_a \ll \mu_s$. Because at 1300 nm tissue albedo values tend to be so high it is difficult to evaluate μ_a , one should always be careful when assessing such results. In general, the extracted μ_a has a meaning if there is a known absorber in the tissue. Indeed, the results shown here substantiate the approach suggested throughout this thesis- if in comparing the 3-parameter to those from the 2-parameter fit results the extracted μ_s remains the same and g_{eff} slightly increases, then the 3-parameter fit results may be considered of some diagnostic value.

Some additional factors should be considered in analyzing these results. First, because coherence effects in light propagation are not included in the MC model, there is a slight bias between the MC and EHF models that increases as the transport reduced optical depth increases [42,43]. However in References [42,43] the transport reduced optical depth, defined as $\tau_{\text{tr}} = \mu_s z \times (1 - g_{\text{eff}})$, did not include absorption effects. Here, the quantity $\mu_s \times (1 - g_{\text{eff}}) = 0.15 \leq \mu_a$. It is only logical to assume that absorption effects would increase the bias between the two models; nonetheless, the exact influence of absorption has not been properly investigated and so no further speculation on this matter is given here. It is also worth noting that MC simulations are only a model, and that some of the aspects discussed here would not be present under typical experimental conditions. Hence, the ability of the absorption inclusive EHF model to describe the OCT signal in a low-albedo medium must be verified experimentally.

Overall, the results presented here indicate that for a certain albedo range (near 0.9), absorption not only affects the OCT signal but also diminishes the accuracy of μ_s and g_{eff} extracted using a 2-parameter fit. Moreover, such errors may be reduced, though not completely eliminated, by making μ_a an additional fitting parameter. It is in cases like these where also fitting μ_a increases the diagnostic utility of the extracted scattering parameters.

5. Clinical studies using the extraction algorithm

It is important now to recall what the motivation for this study was: To facilitate qualitative high-resolution visualization of tissue with quantitative tissue optical property information. The point of this thesis is to move one step closer to *in situ* quantitative tissue characterization using OCT, which would facilitate its acceptance as a practical imaging modality capable of diagnosing tissue pathology. Improving and optimizing the extraction algorithm is the means by which we hope to accomplish this feat.

As mentioned above, vascular imaging was the relevant application for this thesis and will be focused on in the present chapter. This chapter is organized as follows: First, an introduction to atherosclerosis is given in Section 5.1, along an explanation of what the objectives of OCT are in this field. Supplementary details describing arterial anatomy and the condition of atherosclerosis are given in Appendix E. Section 5.2 is a review of the milestones intravascular OCT has had thus far in this field. Our initial experiments applying the old extraction algorithm on postmortem aortic biopsies are given in Section 5.3 along with a discussion of those preliminary results. This chapter concludes (Section 5.4) with some measurements carried out on carotid specimen removed during endarterectomy procedures, which we used to test our new algorithm.

5.1 Coronary artery disease and atherosclerosis

Coronary artery disease (CAD) is the leading cause of mortality and morbidity in the industrialized world, accounting for over 7 million deaths per year globally [56]. CAD is the result of atherosclerosis, and atherosclerotic lesions progress from early lipid-laden fatty streaks, over intermediate lesions with extracellular lipid deposits covered by a fibrous cap, to mature plaques characterized by a thick neointima and fibrocalcific vascular remodeling. CAD patients are prone to experiencing acute coronary syndromes, i.e., acute myocardial infarction (heart attack), unstable angina pectoris, or sudden cardiac death. Autopsy studies have pointed to disruption of thin cap fibroatheromas (vulnerable plaques) [57,58] as a key predecessor to acute coronary events [59]. Vulnerable plaques commonly contain a large lipid pool inside the plaque separated from the lumen by a thin fibrous cap, with intense macrophage inflammation present, and expression of proteolytic enzymes that compromise the structural integrity of the plaque [57-59].

There are two general methods for treating CAD: coronary artery bypass grafting and percutaneous coronary intervention. In the first method, a thoracic surgeon removes a healthy vessel from another part of the body and transplants it so that the blood has an alternative route to supply the heart with oxygen [60]. Making this blood vessel ‘detour’ is often a difficult and arduous task that is susceptible and sensitive to many errors. The latter option, abbreviated PCI, is where an intervening cardiologist attempts to mechanically stabilize the plaque by several catheter-based means. In general, PCI methods involve advancing a therapeutic catheter via a guidewire to the site of the culprit lesion. One common technique is balloon angioplasty, whereby a balloon is dilated inside the vessel*. Another is to use a high-powered excimer laser to dissolve the plaque. PCI requires intravascular imaging modalities (i.e., angiography, intravascular ultrasound, or intravascular OCT) to visualize the vessel

* Nowadays, the balloon often positions a cylindrical wire mesh called a stent inside the vessel and props it open in a sturdy manner.

wall to identify high-risk atherosclerotic lesions, and it is this procedure to which we hope to contribute with this study.

Ultimately, to become an integrated imaging technology assisting PCI, an imaging modality (i.e., OCT) must be able to do the following consistently and reliably [2,59]:

- Clearly identify the three major plaque types, that is, fibrous, lipid-rich, and fibrocalcific plaques, and easily distinguish them from normal vessels
- Measure a fibrous cap of 65 μm or less with sufficient resolution
- Detect macrophage infiltration in plaques
- Assess stent deployment in vessels
- Avoid saline flushing, which causes great patient discomfort*

At present, no accepted diagnostic imaging modality is capable of accomplishing any of these objectives with sufficient accuracy and reliability. This is primarily due to the low resolution and contrast in each technique. Presently, the highest resolution is obtained with high frequency intravascular ultrasound ($\sim 100 \mu\text{m}$) [2].

5.2 Intravascular OCT today

In thirteen years, OCT has achieved quite a few milestones in terms of intravascular imaging. Firstly, OCT has recently demonstrated its ability to visualize vessel histopathology at unprecedented levels of resolution and preliminary data have indicated that it is possible by OCT to qualitatively distinguish between normal arteries, and fibrous, fibrocalcific, and lipid-rich plaques [61,62]. Moreover, OCT has also been shown to quantify plaque macrophage content [63] in lipid-rich plaques, as well as assess the success of intracoronary stent implantation in patients with CAD during PCI [64]. With its micrometer axial resolution, precise measurements of fibrous caps are now possible [65]. An optically clear hemoglobin-based blood substitute has been used to displace blood and enable OCT imaging with minimal patient discomfort [66]. And finally, OCT has proven its feasibility in patients with CAD [61], and currently there are clinical tests being conducted by the group at Massachusetts General Hospital and LightLab Imaging, Inc.

And while all these accomplishments are impressive, image interpretation remains a major obstacle for OCT. Specifically, differentiating between the three types of plaques, i.e., fibrous, fibrocalcific, and lipid-rich lesions, by OCT is at present subjective and therefore interpretation of OCT images of coronary pathophysiology is difficult[†]. An objective interpretation would be important in order for a valid OCT technology to become clinically applicable and potentially adopted into future treatment guidelines for patients with CAD.

In an attempt to facilitate the interpretation of OCT images of the normal and diseased artery wall, it is important first to consider the histopathological alterations that occur in the vascular wall during plaque development. This process involves changes of the vessel wall architecture, cellular content, extracellular matrix organization and biochemical composition. Although these alterations may occur throughout the

* One major obstacle for all intravascular imaging modalities is imaging through the highly scattering blood that is between the intima and the catheter. Displacing blood with saline provides a 2-3 s temporal window for imaging; however, the temporary oxygen deprivation burns the patient.

[†] Some reasons for this include similar optical properties of collagen and elastin [61] and no existing precise definition of sharp versus poor delinearity, which is necessary to distinguish a small lipid pools from large calcifications [61].

arterial wall during lesion progression, they first and foremost affect the inner intimal layer of the vessel wall, which is adjacent to the blood stream and readily assessable for OCT interrogation during percutaneous intraarterial procedures. Specifically, a reorganization of intimal collagen fibers is likely to produce changes intima's optical properties, i.e., μ_s , μ_a , and g_{eff} . It is our intention to use OCT to determine these quantities and precisely define the optical properties of both normal vessels and the three characteristic atherosclerotic lesion types.

5.3 Feasibility study

This section describes the methods and results from our initial experiments testing for differences in the optical scattering properties of atherosclerotic lesions and normal vessels using the old algorithm [35,38]. Our initial findings indicated that scattering property data obtained by OCT extractions might provide a way to objectively characterize intravascular OCT images.

5.3.1 Sample handling and imaging

Fourteen (4 normal, 4 lipid-rich, 3 fibrous, and 3 fibrocalcific) aortic segments were obtained within four hours of autopsy and imaged with OCT in phosphate buffered saline. During OCT imaging, the handheld probe was in contact with a glass cuvette inside of which the biopsies were mounted. Regions corresponding to those imaged with OCT were marked and located on digital photos. The samples were decalcified when necessary and routinely processed for paraffin embedding. Four μm thick sections were sliced at the regions as shown by the digital photographs and stained with hematoxylin and eosin or combined elastin and Van Gieson Hansen stains. Sections were examined by light microscopy with histopathological characterization of the intima. Corresponding areas of the intima were identified in OCT images and selected for subsequent image post-processing.

5.3.2 Curve-fitting

The OCT images were laterally divided into ROIs spanning approximately 20-30 A-scans representing 200-300 μm . ROIs in this *ex vivo* study were manually and systematically selected spanning an area with uniform scattering properties. Altogether, the images were subdivided into 151 ROIs; 41 normal, 40 lipid-rich, 34 fibrous, and 36 fibrocalcific. To select the correct z-pixels on the curve in OCT scans from normal arteries, boundaries of the intima were easily identified, and the final z-pixel in the fitting region was chosen as the one immediately preceding the peak arising from the intima-internal elastic membrane interface. In images of atherosclerotic lesions, it was much more difficult to identify an end pixel, as the internal elastic membrane was destroyed by the lesion. To accommodate this, the final pixel for the fit was chosen as the first pixel within 2 dB of the noise floor. In all cases, we ascertained that the sum of the length of the fitting depth and the superficial interface region did not exceed the intimal thickness as measured by light microscopy*.

5.3.3 Results and discussion

OCT images were correlated with the corresponding histological sections using Table 1 in Reference [61] as a guide and representative samples are shown in Figure 15.

* Of note, in the fibrocalcific samples, artifacts created during the decalcification process made it impossible to measure intimal thickness, and therefore we did not limit the ROI in the axial direction in these cases.

Qualitatively, images obtained by OCT and microscopy demonstrated similar gross histopathological features that allowed for reasonable differentiation between normal vessels and lipid-rich, fibrous, and fibrocalcific plaques, respectively. The distribution of μ_s and g_{eff} for ROIs of normal arteries and the three overall atherosclerotic lesion types is shown in Figure 16. To facilitate interpretation, the extracted data were grouped into intervals based on the respective values of μ_s and g_{eff} . For μ_s , the intervals spanned 5 mm^{-1} for values from 0 to 40 mm^{-1} , and 10 mm^{-1} for values over 40 mm^{-1} . Since human soft tissue is generally very forward scattering, g_{eff} range intervals of 0.05 were chosen for g_{eff} values near 1, but the interval range was larger for the limited number of g_{eff} values below 0.8.

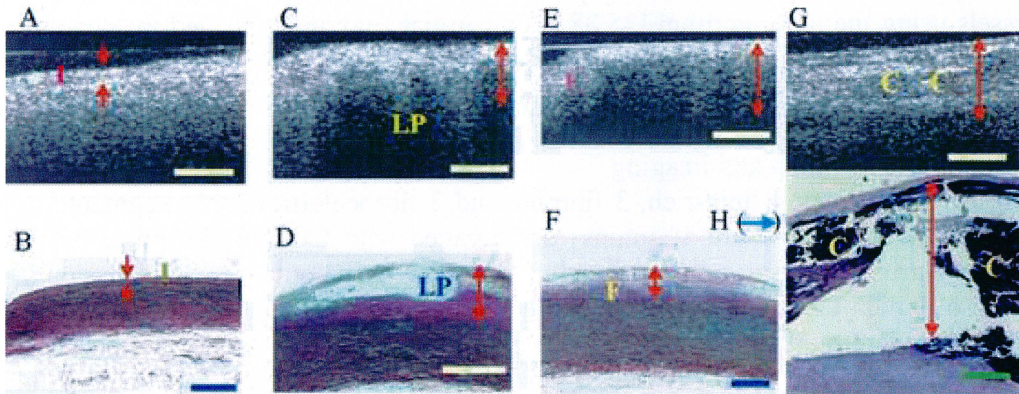
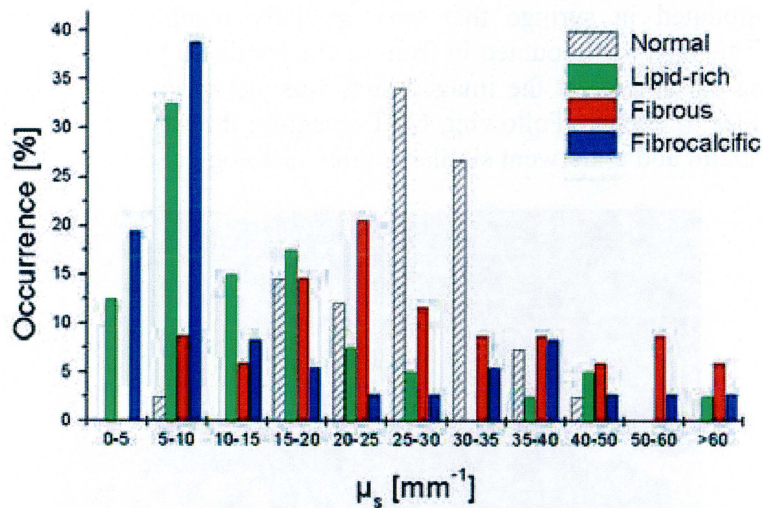


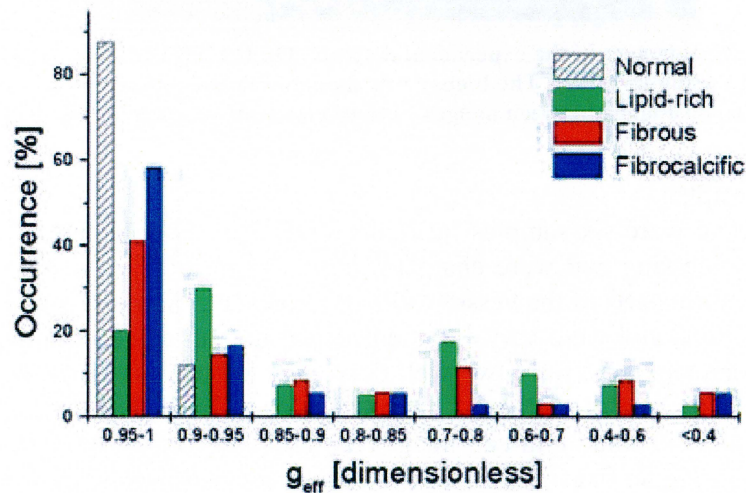
Figure 15: Correlation of raw OCT images (A, C, E, and G) and histopathology (B, D, F, and H). Normal intima labeled ‘I’ in (A-B). Lipid-rich lesion (C-D), with a lipid pool marked ‘LP’. Fibrous plaque (E-F), with fibrous area marked ‘F’. Fibrocalcific lesion (G-H), with the calcifications denoted ‘C’. Rupture artifacts caused by the decalcifying process are clearly seen in (H). The arrows represent the intima in (A-F) and the fitting region in (G-H), respectively. Bars=500 μm . From [35].

Our preliminary data suggested that very similar optical properties were observed in images of normal samples (diagonal lines) but not in those representing atherosclerotic lesions. In normal arteries, almost 90% of g_{eff} values were concentrated between 0.95 and 1, whereas more than 50% of atherosclerotic lesion ROIs were below 0.95. Approximately 95% of the normal arterial samples had μ_s between 15 and 39 mm^{-1} , while μ_s was below 15 mm^{-1} in about 60% of lipid-rich and fibrocalcific plaques. Furthermore, fibrous lesions demonstrated very considerable variations in μ_s .

To our knowledge, the above preliminary data represent the first quantitative analysis of the optical scattering properties, i.e., the scattering coefficient and the anisotropy factor, of the normal and diseased human aortic intima *in vitro* at 1300 nm. The study indicates that the presented algorithm may provide a basis for extension of the OCT technique beyond qualitative image assessment towards tissue characterization based on physical principles. Techniques for detection of unstable atherosclerotic lesions have generated enormous interest in the field of vascular biology, and the future clinical utility of such methods is dependent on minimizing subjective and operator-dependent bias in the acquisition and interpretation of data [2]. We therefore suggest that our first OCT algorithm took an important step in this direction and that further studies are warranted to define the validity of the described method for characterization of atherosclerotic lesions.



(A)



(B)

Figure 16: Distributions of μ_s (A) and g_{eff} (B) for normal arteries and lipid-rich, fibrous, and fibrocalcific atherosclerotic plaques, respectively. In (A), μ_s for normal samples (striped) were centered between 15 and 40 mm^{-1} , but were centered at lower values for lipid-rich (green) and fibrocalcific (blue) plaques, and were randomly distributed for fibrous plaques (red). In (B), g_{eff} values were generally higher in normal intimas than in atherosclerotic lesions. From [35].

5.4 Endarterectomy study

As a follow-up to the initial study on postmortem aortic biopsies, we next chose to investigate plaque removed from patients during carotid endarterectomy procedures*. Details on this procedure are found in Appendix E.1, along with illustrations of what typical samples handled look like.

Our samples were handled in the following manner: The excised plaques were placed in phosphate buffered saline and cut into 7 mm × 7 mm biopsies that were kept at 4°

* Endarterectomy procedures involved with this study were carried out by the department of Vascular Surgery at Rigshospitalet, Copenhagen, Denmark.

C until OCT imaging. Biopsies were warmed up in a warm water bath to 37° C and placed in mounted in syringe that was specially machined for optimal biopsy mounting. This unit was mounted in front of the handheld probe, as shown in Figure 17. Marking of samples at the imaged sites was again done with the digital video camera, similar to above. Following OCT imaging, the samples were fixed in 10% buffered formalin and underwent similar routine histological processing [35,38].

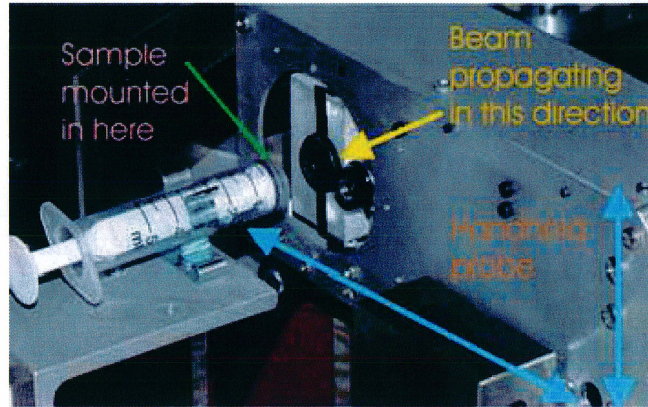


Figure 17: The sample arm in the experimental setup. On the left is the handheld probe, which remained fixed during imaging. The biopsy was mounted in the syringe on top of a translation stage, and was re-positioned between images. Transverse scans were made vertically.

5.4.1 Initial results

Altogether, there were six samples imaged by OCT at multiple sites that underwent histological processing and were characterized*. As all of the samples were partial arterectomies, only parts of the vessel walls were present. Some of the specimens had huge calcifications and were very fragmented and not suited for illustration. Of the remaining specimen, there were two well-defined atheromatous lesions in most of the intima, including some of the media. One histology image matched up well to two OCT images and the other to three†; images representative of the correlation are found in Figure 18. These five OCT images were processed using the new extraction algorithm. As in the previous study [35,38], we ascertained that the distance from the specular reflection to the deep ROI boundary (i.e., $z_2 - z_{\text{peak}}$) was not greater than the intimal thickness as measured by microscopy. For both specimens, the intima measured approximately 2 mm.

Once all the images were processed using the above algorithm, fit results that were outliers or physically meaningless had to be eliminated. To properly implement a purge process, a systematic approach was taken, and if the fitting results failed to meet certain conditions, they were excluded. In summary, these conditions were:

* Of note, actually there were two *ex vivo* studies carried out using the new extraction algorithm, one was a correlation study where the lesion was imaged at several places (similar to [35,38]), and the other was a temperature dependence of plaque optical properties, where the sample was imaged at one location with the temperature varying from 24-42° C. The latter study is beyond the scope of this thesis, and this limited the number of specimens for the first investigation to six. Moreover, excluded from the discussion here are biopsies where the histological sections were inadequate to display. This was the case in four of the remaining six samples, as decalcification left severe artifacts in the histopathological images forcing us to exclude another four samples.

† For medical studies stricter correlation rules would apply, thus for each sample, one OCT image would be matched up to one histological section.

- $\theta_{\text{rms}} > 1$
- $a < 0.8$
- $\mu_a > 3 \text{ mm}^{-1}$
- A poorly looking fit

It is worth noting that, strictly speaking, the models used [19,22] in the fit are only valid in the paraxial approximation where $\theta_{\text{rms}} < 0.5$, as well as in the condition where $\mu_s \gg \mu_a$. Outside these validity ranges, the models are considered a good first-order approximation to the OCT signal. This was the primary reasoning behind the ‘extended’ tolerances used here. Of course, as this technique develops these suggestive restrictions are likely to change.

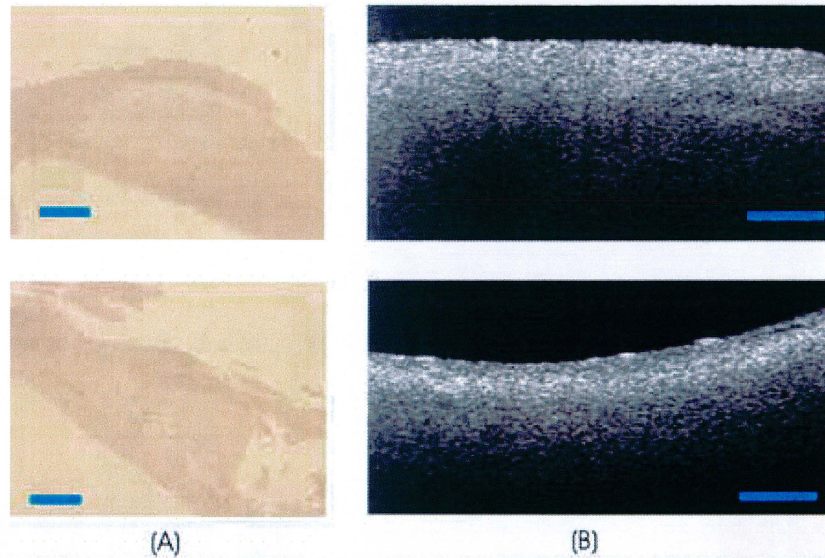


Figure 18: Representative images obtained by histopathology (A) and OCT (B) for the two lipid-rich plaques analyzed. Bar = 600 μm .

A distribution of the fitting results is given in Figure 19. Extraction data obtained from fitting only μ_s and g_{eff} is given in Figure 19(A-B), the numbers displayed generally followed the trends described in Reference [35,38]. Cases where μ_a were also fit were evaluated and then used to adjust the data displayed in Figure 19(A-B). After applying the above restrictions, the number of ROIs where μ_a results had physical meaning was only four (out of 23 total ROIs). This low number is indeed not surprising, considering that at 1300 nm tissue albedo values often approach unity [13].

5.4.2 Discussion

In reviewing these results some general observations could still be made*. First, one μ_a value was quite small ($\sim 10^{-4}$), and μ_s and g_{eff} were relatively unaffected. In the remaining three cases (13% of all the examined ROIs) there was an observable increase in g_{eff} . Noting the results from the MC simulations in the previous chapter, an increase in g_{eff} was expected when absorption was present because g_{eff} and μ_a have offsetting effects on the OCT signal [19]. In comparing the low fitted g_{eff} values obtained from the 2-parameter fit to those from the 3-parameter fit (i.e., in cases where absorption effects were present) may provide clues concerning the relatively low g_{eff} values found in lipid-rich plaques in Reference [35,38]. Analyzing more samples should provide more insight into this matter.

* Of note, in all cases where $3 \text{ mm}^{-1} < \mu_a < 5 \text{ mm}^{-1}$, the observations described here still held true.

Also, μ_s remained the same in two of the remaining cases but dramatically increased in the third. A close examination of the fit-data comparison revealed that the OCT signal in the single-scattering regime exhibited rather large modulations, and that the two fitted curves actually differed quite a bit in this region. Because it is this part of the OCT signal that primarily determines μ_s , it seems reasonable that large signal variations in this range affected the fit. This illustrates another point: By fitting two models to one set of data-points, we may more easily detect ROIs where the iterated results are not stable from the mathematical perspective.

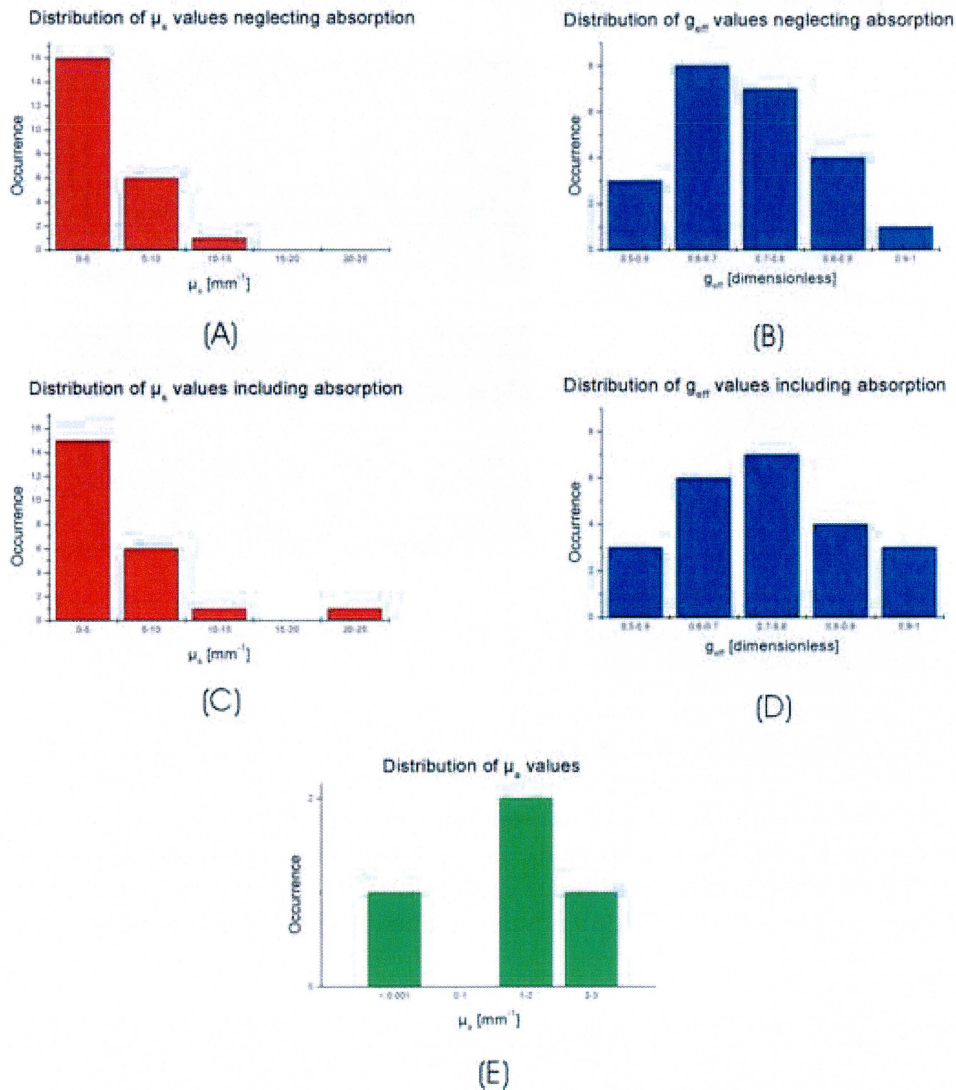


Figure 19: Distribution of μ_s , g_{eff} , and μ_a in the two analyzed atheromatous lesions. Distributions of μ_s and g_{eff} obtained by fitting to the 2-parameter model are shown in (A-B). Corrections made to these two distributions by including μ_a as a fitting parameter are given in (C-D). For completeness, the μ_a distribution is shown in (E)

What these results indicate is that in cases absorption influences the OCT signal, including μ_a as a fitting parameter may provide clearer details of the light-tissue interaction and the curve-fitting technique. Moreover, by also fitting μ_a , it is possible to correct fit results obtained using the 2-parameter model. This correction to the

distributions in Figure 19 (A-B) is found in Figure 19 (C-D). For completeness, the μ_a distributions are shown in Figure 19(E). Needless to say, to verify these assertions more detailed studies on phantoms and tissue specimens under both *ex vivo* and *in vivo* conditions are necessary.

5.4.3 Utility of the new algorithm in practice

Before we conclude this chapter, some comments regarding the utility of the new algorithm in terms of performing its tasks are in order. First, the new algorithm has tremendously speeded up extraction data acquisition. The most impressive feature of the new algorithm is its apparent ability to correct fits performed using the 2-parameter model in ROIs where the OCT signal was influenced by absorption. Correcting 2-parameter OCT extraction results with use of the 3-parameter fit may reduce some degrees of technical bias in the current extraction technique. Ridding the method of such bias will make it more applicable for attaining our goal of quantitative, objective plaque characterization as outlined in [2].

Aside from descent performance, the new algorithm does have some drawbacks. Namely, the volume of data generated is enormous, and it can be quite bothersome to visually examine every single fit. A 'fit results filtration system' can be (and should be) easily implemented shortly to lessen the burden on the user. Furthermore, there are many ways to analyze the generated data. Of great importance to carrying out a systematic clinical study would be to have the data processing methods planned out ahead of time.

Still, our results in this section suggest that once mastered, the OCT extraction technique holds great potential for becoming a fast and accurate diagnostic tool.

6. Conclusion

The current study demonstrated that with use of the outlined algorithm, the optical properties of tissue may be obtained from optical coherence tomography images. The initial evaluation study on phantoms showed that OCT is capable of accurately determining the optical scattering properties, i.e., the scattering coefficient μ_s and effective anisotropy parameter g_{eff} , of highly scattering media, obtaining results in agreement with a well-established experimental method. Using this technique, we were able for the first time to conduct a preliminary investigation that quantitatively compared the optical scattering properties of the human arterial intima *ex vivo*. Our preliminary *ex vivo* aortic tissue data indicated that differences in scattering properties data may exist between normal and atherosclerotic arterial segments and that optical scattering data provided by OCT can potentially contribute to plaque characterization.

Extending our modeling to include absorption effects and subsequent numerical experiments revealed that in cases where absorption influences the OCT signal, additionally fitting the absorption coefficient μ_a reduces the error in extracting optical scattering properties and thereby improves their diagnostic value. Preliminary experiments on carotid lipid-rich plaques indicated that in some cases (13%), adding the third parameter can modify the extracted scattering parameters and that this correction may prove important in these particular cases. These assertions remain to be confirmed through continued follow-up experiments on phantoms and biopsies.

The OCT technique presented here opens many new avenues of research combining high-resolution tissue visualization and scattering properties measurements. This may allow for the assessment of yet unexplored biophysical properties of tissues and holds considerable promise for future clinical utility.

6.1 Perspectives

The diagnostic tool our group is aiming at is a fully-automated ‘clinic-friendly’ one command extraction algorithm. Getting to this step requires more efficient data-handling methods. One way to enhance this algorithm would be to employ an automatic alignment routine that would align the first pixel of the tissue surface in adjacent A-scans. Another technical advance should be implementing a ‘smart’ segmentation algorithm that delineates histological layers. With improved modeling, more OCT imaging systems (i.e., ultrahigh resolution OCT) could make use of this algorithm. And most importantly, for clinical usefulness, a database should be developed that relates different tissue pathologies to the corresponding optical property data.

Appendix A: Derivation of the OCT signal

This appendix provides a condensed overview of the derivation of the OCT signal. A more detailed version of this derivation (where absorption effects not included) is found in [22,27]. The extension of the model to include absorption effects [19] is as of yet unpublished; however, the main difference between both derivations is pinpointed here.

Calculating the mean square heterodyne signal current $\langle i^2(z) \rangle$ at the photodetector of an OCT system requires mixing of the sample field U_S with the reference field U_R . This is done with the use of mutual coherence function Γ , and can be expressed as [22,27]

$$\langle i^2(z) \rangle = 2\alpha^2 |g(\tau)|^2 \times \text{Re} \iint \Gamma_S(\mathbf{p}_1, \mathbf{p}_2; z) \Gamma_R(\mathbf{p}_1, \mathbf{p}_2) d\mathbf{p}_1 d\mathbf{p}_2, \text{ with} \quad (13)$$

$$\Gamma_S(\mathbf{p}_1, \mathbf{p}_2; z) = \langle U_S(\mathbf{p}_1; z) U_S^*(\mathbf{p}_2; z) \rangle, \text{ and} \quad (14)$$

$$\Gamma_R(\mathbf{p}_1, \mathbf{p}_2; z) = U_R(\mathbf{p}_1; z) U_R^*(\mathbf{p}_2; z). \quad (15)$$

Here, α is the power to current conversion factor, Re denotes the real part, \mathbf{p}_1 and \mathbf{p}_2 are two-dimensional vectors transverse to the optical axis, and the subscripts R and S represent the reference and sample arms, respectively. The integrations are over the area of the detector, and $\langle \cdot \rangle$ denote ensemble averaging over the (independent) statistical properties of the tissue and the diffusely reflecting discontinuity. Also, $|g(\tau)|$ is the modulus of the normalized temporal coherence function of the source. But in the case of interest, the optical pathlength of both arms of the Michelson interferometer are always matched, and from that it follows that $|g(\tau)| = |g(0)| = 1^*$ [27]. Note that in the reference arm the field is assumed to be constant at all depths.

In OCT, an optical beam probes a turbid medium with a unique μ_s , θ_{rms} , and refractive index n at a depth z where there is a diffuse refractive index discontinuity. As light returning to the mixing plane is diffusely backscattered, the discontinuity plane can be thought of as containing a plethora of point sources. It has been shown that mean backscattering irradiance profile $\langle I_B(\mathbf{r}) \rangle$ that can be estimated as [29,67]

$$\langle I_B(\mathbf{r}) \rangle = \frac{R_d P_S}{\pi} \left[\frac{\exp(-\mu_s z) \exp(-r^2 / w_H^2)}{w_H^2} + \frac{[1 - \exp(-\mu_s z)] \exp(-r^2 / w_S^2)}{w_S^2} \right], \quad (16)$$

with \mathbf{r} being a transverse vector in the discontinuity plane, and R_d the Fresnel reflection coefficient at depth z , respectively. The intensity from these point sources are delta-correlated in the backscattered field U_B [29,67].

To describe the propagation of an optical wave from the tissue discontinuity to the detector can be done using the extended Huygens-Fresnel Green's function $G(\mathbf{r}, \mathbf{p})$ which describes propagation through an arbitrary (real) ABCD system in the presence of random inhomogeneities [68,69]. The field in the output plane $U_S(\mathbf{p})$ is given by

$$U_S(\mathbf{p}) = \int U_B(\mathbf{r}) G(\mathbf{r}, \mathbf{p}) d\mathbf{r} = \int U_B(\mathbf{r}) G_0(\mathbf{r}, \mathbf{p}) \exp[i\phi(\mathbf{r}, \mathbf{p})] d\mathbf{r}, \quad (17)$$

where \mathbf{p} represents a transverse vector in the mixing plane. G can be further decomposed into the Huygens-Fresnel Green's function G_0 from the ABCD system

* Note $g \neq |g(\tau)| \neq g_{\text{eff}}$!

without the inhomogeneities and a phase distorting factor (resulting from the inhomogeneities) on the propagating spherical wave. The phase ϕ is assumed to be random, and the Huygens-Fresnel Green's function G_0 is [68]

$$G_0(\mathbf{r}, \mathbf{p}) = -\frac{ik}{2\pi B} \exp\left[-\frac{ik}{2B}(Ar^2 - 2\mathbf{r} \cdot \mathbf{p} + Dp^2)\right], \quad (18)$$

with k being the (center) free-space wavenumber, and A , B , and D being ABCD ray matrix elements of propagation through the random medium.

Mutual coherence functions such as those in Equation (14) represent the ensemble averaged cross-correlation of light returning from two points on the discontinuity plane, \mathbf{r}_1 and \mathbf{r}_2 [70]. From Equation (17) we see that light returning from each point has undergone a unique random phase distortion ϕ . Thus it is possible to define another mutual coherence function Γ_{pt} for a point source in the discontinuity plane and observed in the lens plane. Γ_{pt} , which includes the effects of the scattering inhomogeneities on the returning wavefront, can be written [67,68] and approximated [67,22,32] as

$$\Gamma_{pt}(\mathbf{p}_1, \mathbf{p}_2; \mathbf{r}) = \left\langle e^{[i(\phi(\mathbf{p}_1; \mathbf{r}) - \phi(\mathbf{p}_2; \mathbf{r}))]} \right\rangle \cong e^{-\mu_s z} + (1 - e^{-\mu_s z}) e^{-\frac{|\mathbf{p}_1 - \mathbf{p}_2|^2}{\rho_0^2}}, \quad (19)$$

with the right side being the approximation, and ρ_0 being the lateral coherence length of the reflected sample beam in the mixing plane. What remains to be done now is substituting Equations (14-19) into Equation (13), integrating, and simplifying. The resulting expression is Equation (3), which is given here again for completeness.

$$\langle i^2(z) \rangle = \langle i^2 \rangle_0 \Psi_s(z)$$

$$= \frac{\alpha^2 P_R P_S \sigma_b}{\pi w_H^2} \left[e^{-2\mu_s z} + \frac{4e^{-\mu_s z} [1 - e^{-\mu_s z}]}{1 + (w_S^2 / w_H^2)} + (1 - e^{-\mu_s z})^2 \frac{w_H^2}{w_S^2} \right]. \quad (20)$$

As briefly mentioned earlier, the basic procedure for including absorption effects in the theoretical model is almost the same. The one notable change is in the Huygens-Fresnel Green's function, which now becomes [34]

$$G_0(\mathbf{r}, \mathbf{p}) = -\frac{ik \exp(-ikL_0)}{2\pi B} \exp\left[-\frac{ik}{2B}(Ar^2 - 2\mathbf{r} \cdot \mathbf{p} + Dp^2)\right], \quad (21)$$

with L_0 being the total optical pathlength for a ray traveling along the optical axis. Specifically, $L_0 = \sum_j n_j L_j$ where j represents every individual element having a unique thickness L_j and complex refractive index n_j . Inserting this Huygens-Fresnel Green's function into Equation (14) and integrating results in a heterodyne efficiency factor that includes absorption effects and is given again here.

$$\Psi_{SA} = e^{-2\mu_a z} \left[e^{-2\mu_s z} + \frac{4e^{-\mu_s z} (1 - e^{-\mu_s z})}{(1 + \mu_a \Delta z_D)(1 + w_{SA}^2 / w_H^2)} + \frac{(1 - e^{-\mu_s z})^2 w_H^2}{(1 + \mu_a \Delta z_D)^2 w_{SA}^2} \right] \quad (22)$$

Appendix B: The extraction at the present

This appendix provides a detailed explanation of the extraction as of 28 May 2004. First, a detailed flow chart and table that explain the principles behind the algorithm are given in A.1. The commented codes are given in Appendix A.2 in their entirety.

A.1 Description of the algorithm

Altogether, the extraction algorithm is composed of eight codes. The parent code `extract` controls and coordinates seven children. Table 3 lists all the codes and explains their purposes, which are shown in Figure 20 where there is a graphical representation of how the codes interact with one another and with the user. For simplicity, Figure 20 is color-coded. The remainder of this appendix is an explanation to be used in conjunction with Table 3 and Figure 20.

As explained in the overview in Section 3.4.7, the user initiates the algorithm by typing ‘extract’ in the Matlab command prompt (top of Figure 20). A warning box appears telling the user to close all Matlab figures before continuing. After having done so and clicking ‘OK’, an ‘open-file’ dialog box prompts the user to select an OCT data file to be read by the file `readbinfilewithheader.m`. Unlike before, the user does not need to manually erase the header information from the binary file (an arduous task if analyzing hundreds of images). Preprocessing then takes place—the negative offset is removed and the signal is normalized. A large image appears on the screen, and the user is prompted to enter the number of transverse segments (N) to divide the image into. N initiates the ensuing FOR loop, and dictates how many cycles it will repeat.

Each cycle in the first FOR loop Figure 20 (middle of figure) begins with a plot of the averaged A-scan for that particular segment. Message boxes direct the user to zoom in on the part of the curve near the specular reflection (z_{peak}). The user keeps clicking on the part of the curve that represents z_{peak} as long as necessary, finishing by hitting ‘ENTER’—this is the `ginput` command. This identifies the pixel, which is stored and used in creating the z vector. In the same ‘zoom and click’ manner, the user then supplies graphical input for z_1 and z_2 , respectively. All these inputs axially delineate the ROI and form the z vector to be used during curve-fitting. Next, the code `fit_sa_gui.m` is called, which uses the `lsqcurvefit` routine to fit the averaged OCT signal from the ROI to the curve `psi_sa_gui.m`, the model that includes absorption effects. The returned μ_s , θ_{rms} , and μ_a are subsequently stored. Afterwards, the code repeats the fitting task, only this time using the code `fit_s_gui.m` to fit the 2-parameter model [22] found in the code `psi_s_gui.m`. Like in the previous case, the returned μ_s and θ_{rms} are stored. In both fitting routines, an IF clause is added, that sets all the returned values to zero should the fit attempt not converge or should the maximum number of iterations (500) or function evaluations (also 500) be reached.

Once the loop terminates, three *.txt files are saved, that are also used in the ensuing display routine (middle-right and bottom of Figure 20). These three *.txt files contain the result from the 3-parameter fit, the 2-parameter fit, and the boundary pixels for each ROI, respectively. All three files are read by the `fit_data_comp.m` code that is called once the files immediately after the files are saved. A second FOR loop is then initiated (bottom of Figure 20) for data display and storage. Like the first FOR

loop, N cycles are executed. In each cycle, the data points are plotted along with the results from both fits. An error parameter [%] is calculated using

$$100 \times \frac{1}{M} \sum_{j=1}^M (\Psi_{\text{measured}}(j) - \Psi_{\text{fitted}}(j)), \quad (23)$$

where M is the number of data points and Ψ_{measured} and Ψ_{fitted} the measured and fitted heterodyne efficiency factor, respectively. All the fitted parameters and error estimates from both fits are printed on this graph, along with a label containing the image filename and segment number. For each ROI, a fit-data comparison plot is exported as a *.jpg. Once this completes, a final routine is called that displays the original image with the ROIs outlined in red and lines corresponding to z_{peak} marked in blue. This image is also exported as a *.jpg, and the algorithm terminates.

Table 3: *.m files used in the new extraction algorithms and their tasks. Compare to ellipses with blue text in Figure 20.

*.m file	Task
extract	Interacts with user and coordinates all the *.m files
readbinfilewithheader	Removes header from data file and converts binary data into ASCII
fit_sa_gui	Performs 3 parameter fit to equation system in psi_sa_gui
fit_s_gui	Performs 2 parameter fit to equation system in psi_s_gui
psi_sa_gui	Equation system including absorption
psi_s_gui	Equation system excluding absorption
fit_data_comp	Receives 3 and 2 parameter fit results, calculates error, plots labeled results, and saves graphs as *.jpg files
img_roi_disp	Displays image with all the ROIs highlighted in red, and labels axial lines corresponding to z_{peak} in blue

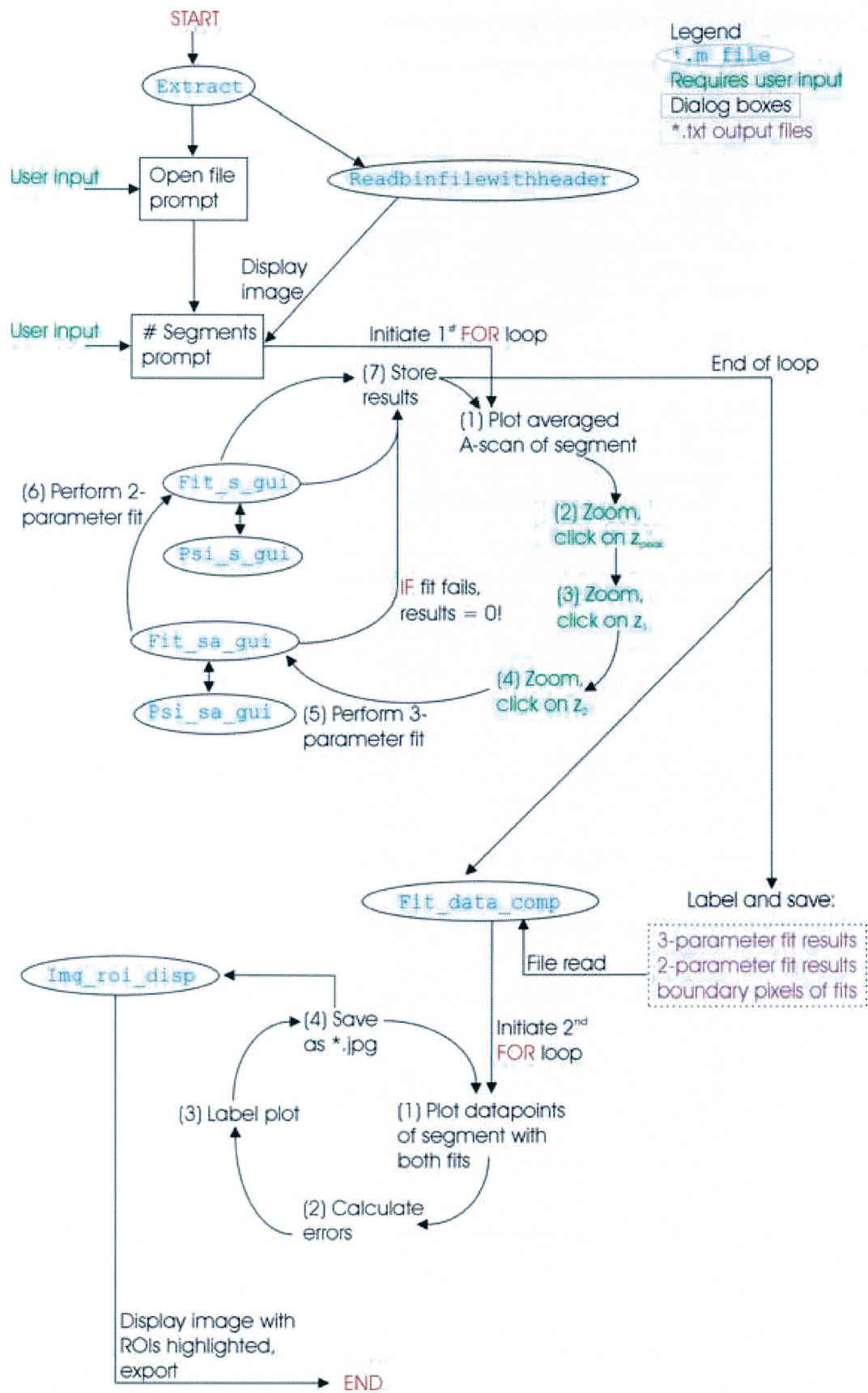


Figure 20: A detailed schematic of the new extraction algorithm. The tasks of *.m files (ellipses with blue text) are listed in Table 3.

Appendix B2: Codes of the extraction algorithm

```
function [] = extract

in_wrn = warndlg(...
    'make sure you have an "extraction output" folder with subfolders
    "fit images" and "numerical results"! ',...
    'extraction initiation warning');
waitfor(in_wrn);
[file, path] = uigetfile('*.dat', 'Select an OCT data file');
out_fol = 'extraction output\numerical results\'; % To be used in
saving output files later

x_max = 400;
z_max = 690;

% Load data file
data = readbinfilewithheader(file, z_max, x_max);
data = 1 + data - min(min(data));
datalog = log10(data);
datalog = datalog / max(max(datalog));
% datalog = 1 - datalog;
img = figure;
set(img, 'position', [50, 100, 800, 580]);
imagesc(datalog); colormap(gray);

% Get user input for number of extraction segments
prompt1 = {'How many extraction segments do you want?'};
title1 = 'Segment prompt';
lines = 1;
def1 = {'13'};
answer1 = inputdlg(prompt1, title1, lines, def1);
N = str2double(answer1);
close(img);

% Split into N segments, plot average A scans, obtain boundary pixels
information, and do 2 fits
for i = 1 :N
    x1 = 1 + round(x_max * (i - 1) / N);
    x2 = round(x_max * i / N);

    % Average A-scans, smooth, and plot
    avg_a_scan = mean(data(:, x1 : x2), 2);
    avg_a_scan = avg_a_scan';
    L = length(avg_a_scan);
    avg_a_scan(3 : L - 2) = smoothts(avg_a_scan(3 : L - 2)); % Smooth
    a_fig = figure;
    plot(avg_a_scan);
    set(a_fig, 'position', [25, 200, 600, 475]);

    % Prompt user for z_peak input
    z_msg = msgbox('zoom into the region of z_peak and click "ok"',
'zoom prompt');
    set(z_msg, 'position', [480, 460, 250, 75]); % Prompt for correct
zoom
    waitfor(z_msg);
    instr_msg = msgbox('click on the correct z_peak position. when
finished, hit "enter"', ...
    'Instructions prompt'); % Graphical input with mouse click
    set(instr_msg, 'position', [480, 460, 250, 75]);
```

```

[z_clicked, x_clicked] = ginput;
z_peak = round(z_clicked(end));
close(instr_msg);

% Prompt user for z1 input
z_msg = msgbox('zoom into the region of z1 and click "ok"', 'zoom
prompt');
set(z_msg, 'position', [480, 460, 250, 75]); % Prompt for correct
zoom
waitfor(z_msg);
instr_msg = msgbox('click on the correct z1 position when
finished, hit "enter"', ...
'Instructions prompt'); % Graphical input with mouse click
set(instr_msg, 'position', [480, 460, 250, 75]);
[z_clicked, x_clicked] = ginput;
z1 = round(z_clicked(end));
close(instr_msg);

% Prompt user for z2 input
z_msg = msgbox('zoom into the region of z2 and click "ok"', 'zoom
prompt');
set(z_msg, 'position', [480, 460, 250, 75]); % Prompt for correct
zoom
waitfor(z_msg);
instr_msg = msgbox('click on the correct z2 position. when
finished, hit "enter"', ...
'Instructions prompt'); % Graphical input with mouse click
set(instr_msg, 'position', [480, 460, 250, 75]);
[z_clicked, x_clicked] = ginput;
z2 = round(z_clicked(end));
close(instr_msg);

term_msg = msgbox('Close figure to continue. DO NOT click
"ok"', 'Instructions prompt');
waitfor(a_fig);
close(term_msg);

% Modify Average A scan and plot
avg_a_scan = avg_a_scan(z1 : z2); % Trim
avg_a_scan = avg_a_scan / max(avg_a_scan); % Normalize
log_avg_a_scan = log10(avg_a_scan); % Log

% Save file to be read by fitting program (necessary for semi-
automation)
M = [z_peak, z1, z2];
save 'intermediate.txt' M -ASCII -TABS
save 'shit.txt' log_avg_a_scan -ASCII -TABS

% Perform fits and save results
res_sa(i,:) = fit_sa_gui(log_avg_a_scan);
res_s(i,:) = fit_s_gui(log_avg_a_scan);
borders(i,:) = [x1, x2, z_peak, z1, z2]; % File with boundary
pixels
end

fit_data_comp(file, data, N, res_sa, res_s, borders);

img_roi_disp(file, datalog, N, x_max, z_max, borders);

% Create filenames for saving
fname_sa = strrep(file, '.DAT', '_results_sa.txt');

```

```

fname_sa = strcat(out_fol, fname_sa);
fname_s = strrep(file, '.DAT', '_results_s.txt');
fname_s = strcat(out_fol, fname_s);
fname_b = strrep(file, '.DAT', '_border_pts.txt');
fname_b = strcat(out_fol, fname_b);

save(fname_sa, 'res_sa', '-ascii');
save(fname_s, 'res_s', '-ascii');
save(fname_b, 'borders', '-ascii');

```

```

function data = readbinfilewithheader(filename,rows,columns);

fID = fopen(filename, 'r','ieee-be');
if fID == -1
    error('File could not be read. Check if you typed the filename
correctly')
end

for i=1:21,
    fgets(fID);
end

%read all file
data = fread(fID,[rows,columns], 'float');
fclose(fID);

```

```

function [Q] = fit_sa_gui(log_avg_a_scan)

lb = [0, -pi/2, 0]; % Lower boundary (mu_s, theta_rms, mu_a)
ub = [inf, pi/2, inf]; % Upper boundary
b0 = [10, 0.1, 0.1]; % Initial value guesses

% Obtain relevant z information
z_info = load('intermediate.txt');
z_peak = z_info(1);
z1 = z_info(2);
z2 = z_info(3);
z = linspace(0, 0.00416 * (z2 - z1), z2-z1 + 1);
z_offset = (z1 - z_peak) * 0.00416;
z = z + z_offset;

options = optimset('maxiter', 500, 'maxfunevals', 500);
[b, resnorm, fval, exitflag, output] = lsqcurvefit(@psi_sa_gui, b0,
z, log_avg_a_scan, ...
    lb, ub, options); % fit

% figure;
% plot(z, log_avg_a_scan, '*');
% hold on
% plot(z, psi_sa_gui(b, z), 'r');
% legend('data points', 'fit');
% title('fit-data comparison for curve including absorption');
% xlabel('depth [mm]');
% ylabel('log_1_0 (psi) [a.u.]');

mu_s_fitted = b(1);
theta_rms_fitted = b(2);
mu_a_fitted = b(3);

fit = 10 .^ (psi_sa_gui(b, z));
avg_a_scan = 10 .^ (log_avg_a_scan);

```

```

% back transform data for error calcs
max_err_pct = max(abs((avg_a_scan - fit) ./ fit)) * 100;
avg_err_pct = sum(abs((avg_a_scan - fit) ./ fit)) ./
(length(avg_a_scan)) * 100;

Q = [mu_s_fitted, theta_rms_fitted, mu_a_fitted, max_err_pct,
avg_err_pct];

% In case fit does not converge
if exitflag <= 0
    Q = [0, 0, 0, 0, 0] + 1e-6;
end

```

```

function [Q] = fit_s_gui(log_avg_a_scan)

lb = [0, -pi/2]; % Lower boundary (mu_s, theta_rms)
ub = [inf, pi/2]; % Upper boundary
b0 = [10, 0.1]; % Initial value guesses

% Obtain relevant z information
z_info = load('intermediate.txt');
z_peak = z_info(1);
z1 = z_info(2);
z2 = z_info(3);
z = linspace(0, 0.00416 * (z2 - z1), z2-z1 + 1);
z_offset = (z1 - z_peak) * 0.00416;
z = z + z_offset;

options = optimset('maxiter', 500, 'maxfunevals', 500);
[b, resnorm, fval, exitflag, output] = lsqcurvefit(@psi_s_gui, b0, z,
log_avg_a_scan, ...
    lb, ub, options); % fit

% figure;
% plot(z, log_avg_a_scan, '*');
% hold on
% plot(z, psi_s_gui(b, z), 'r');
% legend('data points', 'fit');
% title('fit-data comparison for curve without absorption');
% xlabel('depth [mm]');
% ylabel('log10(psi) [a.u.]');

mu_s_fitted = b(1);
theta_rms_fitted = b(2);

fit = 10 .^ (psi_s_gui(b, z));
avg_a_scan = 10 .^ (log_avg_a_scan);

% back transform data for error calcs
max_err_pct = max(abs((avg_a_scan - fit) ./ fit)) * 100;
avg_err_pct = sum(abs((avg_a_scan - fit) ./ fit)) ./
(length(avg_a_scan)) * 100;

Q = [mu_s_fitted, theta_rms_fitted, max_err_pct, avg_err_pct];

% In case fit does not converge
if exitflag <= 0
    Q = [0, 0, 0, 0] + 1e-6;
end

```

```

function signal_rms = psi_s_gui(beta,z)

mu_s = beta(1); % These are the fitting parameters we want to extract
theta_rms = beta(2);
%z_offset = beta(3);
%w0= beta(3);
%scaling = beta(3);
z1 = 380; % This is the start of the data to fit
z_peak = 377; % This is the position of the peak from the specular
reflection.
% z_offset = (z1-z_peak)*0.00416;
z_offset = 1e-6;
z = z + z_offset;

lambda = 1.31E-3; %wavelength in mm
n = 1.55; % refractive index
f = 16; % focal length in mm
w0 = 0.8; % inter lens beam waist radius in mm
%theta_rms = 0.05;
k = 2*pi/lambda;

% ABCD ray matrix elements
A = 1;
B = f + z / n; % fixed focus
% B = f * A; % dynamicm focusing

rho = sqrt(3./(mu_s*z)) .* lambda/(pi*theta_rms) .* (n*B./z); %
Lateral coherence length

wHSqrd = w0^2*(A - B/f).^2 + (B / (k*w0)).^2;
wSSqrd = wHSqrd + (2*B ./ (k * rho)).^2;
wSwH = wSSqrd./wHSqrd;

z_off = z(1); % NOTE: z_off here EQUALS z_offset in fit_sa_gui
c1 = (exp(-2*mu_s*z_off) + 2*exp(-mu_s*z_off).*(1-exp(-mu_s*z_off))./
...
(1+wSwH) + (1-exp(-mu_s*z_off)).^2./wSwH) .^ -1;
signal_sq = c1 .* (exp(-2*mu_s*z) + 2*exp(-mu_s*z).*(1-exp(-
mu_s*z))./ ...
(1+wSwH) + (1-exp(-mu_s*z)).^2./wSwH); %

signal_rms = sqrt(signal_sq);
signal_rms = log10((signal_rms)) ;

```

```

function signal_rms_sa = psi_sa_gui(beta, z)

mu_s = beta(1); % These are the fitting parameters we want to extract
theta_rms = beta(2);
mu_a = beta(3);
%w0= beta(3);
%scaling = beta(3);
% theta_rms = 0.45;
% mu_s = 10;

lambda = 1.31E-3; %wavelength in mm
n = 1.4; % refractive index
f = 16; % focal length in mm
w0 = 0.8; % inter lens beam waist radius in mm
%theta_rms = 0.05;
k = 2*pi/lambda;

```

```

fw0 = mu_a / (f / w0^2);
kw0f = mu_a / ((k*w0)^2 / f);

% ABCD ray matrix elements
A = 1;
B = f + z / n; % fixed focus
% B = f * A; % dynamic focusing

rho = sqrt(3./ (mu_s*z)) .* lambda/(pi*theta_rms) .* (n*B./z); %
Lateral coherence length

% new formulas for mu_a extraction
wHSqrd = w0^2*(A - B/f).^2 + (B / (k*w0)).^2;
del_zn = (z ./ (4 * (n^2) * (B.^2))) .* (w0^2 + 0.5*rho.^2);
del_zd = (z / (2*n^2)) .* ((w0/f)^2 + (1/(k*w0))^2 + (2 ./
(k*rho)).^2) ;
mzn = 1 + mu_a .* del_zn;
mzd = 1 + mu_a .* del_zd;
wSASqrd = (wHSqrd + (mzn).*(2*B./(k.*rho)).^2)./(mzd);
wSAwH = wSASqrd./wHSqrd;

% scaling factor
z_off = z(1); % NOTE: z_off here EQUALS z_offset in fit_sa_gui
B_offset = f + z_off/n ;
rho_offset = sqrt(3/(mu_s*z_off)) * lambda/(pi*theta_rms) *
(n*B_offset / z_off) ;
del_zn_offset = (z_off / (4 * (n^2) * (B_offset^2))) * (w0^2 +
0.5*rho_offset^2) ;
del_zd_offset = (z_off / (2*n^2)) * ((w0/f)^2 + (1/(k*w0))^2 + (2 /
(k*rho_offset))^2) ;
mzn_offset = 1 + mu_a * del_zn_offset ;
mzd_offset = 1 + mu_a * del_zd_offset ;
wHSqrd_offset = w0^2*(A - B_offset/f)^2 + (B_offset / (k*w0))^2 ;
wSASqrd_offset = (wHSqrd_offset +
(mzn_offset).*(2*B_offset/(k*rho_offset))^2)/(mzd_offset) ;
wSAwH_offset = wSASqrd_offset / wHSqrd_offset ;

sing_scatt_scal = exp(-2*mu_s*z_off) ;
x_term_scal = 4*exp(-mu_s*z_off) * (1-exp(-mu_s*z_off)) / (mzd_offset
* (1+wSAwH_offset)) ;
mult_scatt_scal = (1-exp(-mu_s*z_off)).^2 ./ (wSAwH_offset .*
mzd_offset) ;
signal_sa_scal = exp(-mu_a*z_off) * (sing_scatt_scal + x_term_scal +
mult_scatt_scal) ;
scal_fact = 1 / signal_sa_scal ;

% psi (z) with mu_a effects included
sing_scatt = exp(-2*mu_s*z);
x_term = 4*exp(-mu_s*z) .* (1-exp(-mu_s*z)) ./ (mzd .* (1+wSAwH)) ;
mult_scatt = (1-exp(-mu_s*z)).^2 ./ (wSAwH .* mzd) ;
signal_sa_sq = scal_fact * exp(-mu_a*z) .* (sing_scatt + x_term +
mult_scatt);
% signal_SS_sq = scal_fact * exp(-mu_a*z) .* sing_scatt; % single
scattering only

signal_rms_sa = sqrt(signal_sa_sq);
signal_rms_sa = log10(signal_rms_sa);

```

```

function [] = fit_data_comp(file, data, N, res_sa, res_s, borders)

```

```

% Strings to be used in data output
img_fol = 'extraction output\fit images\'; % Folder for saving .jpg
files
n = int2str(N);
sc = ' mu_s = ';
an = ' g = ';
ab = ' mu_a = ';
un = ' mm-1';
f3 = '3 parameter fit: ';
f2 = '2 parameter fit: ';
er = ' error = ';
ttl = 'Fit-data comparison for ROI ';

for j = 1 : N

    % Assigning border pixels correct names and values
    x1 = borders(j, 1);
    x2 = borders(j, 2);
    z_peak = borders(j, 3);
    z1 = borders(j, 4);
    z2 = borders(j, 5);
    z = linspace(0, 0.00416 * (z2 - z1), z2-z1 + 1);
    z_offset = (z1 - z_peak) * 0.00416;
    z = z + z_offset;

    % Assigning correct values for vectors containing fit results
    b_sa = res_sa(j, 1 : 3);
    b_s = res_s(j, 1 : 2);

    % Average A-scans and modify curves
    avg_a_scan = mean(data(z1 : z2, x1 : x2), 2);
    avg_a_scan = avg_a_scan';
    L = length(avg_a_scan);
    avg_a_scan(3 : L - 2) = smoothts(avg_a_scan(3 : L - 2)); % Smooth
    avg_a_scan = avg_a_scan / max(avg_a_scan); % Normalize
    log_avg_a_scan = log10(avg_a_scan); % Log

    % Convert results to strings
    s3 = num2str(res_sa(j, 1));
    g3 = num2str(cos(res_sa(j, 2)));
    a3 = num2str(res_sa(j, 3));
    e3 = num2str(res_sa(j, 5));
    s2 = num2str(res_s(j, 1));
    g2 = num2str(cos(res_s(j, 2)));
    e2 = num2str(res_s(j, 4));
    J = int2str(j);
    ttl = 'Fit-data comparison for ROI ';

    % Plot data and 2 fits
    f = figure;
        set(f, 'position', [200, 100, 750, 550]);
    plot(z, log_avg_a_scan, '*');
        hold on
        plot(z, psi_sa_gui(b_sa, z), 'k');
        hold on
        plot(z, psi_s_gui(b_s, z), 'r');
    st3 = strcat(f3, sc, s3, un, ' ', an, g3, ' ', ab, a3, un, ' ',
', er, e3, '%');
    st2 = strcat(f2, sc, s2, un, ' ', an, g2, ' ', er, e2, '%');
    legend('OCT data used in fit', st3, st2, 0);
        legend boxoff

```

```

    ttl = strcat(ttl, ' (' , J, ') of (' , n, ') in file [' ,
strrep(file, '.DAT', ' '));
    title(ttl);
        xlabel('Depth [mm]');
        ylabel('Log_1_0 (OCT signal) [a.u.]');

    % Add results to graphs
    z_pos = z(end) * 2 / 3;

    % Export plots
    img_name = strrep(file, '.DAT', '_');
    img_name = strcat(img_fol, img_name, J, '_of_', n, '.jpg');
    saveas(f, img_name);
end

```

```

function [] = img_roi_disp(file, datalog, N, x_max, z_max, borders)

% Modeify lateral boundary pixels
borders(1, 1) = borders(1, 1) + 1;
borders(end, 2) = borders(end, 2) -1;

% Assign names to 2 lateral and 3 axial pixels in each ROI
x1 = borders(:, 1);
x2 = borders(:, 2);
z_peak = borders(:, 3);
z1 = borders(:, 4);
z2 = borders(:, 5);

% Create an inverse gray-scale image in RGB
img = zeros(z_max, x_max, 3);
img(:, :, 1) = datalog;
img(:, :, 2) = datalog;
img(:, :, 3) = datalog;

for i = 1 : N
    % Delineate lateral ROI boundaries in red
    img(z1(i) : z2(i), x1(i) - 1 : x1(i) + 1, 1) = 1; % red left
    img(z1(i) : z2(i), x1(i) - 1 : x1(i) + 1, 2) = 0; % green left
    img(z1(i) : z2(i), x1(i) - 1 : x1(i) + 1, 3) = 0; % blue left
    img(z1(i) : z2(i), x2(i) - 1 : x2(i) + 1, 1) = 1; % red right
    img(z1(i) : z2(i), x2(i) - 1 : x2(i) + 1, 2) = 0; % green right
    img(z1(i) : z2(i), x2(i) - 1 : x2(i) + 1, 3) = 0; % blue right

    % Delineate axial ROI boundaries in red
    img(z1(i) : z1(i) + 2, x1(i) : x2(i), 1) = 1; % red top
    img(z1(i) : z1(i) + 2, x1(i) : x2(i), 2) = 0; % green top
    img(z1(i) : z1(i) + 2, x1(i) : x2(i), 3) = 0; % blue top
    img(z2(i) - 2 : z2(i), x1(i) : x2(i), 1) = 1; % red bottom
    img(z2(i) - 2 : z2(i), x1(i) : x2(i), 2) = 0; % green bottom
    img(z2(i) - 2 : z2(i), x1(i) : x2(i), 3) = 0; % blue bottom

    % Delineate ROI z_peak lines in blue
    img(z_peak(i) : z_peak(i) + 2, x1(i) : x2(i), 1) = 0; % red
z_peak
    img(z_peak(i) : z_peak(i) + 2, x1(i) : x2(i), 2) = 0; % green
z_peak
    img(z_peak(i) : z_peak(i) + 2, x1(i) : x2(i), 3) = 1; % blue
z_peak
end

```

```

% Display image
u = figure;
imagesc(img);
set(u, 'position', [50, 100, 800, 580]);

% Label ROI number on image
for i = 1 : N
    m = int2str(i);
    roi_label = strcat('ROI (' , m, ')');
    if z_peak < 11
        z_peak = 11; % To label plots where z_peak is too low
    end
    t = text(x1(i), z_peak(i) - 10, roi_label);
    set(t, 'color', [1, 0, 0]);
end

% Export image
img_fol = 'extraction output\fit images\'; % Folder for saving .jpg
files
img_lbld = strrep(file, '.DAT', '_ROI_label.jpg');
img_lbld = strcat(img_fol, img_lbld);
flabel = strrep(file, '.DAT', '');
ttl = strcat('Image of [' , flabel, ', with ROIs delineated (red) and
z_p_e_a_k's labeled (blue)');
title(ttl);
saveas(u, img_lbld);

```

Appendix C. Epoxy phantom recipe copied from the original word document

This is an addendum to a previous recipe by Johannes Swartling that is not presented here. To properly understand how to make these phantoms, his documentation should be read beforehand.

Epoxy phantoms for dummies

Addendum to notes on epoxy tissue phantom making

By David Levitz (March 24, 2004)

Original instructions by Johannes Swartling (sometime earlier)

Epoxy: Diglycidyl ether of bisphenol A (DGEBA) using an aliphatic amine hardener

Preparations

1) Figure out concentrations for each phantom

Some useful tips/example:

At 660 nm, μ_s ' scales as linearly $7.75 \text{ cm}^{-1} / (\text{mg TiO}_2 / \text{g epoxy})$.

So, if $g = 0.75$ (from Appl Opt paper), μ_s (660 nm) scales by $3.1 \text{ mm}^{-1} / (\text{mg/g epoxy})$, and thus $\mu_s \approx 3.1 * M(\text{TiO}_2) [\text{mg}] / 122 \text{ g epoxy}$

or, at 660 nm, $\mu_s [\text{mm}^{-1}] \approx 0,0254 * M (\text{TiO}_2) [\text{mg}]$

A similar argument can be used to predict μ_s (and μ_a) at other wavelengths, if the coefficient slope per concentration is known.

For a quick calculation, use the Excel file 'phantom_prep_recipe.xls'

Note: You only use 43 g hardener per phantom; so adjust concentration appropriately.

Saturation: Hardener solutions tended to saturate when more than 400 mg TiO_2 per 43 ml hardener was used. Similarly, the absorbing toner stock solution saturates at concentrations greater than 120 mg / 100 ml.

2) Make cuvettes

For each cuvette, you need 3 extra-large microscope slides (10 cm X 3 cm). Take the glass cutter and cut one of these slides into three pieces, about 3 cm long. Next, you make a sandwich: 1 whole slide + 2 of the pieces you just cut placed on the outside edges + another whole slide. Once you make (and align) the "sandwich", use 3 laundry clips to hold it together. Take an epoxy/hardener mix and glue all around the outside EXCEPT for a 3 cm opening, which you will later micropipette the phantom mix into. The glue should be applied with a match, and after applying it, the still wet "cuvette" should be held together using the 3 laundry-clips and dry for 24 hours.

Note: The epoxy/hardener glue mix you use is NOT the one to be used to make the phantoms. There are 2 small containers from which the 2 components are squeezed out (they are quite pasty), and they should be mixed with a match.

Tip: Make a handful of extra cuvettes. It is also recommended to calibrate your micro-pipette volume setting, so that you only need to empty it once to fill the entire cuvette. Practicing with water in an empty cuvette helps.

3) Oven

Find oven and reserve it for the day you will need it. There is one oven at the ground floor of the machine shop in a room on the far left.

Procedure

For each phantom you need 2 polypropylene cups + epoxy + hardener + TiO_2 + toner

Hardener bottle and stock solution should only be opened in fume hood!

Always wear latex gloves when handling epoxy or hardener!

1) Make concentrated absorber stock solution and put in US bath

Use 120 mg toner powder / 100 g liquid hardener. The measurements should be exact, and the solution should be kept in a capped flask. It is the flask that should be placed in the ultrasonic bath. A 250 ml solution should be stirred in the bath for about 2 hours.

Note: For the hardener, 1 ml \approx 1 g

Note: Not capping the flask tightly will screw up the phantoms- if hardener mixes with air, it will foam about 10 minutes after mixing with epoxy

2) For each phantom, make TiO₂+absorber solution in hardener, put in US bath

In this part, you will need to make a unique solution in a 170 ml *pre-labeled* polypropylene cup for each phantom. In each cup, mix:

- The proper amount of TiO₂,
- 43g hardener – mass of absorbing stock solution
- Absorbing stock solution

It's probably better to use a micropipette with the absorber stock solution. When the individual phantom solution is mixed, cap it and put it in the ultrasonic bath for some minutes (until solution looks homogeneous). If that doesn't work, shake the capped cup hard for a minute and see if dissolving increased; repeat as necessary.

Note: Sometimes the cups with hardener solution float in the US bath. Adding some weight to keep them from floating is recommended.

3) For each phantom, add epoxy, stir until homogeneous

When the cups come out of the ultrasonic bath, add the 122 g epoxy to the second *pre-labeled* phantom cup. Once the first cup done stirring, pour the hardener mix from the ultrasonic bath into the epoxy cup, and stir with a glass rod *slowly* until the solution is homogeneous. Stirring may take up to 45 minutes (or even more); you will not be done until the consistency is uniform throughout the phantom. You may discard the first cup. A watch nearby may be useful but may also scare you (I recommend bringing a book or a second person to help or chat for this part). Phantom consistency is important; you don't want any air bubbles in there. Once you're done stirring, take the glass rod out, wait 1 minute, and stir again for another minute.

Note: 1 full tablespoon of epoxy \approx 25 g epoxy, and it's difficult to get exact measurements. Add the last few g of epoxy by letting them drip off a glass rod.

4) Put 1 ml sample in cuvettes

Micropipette about 1 ml of each phantom into the cuvettes you prepared earlier. Be careful not to spill any phantom and make sure to avoid air bubbles; place the micropipette tip inside the cuvette during injection. Practice some a few times beforehand, it may be useful to slowly move the micropipette across the slab opening as you inject the mix into it. The cuvettes should be left standing right side up, and will NOT need to be baked in the oven. If you see air bubbles in there, try tapping them out with your finger. Any spilling of phantom onto the side of the microscope slides should be cleaned up- it will screw up integrating sphere measurements.

5) Wait 12-16 hours, put in oven for 24 hours

After 12-16 hours, place phantoms on tray and take to oven in machine shop. Heat the samples at 55-60 °C for 24 hours, remove, and machine if necessary.

Additional notes: At room temperature, some particles- either toner or TiO₂ or microspheres- clump together, which will effectively change the scattering parameters. Also, some papers (i.e. Firbank et al 1993) claim TiO₂ has large variations in particle size. More should be looked into that.

References:

Original phantom recipe

- M Firbank and DT Delpy, “A design for a stable and reproducible phantom for use in near infra-red imaging and spectroscopy”, *Phys Med Biol* **38**, p. 847-853, 1993.
- M Firbank, Motoki Oda, and DT Delpy, “An improved design for a stable and reproducible phantom for use in near infra-red imaging and spectroscopy”, *Phys Med Biol* **40**, p. 955-961, 1995.

Spectroscopic calibration of this version in visible-NIR range

- J Swartling, JS Dam, and S Andersson-Engels, “Comparison of spatially and temporally resolved diffuse reflectance measurement systems for determination of biomedical optical properties”, *Appl Opt* **42**, p. 4612-4620, 2003.

Appendix D: Example of an input *.mci file into the Monte Carlo code

This is an example input file for the GMCML code. To repeat the experiment, all parameters in black should be kept constant. Red color text represents variables that change for each run.

```
#####
# Template of input files for Monte Carlo simulation (mcm1).
# Anything in a line after "#" is ignored as comments.
# Space lines are also ignored.
# Lengths are in cm, mua and mus are in 1/cm.
#####
#
1.0                # file version
1                 # number of runs
#
### Specify data for run 1
exps0.mco        A                # output filename, ASCII/Binary
# output irr y/n(1/0)    maximum radius    number of intervals    filename
0                0.135              1000                    g.txt
0 g93mys0.bin      # flag for saving the data of each individual photon
that exits at the bottom

# output pathhist y/n(1/0) 'aperture diameter' 'minimum path length' 'maximum path length'
resolution in wavelengths probe depth    filename
                1                3.0        3.188                3.7
                0.5              0.06       c0.95-6.txt

0                octtestS0.txt    0.00127869 # flag and filename and coherence length of the source
for calculating and saving detected OCT-signal

0                exit.txt        # flag for saving the data of each individual photon
that exits at the top

0.08              # 1 over e radius in cm
1.6               # focal length in cm
0.000131         # wavelength in cm
1.54             # distance from lens to medium
500000000       # No. of photons
0.01            0.01            # dz, dr
10              10              1          # No. of dz, dr & da.
#
2                # No. of layers
# n              mua            mus            g            d            # One line for each layer
1.0              # n for medium above.
1.0              2.5            50.0          0.92         0.06         0         1.0         1.0         # layer 1
1.0              0.0            0.0           0.99         0.05         1         1.0         1.0         # layer 2
5.0              # n for medium below.
```

Appendix E: A beginner's guide to atherosclerosis

Before describing the disease in detail, it is important to establish what a normal arterial wall looks like. In general, the vessel wall is made up of three concentric layers: The intima, the media, and the adventitia, as shown in Figure 21. The intima and adventitia are primarily collagen, and the media is made up of smooth muscle cells. Separating these three layers are the internal and external elastic membranes, which are mainly composed of elastin (see Figure 21). Although all arteries have this general structure, arteries can be further histologically classified based on their function. Small arteries, i.e., the coronaries, are muscular arteries, where the internal and external elastic membranes laminae are very thin, distinct, and well-defined. Bigger vessels, such as the aorta and the carotid arteries are elastic conducting arteries, and the internal and external elastic membranes are quite thick and loosely defined [71].

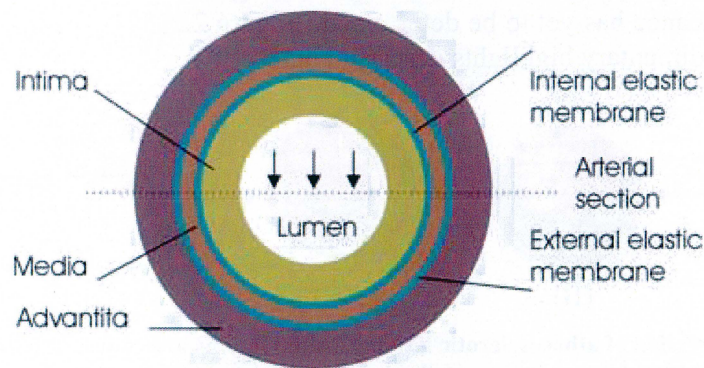


Figure 21: Cross-section of the normal vessel. The internal and external elastic membranes separate the three layers of the arterial wall- the intima, media, and adventitia. The dotted line indicates where sections are cut prior to histological processing. Arrows show the direction of imaging (i.e., lateral scans) using an OCT probe.

Approximately in the teenage years of one's life, the vessel wall begins to alter and the disease of atherosclerosis begins. Atherosclerosis is a complicated disease that evolves over decades, with no clear sequential order of events [59]. Likewise, the paradigm describing the disease is constantly changing. However, there are some general loose guidelines that are agreed upon in the community for how this disease progresses, which are described here.

There is no clear opinion on how the disease starts [59], but what is agreed upon is that a smooth muscle cell crosses the internal elastic membrane and ends up in the intima causing an injury [71], and this injury generates an immune response causing the intima to thicken. Macrophages begin to insudate the site, and an initial 'fatty streak' is formed. With time, more collagen is synthesized and the lumen narrows, the macrophages die and are replaced by new ones, and their lipid-rich atheromatous content full of low-density lipoprotein (LDL) is released into the extracellular matrix. Some lesions are stable grow in size but remain structurally stable; the narrowed lumen cannot deliver the required blood to the target organ, resulting in pain. PCI attempts to alleviate this pain.

However, other fatty streaks accumulate debris, and a lipid-pool forms. This necrotic core grows with time collecting debris, thereby altering the mechanical properties of the vessel. As the lipid-pool grows, the necrotic core becomes separated from the lumen by a collagen-rich fibrous cap. When this cap gets sufficiently narrow

(shoulder regions of the plaque are particularly susceptible), i.e., $< 65 \mu\text{m}$, the plaque becomes vulnerable and is predisposed to rupture [59]. Plaque rupture releases all the accumulated lipid and LDL into the lumen and an occlusive thrombus (clot) forms. What makes these thin cap fibroatheromas so dangerous is that often they do NOT compromise the lumen of the vessel, and many patients are not even aware they are at risk.

At this point, the vessel has become either partially or totally occluded. Total occlusions mean the target organ has an infarction; if the target organ is the heart is called a heart attack, if it is the brain this is called a stroke. Should the vessel not be completely occluded, a stabilizing healing process takes place, but inevitably the plaque keeps growing and this process is repeated [59]. Often, this inevitably results in sudden coronary death. In addition to atherogenesis described here, calcium deposits also may appear in the vessel wall throughout this process, although their clinical significance has yet to be determined. Figure 22 [59] gives some sketches of some of the rudimentary highlights described here.

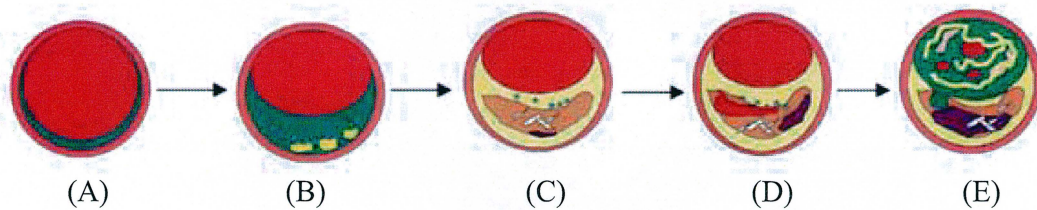


Figure 22: Progression of atherosclerotic lesions. Initial lesions are characterized by a thickening of the intima resulting from collagen synthesis (A). This site generates an immune response and some initial extracellular lipid deposits manifest themselves as a fatty streak (B). In some lesions (over considerable time) lipid accumulation forms a necrotic core (orange in (C)) that compromises the structural integrity of the vessel wall. A neointima is then formed (D), which may contain a thrombus, hemorrhage, or calcifications. Following plaque rupture, the vessel is completely occluded (E), causing an infarction in the target organ. Sketches from [59].

Of great importance is the role of collagen in this process. Collagen provides architectural stability and tensile strength to the vessel wall and increased collagen synthesis is an important determinant of plaque growth. Collagen thus constitutes the major extracellular matrix protein of plaques and accounts for the bulk lesion volume. Even more importantly, rupture of the collagen-rich fibrotic cap is the immediate precursor of atherothrombotic events (i.e., acute myocardial infarction). Assessment of the quantity and organization of collagen in atherosclerotic lesions *in vivo* may therefore provide significant pathophysiological information and influence clinical decision-making in patients with risk factors or overt atherosclerotic disease.

Appendix D.1: The endarterectomy procedure

This sub-appendix will briefly describe the endarterectomy procedure that removes dangerous plaques from the carotid artery. The highlights of the procedure are shown in Figure 23 [60]. Following administration of anesthesia, the doctor makes a cut in the neck. An incision is made along the carotid artery, the plaque is excised, and the artery is sewed shut. An example of a plaque removed before and after being sectioned into small biopsies is found in Figure 24(A-C).

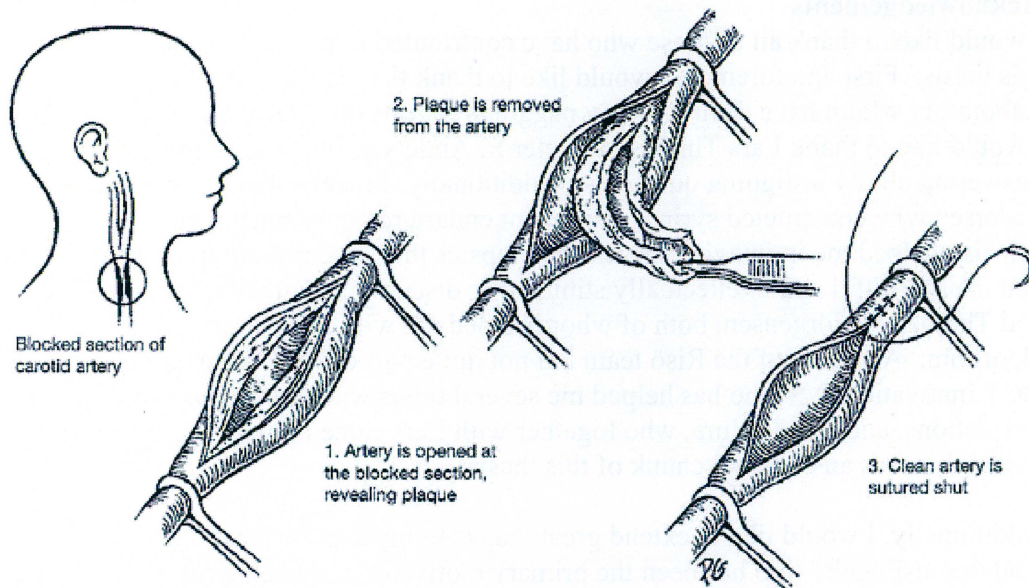


Figure 23: The basics of the endarterectomy procedure. The cylindrically shaped plaque removed in step two is the piece from which biopsies were cut. From [60].

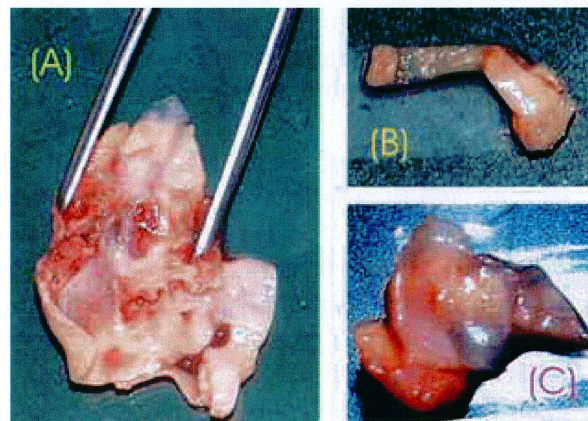


Figure 24: Human carotid atherosclerotic plaque removed via endarterectomy. (A) An excised carotid plaque (see step 2 of Figure 23) cut and held open; total length ≈ 7 cm, total diameter ≈ 1 cm. This large plaque was cut into several smaller biopsies ~ 7 mm \times 7 mm, exemplified in (B-C). The patient was a male in his late 60s.

Acknowledgements

I would like to thank all of those who have contributed in carrying out the research for this thesis. First and foremost I would like to thank the team at Risö National Laboratory whom have dealt with my nagging requests on a daily basis. Specifically, I would like to thank Lars Thrane and Peter E. Andersen for supervising me and answering all my intriguing questions. Additionally, I received help from Finn Pedersen who constructed syringes to mount endarterectomy specimen, and whom has also helped me in imaging the mouse biopsies that I did not report on here. I have had many fruitful and intellectually stimulating discussions with Michael H. Frosz and Thomas M. Jörgensen, both of whom helped me with programming the extraction algorithm. Also part of the Risö team but not quite part of Risö are Andreas Tycho of OCT Innovation A/S who has helped me several times with the Monte Carlo simulations, and Hal T. Yura, who together with Lars came up with the absorption model that was an essential chunk of this thesis.

Additionally, I would like to extend great thanks to my supervisor in Lund, Stefan Andersson-Engels, who has been the primary motivator convincing me to extract μ_a . Also helpful was Johannes Swartling of Polimi Inst., Italy, who left behind a phantom recipe which I used to prepare the low albedo phantoms, together with the beautiful Disa Holmlander. I have also had nice discussions on numerical methods with Tommy Svensson of LTH. Jurga Valanciunaite of Vilnius University assisted with characterizing the high-albedo phantoms using the integrating sphere. Nazila Yavari transported the failed poisonous phantoms for me, and I thank her for doing that dirty deed. A special thanks to Tomas Brage and Carl-Erik Magnusson, who accepted me for studies here in Lund and without whom I would not be here today.

Of course, I greatly appreciate the help of my clinical collaborators Peter R. Hansen of Amtssygehuset i Gentofte, and Lars Bo Nielsen, Claus B. Andersen, and Karin Rasmussen of Rigshospitalet. Peter was the one who started this whole project and put me in touch with the other medical doctors. Lars Bo provided me with endarterectomy samples, which I used for imaging. Claus obtained us the aortic biopsies and did all the histopathological characterization. Seeing the aorta at RH made me the vegetarian I am today. And Karin got us the two mice, Sporty Joe and Fat Bastard, which we dissected. Unfortunately they were not useful for this thesis. My sincerest apologies go to the friends and family of Fat Bastard, it is quite unfortunate his remains were left in the fridge.

Additionally, I would like to thank my officemates, Morten Fruelund, Laura Pastor, Ronnie Nilsson, Dennis Kristensen of Risö National Laboratory and Daniel Bengtsson and Khaled Terike for all the brilliant trash-talking conversations we have had over the past year. Special thanks go to Laura, who left many beers in the fridge of our Risö office which made a few nights fun that would otherwise have been boring. And to Ronnie, who competed with me for spending the most consecutive time at Risö, I can now say that my 56 hours crushed your 40.

This work was funded by the BIOP Graduate School, with some assistance from the Danish Heart Foundation.

Paper I

Assessing blood vessel abnormality via extracting scattering properties from OCT images

David Levitz^{*1,2}, Claus B. Andersen³, Michael H. Frosz¹, Lars Thrane¹, Peter R. Hansen⁴, Thomas M. Jørgensen¹, and Peter E. Andersen¹

⁽¹⁾ Optics and Fluid Dynamics Department, Risø National Laboratory,
PO Box 49, DK-4000, Roskilde, Denmark

⁽²⁾ Department of Physics, Lund University, PO Box 118, SE-221 00, Sweden

⁽³⁾ Department of Pathology, Rigshospitalet, Frederik V's Vej, DK-2100 København
Ø, Denmark

⁽⁴⁾ Department of Cardiology, Gentofte University Hospital, Niels Andersenvej,
DK-2900, Hellerup, Denmark

ABSTRACT

Background: Coronary artery disease (CAD) is the leading cause of mortality and morbidity in the industrialized world. Optical coherence tomography (OCT) is a high-resolution intravascular imaging technology with a potential for *in vivo* plaque characterization. Although structural remodeling of the arterial vessel wall during plaque development can change tissue optical scattering properties, very limited evidence is available on the exact optical scattering properties of plaques. The scattering coefficient, μ_s , and the anisotropy factor, g , can be derived from OCT images by fitting a theoretical model to individual depth-scans. The aim of the current study was to use this method to examine by OCT the scattering properties of human arteries with different stages of atherosclerotic lesion development. **Methods:** Normal ($n=4$), lipid-rich ($n=4$), and fibrous ($n=3$) aortic blocks as classified by parallel histopathologic examination were obtained within 24 hours of death and imaged by OCT. The intima was located in the OCT images, and then further split into 115 blocks (41 normal, 40 lipid-rich, and 34 fibrous) of adjacent OCT depth-scans transversely spanning ~ 200 - $300 \mu\text{m}$. Scattering signals from each block were averaged and fit to the theoretical model. From these fittings, μ_s and g were extracted. **Results and Discussion:** The optical scattering properties of normal aortic intima were quite different from lipid-rich and fibrous lesions, respectively. We discovered that the normal intima was generally highly forward scattering, i.e., with $0.917 < g < 1.00$, while diseased vessels were much less so. Furthermore, normal vessels usually had $15 < \mu_s < 39 \text{ mm}^{-1}$, whereas lipid-rich blocks had $\mu_s < 15 \text{ mm}^{-1}$. Fibrous blocks displayed large variations in μ_s , reflecting a histopathology with varying amounts of collagen, lipids, and elastin. Based on our findings, we defined a criteria of μ_s and g for normal intimas, using the above values of μ_s and g as cutoffs. Our "normal" criteria demonstrated high sensitivity (92.4%) and specificity (82.4%). We conclude, that a detailed analysis of the tissue optical scattering properties can enhance the capacity of OCT to provide information about vascular pathology.

Keywords: Optical coherence tomography, atherosclerosis, scattering properties

1. BACKGROUND

Coronary artery disease (CAD) is the leading cause of mortality and morbidity in the industrialized world, accounting for over 7 million deaths per year globally.¹ CAD is the result of atherosclerosis, and CAD patients are prone to experiencing acute coronary syndromes, i.e., acute myocardial infarction (AMI or heart attack), unstable angina pectoris, or sudden cardiac death. Atherosclerotic lesions progress from early lipid-laden fatty streaks, over intermediate lesions with extracellular lipid deposits covered by a fibrous cap, to mature plaques characterized by a thick neointima and fibrocalcific vascular remodeling. Collagen provides architectural stability and tensile strength to the vessel wall and increased collagen synthesis is an important determinant of plaque growth. Collagen thus constitutes the major extracellular matrix protein of plaques and accounts for the bulk lesion volume. Even more importantly, rupture of the collagen-rich fibrotic cap is the immediate precursor of atherothrombotic events (i.e., acute myocardial infarction). Assessment of the quantity and organization of collagen in atherosclerotic lesions *in vivo* may therefore provide significant

* Correspondence: E-mail: lars.thrane@risoe.dk, telephone +45 46 77 45 29; fax: +45 46 77 45 65

pathophysiological information and influence clinical decision-making in patients with risk factors or overt atherosclerotic disease.

Optical coherence tomography (OCT) is a new imaging technique in which backscattered light from the tissue is interfered with a reference wave, utilizing a technique known as low-coherence interferometry.² With an axial resolution between 1-20 μm , OCT has recently demonstrated its ability to visualize vessel histopathology at unprecedented levels of resolution and preliminary data have indicated that it is possible by OCT to distinguish between normal arteries, and fibrous, fibrocalcific, and lipid-rich plaques,^{3,4} as well as to quantify plaque macrophage content⁵ and to assess the success of intracoronary stent implantation in patients with CAD during percutaneous intracoronary intervention (PCI).⁶ However, because of technical limitations, differentiating between the three types of plaques (i.e., fibrous, fibrocalcific and lipid-rich lesions) by OCT is at present difficult, and no general consensus exists on the interpretation of OCT images of coronary pathophysiology. Such consensus would be important in order for a valid OCT technology to become clinically applicable and potentially adopted into future treatment guidelines for patients with CAD.

In an attempt to facilitate the interpretation of OCT images of the normal and diseased artery wall, it is important first to consider the histopathological alterations that occur in the vascular wall during plaque development. This process involves changes of the vessel wall architecture, cellular content, extracellular matrix organization and biochemical composition. Although these alterations may occur throughout the arterial wall during lesion progression, they first and foremost affect the inner intimal layer of the vessel wall, which is adjacent to the blood stream and readily assessable for OCT interrogation during percutaneous intraarterial procedures. Specifically, a reorganization of intimal collagen fibers is likely to produce in changes intima's optical scattering properties, i.e., the scattering coefficient, μ_s , and anisotropy parameter, g .

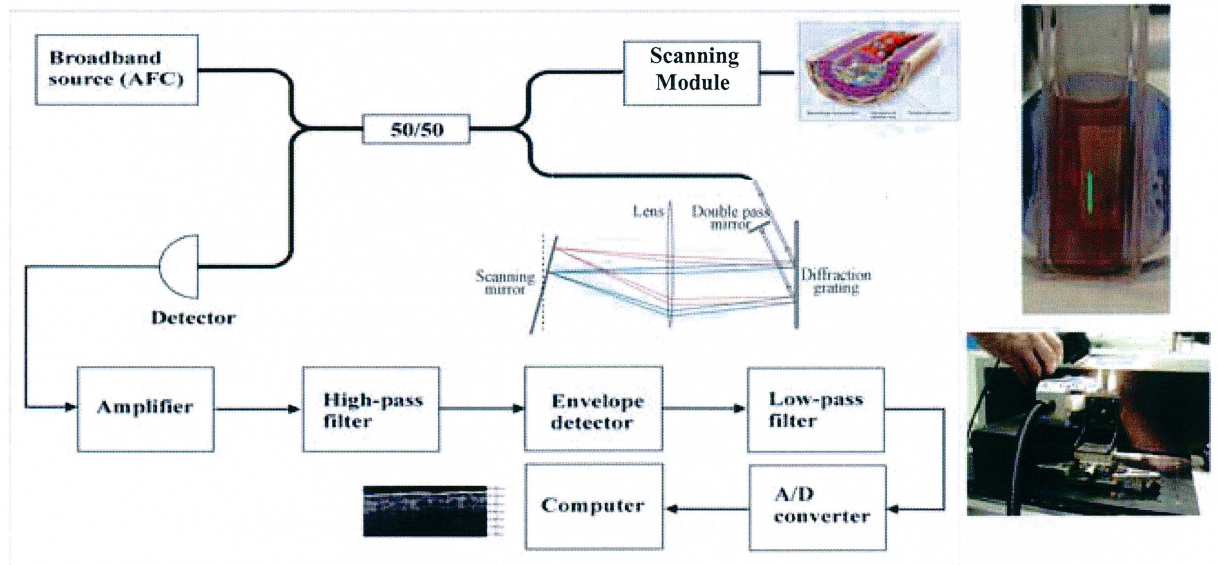


Figure 1: A schematic of the OCT system used in the experiment (left) and photographs of the sample mounting (right above and below). In the upper right, the sample in the cuvette is shown, with the region imaged by OCT marked by the line. The photo in the lower right is a side view of the cuvette mounted on translation stages facing the scanner on its left.

A theoretical model has previously been developed at Risø National Laboratory, Denmark⁷ to analyze light propagation in highly scattering tissue and predict the resulting signal levels when measured with an OCT system. Derived from the extended Huygens-Fresnel Principle⁸ this model includes multiple scattering effects, enabling analysis of deeper ($>300 \mu\text{m}$) tissue structures. Because this model is also based on ABCD matrix formalism, it is more easily applicable for analyzing tissues with multiple layers. By examining the scattering parameters of the imaged tissue using this model, it is possible to predict the signal in a single depth-scan (A-scan). Conversely, by fitting this model to a curve from an A-scan, it may be possible to extract the scattering properties. The goal of the present study was to implement this theoretical modelling in the interpretation and analysis of OCT images of human

atherosclerotic lesions, and compare our quantitative results with qualitative ones that are presently found in the literature.^{3,4}

2. METHODS

Imaging

For this study, the OCT system (see Figure 1) used an AFC broadband source operating at 1310 nm yielding an axial resolution of 10 μm in tissue; the lateral resolution was 26 μm . Fast depth scanning (about 100 A-scans per second) was achieved with a Fourier domain rapid-scanning optical delay line in the reference arm. A computer controlled fast-scanning module with an integrated digital video camera was incorporated into the sample arm to simplify transverse scanning. In this investigation, images with 690 axial pixels (4.16 μm spacing) and 400 transverse (10 μm spacing) pixels were generated. Image acquisition time (from start of scanning) was approximately 5-6 seconds. The dynamic range of the system was >100 dB.

11 (4 normal, 4 lipid-rich, and 3 fibrous) aortic segments were obtained within 24 hours of necropsy and imaged with OCT in phosphate buffered saline (PBS). Regions corresponding to those imaged with OCT were marked and located on photos from the digital camera. The samples were fixed in 10% formalin solution for >48 hours, were routinely processed for paraffin embedding, and 4 μm thick sections were sliced at the regions as shown by the digital photographs and stained with hematoxylin and eosin (H&E) or combined elastin and Van Gieson Hansen stains. Next, the intima was identified and measured in the histological sections. Using these measurements and criteria listed in references 3 and 4, the intima was identified in the OCT images for use in image post-processing.

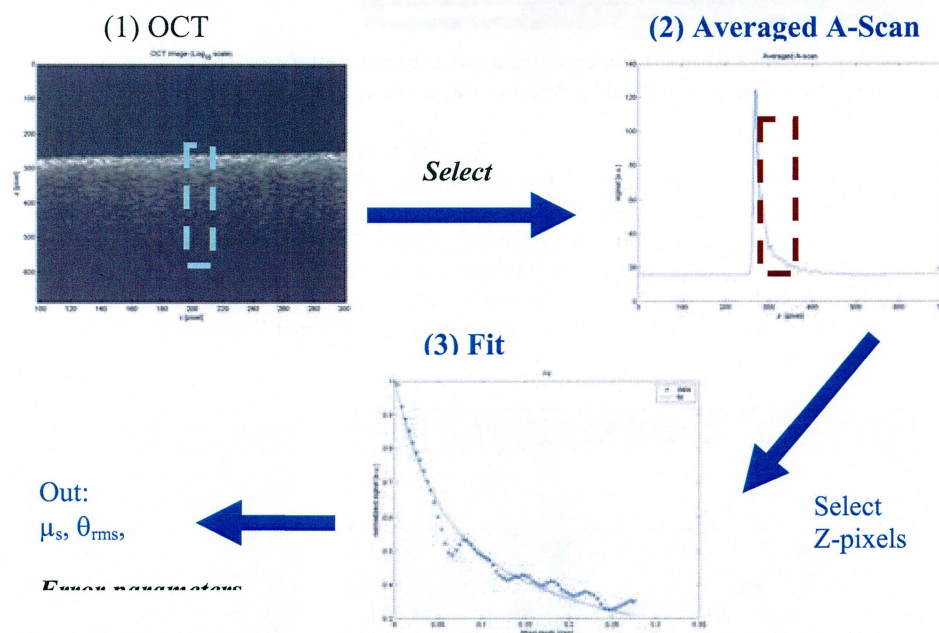


Figure 2: a schematic of the OCT image post-processing algorithm.

OCT image processing

We have developed an algorithm in Matlab for the purpose of this analysis. Principally, this algorithm first took a region x by z pixels long (selected by the user), applied linear smoothing, and averaged them along the transverse (x) direction, yielding a single smoothed, "averaged A-scan" curve. Pixels in the z direction corresponding to the boundaries of the fitting region were selected. To account for signal broadening from specular reflection of the PBS-tissue interface, the z -pixel marking the interface was selected, and it along with nearby pixels were excluded from the fit. Imaging conditions (i.e. light focusing on the tissue surface) were also incorporated into the model. A nonlinear fitting algorithm attempted to fit this curve to the aforementioned model, and output the scattering coefficient μ_s , the root-mean-square scattering angle θ_{rms} ($g = \langle \cos \theta_{rms} \rangle$) and the error of the fit. A schematic representation of the algorithm is shown in Figure 2.

The OCT images were divided along the transverse direction into blocks spanning approximately 20-30 A-scans (correlating to 200-300 μm). Altogether, the images were subdivided into 114 blocks (41 normal, 40 lipid-rich, and 34 fibrous) for fits. Selecting the correct z-pixels on the curve was not trivial. Boundaries of the intima were easily identifiable in images of a normal artery, and the final z-pixel in the fitting region was chosen to be the one before the peak associated with the intima-internal elastic membrane (IEM) interface. In the lipid-rich and fibrous vessel images, it was much more difficult to identify an end pixel, as the intima-IEM interface was destroyed by the lesion's presence. To accommodate this, the final pixel for the fit was chosen as the first pixel within 2 dB of the noise floor. In all cases, we made sure that the sum of the length of the fitting region and that of the interface broadened region did not exceed the intimal thickness as measured by histology.

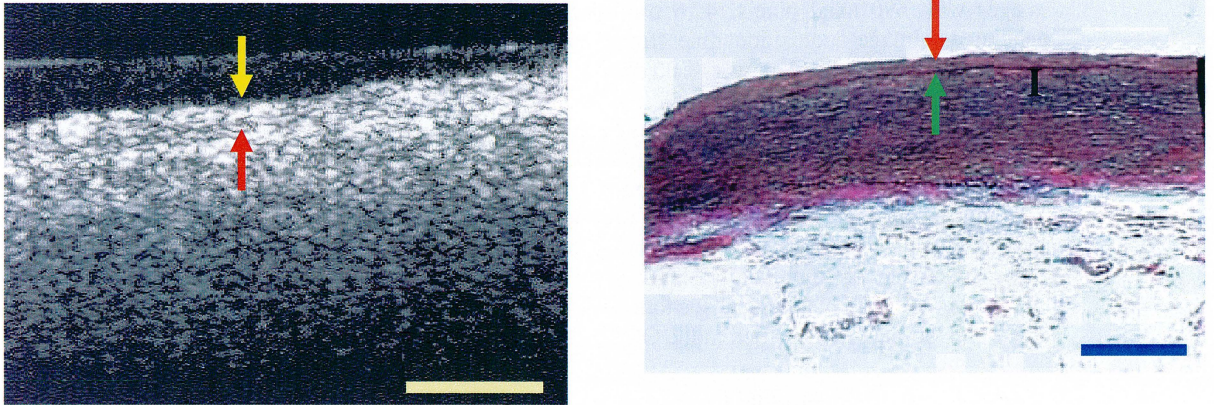


Figure 3: OCT (left) and histology (right) of a normal artery. The intima (I) is identified in both images, and its depth is marked by arrows. Bar represents 500 μm .

3. RESULTS

OCT images were correlated with the corresponding histological sections, and an example of each correlation can be found in Figures 3, 4, and 5. Qualitatively, our OCT images were comparable to OCT images obtained with similar systems by others.^{3,4} By microscopic morphometric assessment of the histological sections, the intima thickness measured 84 μm , 450 μm , and 520 μm for normal vessels, lipid-rich lesions, or fibrous lesions, respectively. These respective intimal layers corresponded to 22 pixels, 119 pixels, and 137 pixels, and served as the upper limits on the fitting plus the broadened region as described above.

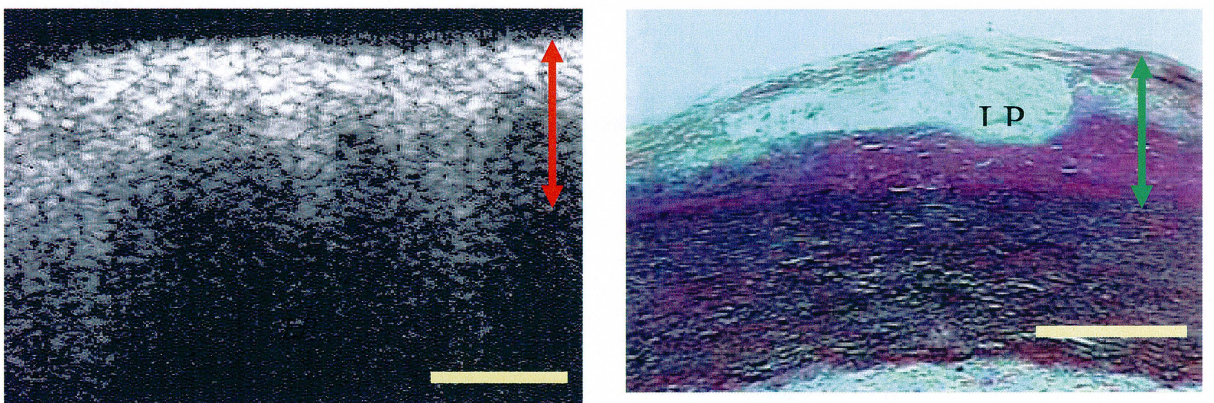


Figure 4: OCT (left) and histology (right) of lipid-rich plaque. A lipid pool can be seen in both images (LP). Arrows marks the intima. Bar represents 500 μm .

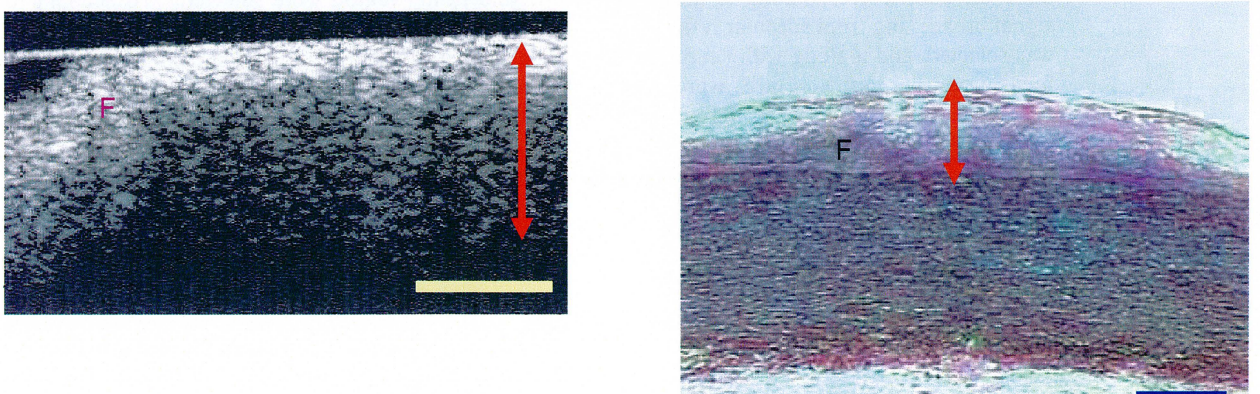


Figure 5: OCT (left) and histology (right) of a fibrous plaque. The plaque can be seen in both images (F). Arrows mark intima. Bar represents 500 μm .

A display of the distribution of respective μ_s and g values for blocks of the three intima types (i.e., normal vessels, lipid-rich lesions, or fibrous lesions) is illustrated in Figures 6 and 7. To facilitate interpretation, the scattering data was grouped according to a suitable scale, i.e., for μ_s , a scale divided in intervals spanning 5 mm^{-1} (from 0 to 40 mm^{-1}), or 10 mm^{-1} (above 40 mm^{-1}). Since tissue is generally very forward scattering, intervals of 0.05 were preselected for g approximating 1, but these intervals were subsequently extended below 0.8 because of a relative absence of g values in those ranges. As shown in Figure 6, 36 of 41 (87.8%) normal arterial blocks had a μ_s value between 15 and 35 mm^{-1} , while 31 of 40 (75%) lipid-rich blocks had a μ_s value under 20 mm^{-1} . In contrast, the distribution of μ_s values for fibrous lesions was inconsistent, and no pattern of scattering values could be established for these lesions. As demonstrated in Figure 7, 36 of 41 (87.8%) normal arterial blocks displayed a g value between 0.95 and 1, while 52 of 74 (70.2%) lipid-rich and fibrous lesions had g values that fell outside this range.

4. DISCUSSION

To our knowledge, the current study represents the first analysis of the optical scattering properties at 1300 nm of the human arterial intima. The main finding was that the intimal layer of different normal arteries consistently demonstrated very similar optical properties. Hence, every normal arterial block had a g value between 0.9 and 1, with g values in normal arteries generally concentrated between 0.95 and 1, and 90.2% of normal arterial blocks had μ_s values between 15 and 36 mm^{-1} (Figures 6 and 7). On the other hand, μ_s and g values from atherosclerotic lesions displayed substantially larger variations than normal arteries, a finding which is consistent with the inherently more heterogeneous nature of tissue pathophysiological responses as compared with the relative homogeneity of healthy tissue organization.

Comparison with histology

To address the potential explanations for the variations of μ_s and g for atherosclerotic lesions compared to normal arteries, histological sections were carefully examined and correlated with the OCT data. As expected, most plaques were characterized by considerable lipid-pools, a fibrous cap, extension of the atheroma into the deeper layers of the vessel wall (i.e., with interspersed collagen and lipid deposits), and disorganized collagen fibers (see Figure 4). All these histological features are likely to contribute to variations of μ_s and g . Indeed, the corresponding OCT images generally displayed signal-poor regions and thus had lower scattering coefficients. An example of such scattering property variation was typified by a block with a very high μ_s of 66.76 mm^{-1} , which was actually found to be representative the fibrous cap surrounding a lipid-rich lesion. In clinical practice, delineation of the highly backscattering fibrotic cap from the modestly backscattering lipid pool may be of great significance, since lesions with thin fibrous caps are considered to be vulnerable and rupture-prone, i.e., likely to trigger an AMI or other unstable coronary syndromes. To accomplish this, we are currently developing more computer-based image processing algorithms.

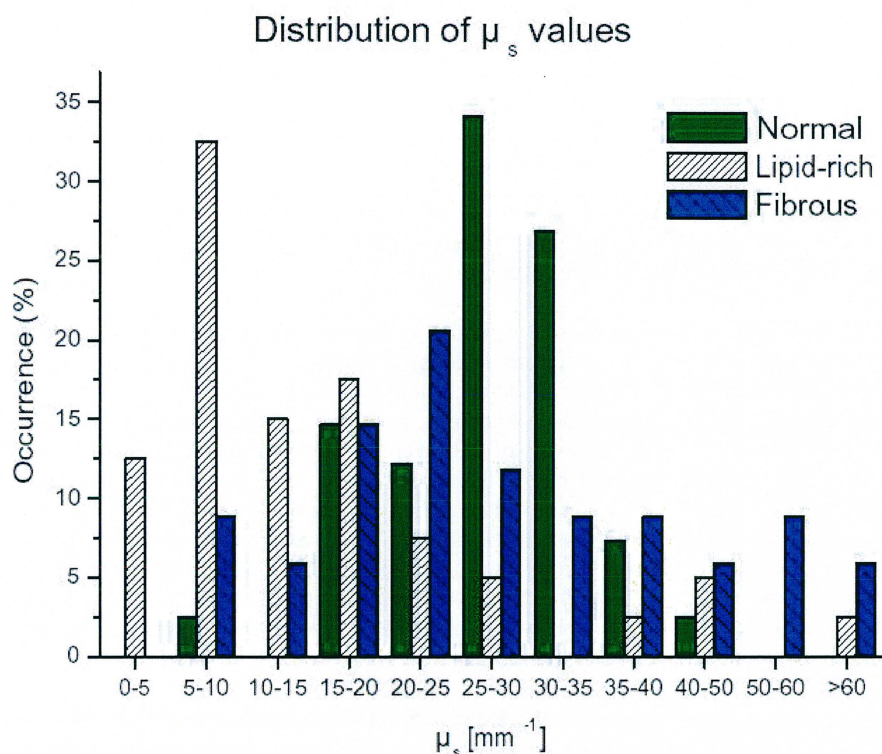


Figure 6: Distribution of arterial blocks according to their scattering coefficient, μ_s .

Of the three vascular tissue types we examined (i.e., normal vessels, lipid-rich lesions, or fibrous lesions), the most diverse optical scattering properties were found in fibrous lesions. A more accurate histopathological classification of this type of lesion could be ‘fibroatheromatous’,⁹ since it always contained isolated areas of fibrous and lipid-rich tissue, as well as mixed fibrous-lipid-rich regions. More specifically, these lesions usually displayed a fibrous cap, and regions with dispersed small lipid pools, a collagen-lipid mixture, and an elastin-lipid-collagen mixture, as shown in Figure 5. Each of these tissue components has different scattering properties, and they were difficult to directly identify in the OCT images. However, a comparison of these quantitative results with the qualitative ones (own results and refs. 3 and 4), clearly demonstrated that fibrous plaque components were more highly backscattering than normal intimal tissue (i.e., 29.4% had $\mu_s > 35$ mm⁻¹, as opposed to 9.8% of normal arteries and lipid-rich lesions).

Statistical Delineation between normal intima and atherosclerotic lesions

Finally, we used our findings of the scattering properties of vessels to define cutoffs for a criteria of μ_s and g for normal intimas, in order to allow for delineation between normal arterial tissue and atherosclerotic lesions. The exact cutoff values were determined by a computer, and we evaluated the cutoffs for the criteria by comparing the resulting sensitivity and specificity. Because we are defining a “normal” criteria, the current standard definitions of sensitivity (the conditional probability of a positive test result given that the disease is present)¹⁰ and specificity (the conditional probability of a negative test result when the disease is not present)¹⁰ are rather ambiguous in this case. Thus, these two terms would need to be redefined in order to be applicable here. We have chosen to redefine sensitivity as the conditional probability of a positive test result given the artery is *healthy*, and specificity as the conditional probability of a negative test result given the artery is *diseased*, i.e. atherosclerotic.

According to this computer-based analysis, we propose $15 < \mu_s < 39$ mm⁻¹ and $0.917 < g < 1$ as tentative cutoff values for normal arteries. As indicated in the Table, these preliminary criteria allow for distinguishing a normal intima from an atherosclerotic one with a sensitivity of 92.7%. Additionally, the criteria accurately distinguish lipid-rich plaques from a normal intima (95% specificity), but the scattering properties of fibrous plaques had some overlap with those of normal vessels, which is reflected by the lower fibrous specificity (67.6%). The overall efficiency, i.e. the probability of correct classification, of these criteria was 85.2%.

Distribution of g values

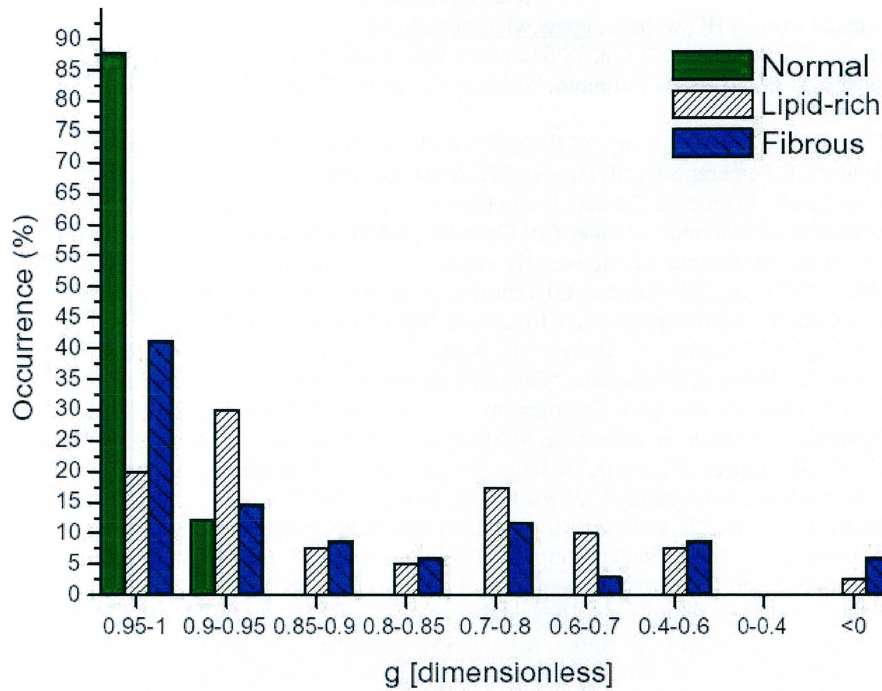


Figure 7: Distribution of arterial blocks according to their anisotropy parameter, g.

Overall sensitivity	92.7
Overall specificity	82.4
Lipid-rich specificity	95.0
Fibrous specificity	67.6
Overall efficiency	85.2

Table: Sensitivity, specificity, and efficiency of the stipulated “normal” criteria of $15 < \mu_s < 39 \text{ mm}^{-1}$ and $0.917 < g < 1$. Values are percents.

While extracting optical properties from OCT images still needs further development before it is of any clinical utility, this investigation took an important first step in tentatively defining what is “normal”. Importantly, the suggested criteria were derived from a limited number of arterial samples and they should be verified in larger studies. The present criteria is based solely on optical scattering properties; by including additional parameters, i.e. intimal thickness, in the criteria, it could be greatly improved. Furthermore, quantitative information on arterial scattering properties as obtained in the current study should be integrated with the qualitative visual information provided by OCT, and it is likely that such a combination of quantitative and qualitative information found in OCT images will substantially enhance the capability of OCT to distinguish between normal arterial tissue and different plaque types.

5. CONCLUSION

The scattering coefficient μ_s and anisotropy factor g differ for healthy, lipid-rich, and fibrous vessels. In the current study, we have showed that by fitting a theoretical model to an averaged OCT depth scan from arterial intima, it is possible to extract scattering parameters and hence assess optical properties relating to the histological organization of this vascular layer. Moreover, we have established a preliminary set of criteria, by which it is possible to distinguish normal intimal tissue from an atherosclerotic lesion by OCT. We conclude, that OCT is a promising imaging modality for identification of different types of arterosclerotic lesions and may hereby provide new important information on vascular pathology.

ACKNOWLEDGEMENT

The authors would like to thank financial support by the Danish Technical Research Council, grant number 9901433, and the BIOP graduate school.

REFERENCES

1. Data taken from WHO website, www.who.int/ncd/cvd
2. D Huang, EA Swanson, CP Lin, JS Schuman, WG Stinson, W Change, MR Hee, T Flotte, K Gregory, CA Puliafito, JG Fujimoto, "Optical Coherence Tomography", *Science* **254**, pp.1178-1181, 1991.
3. IK Jang, BE Bouma, DH Kang, SJ Park, SW Park, KB Seung, KB Choi, M Shishkov, K Schlendorf, E Pomerantsev, SL Houser, HT Aretz, GJ Tearney, "Visualization of Coronary Atherosclerotic Plaques in Patients Using Optical Coherence Tomography: Comparison with Intravascular Ultrasound". *J Amer Col Card* **39**, pp.604-609, 2002.
4. H Yabushita, BE Bouma, SL Houser, HT Aretz, IK Jang, KH Schlendorf, CR Kauffman, M Shishkov, DH Kang, EF Halpern, GJ Tearney, "Characterization of Human Atherosclerosis by Optical Coherence Tomography". *Circulation* **106**, pp.1640-1645, 2002.
5. GJ Tearney, H Yabushita, SL Houser, HT Aretz, IK Jang, KH Schlendorf, CR Kauffman, M Shishkov, EF Halpern, BE Bouma, "Quantification of Macrophage Content in Atherosclerotic Plaques by Optical Coherence Tomography". *Circulation* **107**, pp. 113-119, 2003.
6. BE Bouma, GJ Teaney, H Yabushita, M Shishkov, CR Kauffman, D DeJoseph Gauthier, BD MacNeill, SL Houser, HT Aretz, IK Jang, "Evaluation of intracoronary stenting by intravascular optical coherence tomography". *Heart* **89**, pp. 317-321, 2003.
7. L Thrane, HT Yura, PE Andersen, "Analysis of optical coherence tomography systems based on the extended Huygens-Fresnel principle". *J Opt Soc Am A*. **17**, pp. 484-490, 2000.
8. RF Lutomirski and HT Yura, "Propagation of a finite optical beam in an inhomogeneous medium". *Appl Opt* **10**, pp.1652-1658, 1971.
9. R Virmani, FD Kolodgie, AP Burke, A Farb, SM Schwartz, "Lessons From Sudden Coronary Death- A Comprehensive Morphological Classification Scheme for Atherosclerotic Lesions". *Arterioscler Thromb Vasc Biol* **20**, pp. 1262-1275, 2000.
10. M Greiner and IA Gardner, "Epidemiologic issues in the validation of veterinary diagnostic tests". *Prev Veter Med* **45**, pp. 3-22.

Paper II

Determination of optical scattering properties of highly-scattering media in optical coherence tomography images

David Levitz, Lars Thrane, Michael H. Frosz, and Peter E. Andersen

Optics and Fluid Dynamics Department, Risø National Laboratory, P.O. Box 49, DK-4000 Roskilde, Denmark
david.levitz@risoe.dk, lars.thrane@risoe.dk, michael.h.frosz@risoe.dk, peter.andersen@risoe.dk

Claus B. Andersen

Department of Pathology, Rigshospitalet, Telium Bygning, Frederick V's Vej, DK-2100 København Ø, Denmark
clausbrh01871andersen@rh.dk

Jurga Valanciunaite, Johannes Swartling, and Stefan Andersson-Engels

Department of Physics, Lund Institute of Technology, P.O. Box 118, SE-221 00 Lund, Sweden
jurgaval@centras.lt, johannes.swartling@polimi.it, stefan.andersson-engels@fysik.lth.se

Peter R. Hansen

Department of Cardiology, Amtssygehuset i Gentofte, Niels Andersenvej 65, DK-2900 Hellerup, Denmark
peha@gentoftehosp.kbhamt.dk

Abstract: We developed a new algorithm that fits optical coherence tomography (OCT) signals as a function of depth to a general theoretical OCT model which takes into account multiple scattering effects. With use of this algorithm, it was possible to extract both the scattering coefficient and anisotropy factor from a particular region of interest in an OCT image. The extraction algorithm was evaluated against measurements from an integrating sphere on a set of tissue phantoms and yielded valid results. Finally, a preliminary *ex vivo* OCT investigation on human aortic specimen indicated that the algorithm may contribute importantly to differentiation between normal and atherosclerotic arteries. We conclude that this algorithm may facilitate tissue characterization by OCT.

©2003 Optical Society of America

OCIS codes: (170.4500) optical coherence tomography, (290.0290) scattering, (170.4580) optical diagnostics for medicine

References and Links

1. C. F. Bohren and D. R. Huffman, *Absorption and scattering of light by small particles* (John Wiley & Sons, Inc., New York, NY 1983).
2. Z. Fayad and V. Fuster, "Clinical imaging of the high-risk or vulnerable atherosclerotic plaque," *Circ. Res.* **89**, 305-316 (2001).
3. J. C. Kennedy, R. H. Pottier, and D. C. Pross, "Photodynamic therapy with endogenous protoporphyrin IX: Basic principles and present clinical experience," *J. Photochem. Photobiol. B* **6**, 143-148 (1990).
4. D. Huang, E. A. Swanson, C. P. Lin, J. S. Schuman, W. G. Stinson, W. Chang, M. R. Hee, T. Flotte, K. Gregory, C. A. Puliafito, and J. G. Fujimoto, "Optical coherence tomography," *Science* **254**, 1178-1181 (1991).
5. B. Povazay, K. Bizheva, A. Unterhuber, B. Hermann, H. Sattmann, A. F. Fercher, W. Drexler, A. Apolonski, W. J. Wadsworth, J. C. Knight, P. S. J. Russel, M. Vetterlein, and E. Scherzer, "Submicrometer axial resolution optical coherence tomography," *Opt. Lett.* **27**, 1800-1802 (2002).
6. G. J. Tearney, S. A. Boppart, B. Bouma, M. E. Brezinski, N. J. Weissman, J. F. Southern, and J. G. Fujimoto, "Scanning single-mode fiber optic catheter-endoscope for optical coherence tomography," *Opt. Lett.* **21**, 543-545 (1996).
7. J. M. Schmitt, A. Knüttel, M. Yablowsky, and M. A. Eckhaus, "Optical-coherence tomography of a dense tissue: statistics of attenuation and backscattering," *Phys. Med. Biol.* **39**, 1705-1720 (1994).
8. N. M. Shakhova, V. M. Gelikonov, V. A. Kamensky, R. V. Kuranov, and E. V. Turchin, "Clinical aspects of the endoscopic optical coherence tomography: a methods for improving the diagnostics efficiency," *Laser Physics* **12**, 23-32 (2002).
9. D. Levitz, C. B. Andersen, M. H. Frosz, L. Thrane, P. R. Hansen, T. M. Jørgensen, and P. E. Andersen "Assessing blood vessel abnormality via extracting scattering properties from OCT images" in *European Conference in Biomedical Optics (ECBO)*, W. Drexler, ed. Proc. SPIE **5140**, 12-19 (2003).
10. R. O. Esenaliev, K. V. Larin, I. V. Larina, and M. Motamedi, "Noninvasive monitoring of glucose concentration with optical coherence tomography," *Opt. Lett.* **26**, 992-994 (2001).
11. L. Thrane, H. T. Yura, and P. E. Andersen, "Analysis of optical coherence tomography systems based on the extended Huygens-Fresnel principle," *J. Opt. Soc. Am. A* **17**, 484-490 (2000).
12. G. J. Tearney, B. Bouma, and J. G. Fujimoto, "High-speed phase- and group-delay scanning with a grating-based phase control delay line," *Opt. Lett.* **22**, 1811-1813 (1997).
13. A. M. Rollins and J. A. Izatt, "Optimal interferometer designs for optical coherence tomography," *Opt. Lett.* **24**, 1484-1486 (1999).

14. R. F. Lutomirski and H. T. Yura, "Propagation of a finite optical beam in an inhomogeneous medium," *Appl. Opt.* **10**, 1652-1658 (1971).
15. A. E. Siegman, *Lasers* (University Science Books, Mill Valley, CA 1986).
16. H. T. Yura, L. Thrane, and P. E. Andersen, "Closed form solution for the Wigner phase-space distribution function for diffuse reflection and small angle scattering in a random medium," *J. Opt. Soc. Am. A* **17**, 2464-2474 (2000).
17. C. C. Cheng and M. G. Raymer, "Propagation of transverse optical coherence in random multiple-scattering media," *Phys. Rev. A* **62**, 1-12 (2000).
18. S. A. Prahl, Inverse Adding-Doubling Software. 1999. <http://omlc.ogi.edu/software/iad/index.html>
19. J. Swartling, J. S. Dam, and S. Andersson-Engels, "Comparison of spatially and temporally resolved diffuse-reflectance measurement systems for determination of biomedical optical properties," *Appl. Opt.* **42**, 4612-4620 (2003).
20. D. D. Royston, R. S. Poston, and S. A. Prahl, "Optical properties of scattering and absorbing materials used in the development of optical phantoms at 1064 nm," *J. Biomed. Opt.* **1**, 110-116 (1997).
21. I. K. Jang, B. E. Bouma, D. H. Kang, S. J. Park, S. W. Park, K. B. Seung, K. B. Choi, M. Shishkov, K. H. Schlendorf, E. Pomerantsev, S. L. Houser, H. T. Aretz, and G. J. Tearney, "Visualization of coronary atherosclerotic plaques in patients using optical coherence tomography: comparison with intravascular ultrasound," *J Am Coll Cardiol* **39**, 604-609 (2002).
22. H. Yabushita, B. E. Bouma, S. L. Houser, H. T. Aretz, I. K. Jang, K. H. Schlendorf, C. R. Kauffman, M. Shishkov, D. H. Kang, E. F. Halpern, and G. J. Tearney, "Characterization of human atherosclerosis by optical coherence tomography," *Circulation* **106**, 1640-1645 (2002).
23. G. J. Tearney, H. Yabushita, S. L. Houser, H. T. Aretz, I. K. Jang, K. H. Schlendorf, C. R. Kauffman, M. Shishkov, E. F. Halpern, and B. E. Bouma, "Quantification of macrophage content in atherosclerotic plaques by optical coherence tomography," *Circulation* **107**, 113-119 (2003).
24. B. E. Bouma, G. J. Tearney, H. Yabushita, M. Shishkov, C. R. Kauffman, D. DeJoseph Gauthier, B. D. MacNeill, S. L. Houser, H. T. Aretz, E. F. Halpern, and I. K. Jang, "Evaluation of intracoronary stenting by intravascular optical coherence tomography," *Heart* **89**, 317-321 (2003).

1. Introduction

Over the last few decades there has been a continuing search for a high-resolution imaging modality that can quickly and accurately measure the optical properties of layered tissue *in vivo*. Here, the optical properties of interest are those that primarily guide light transport inside the tissue, namely, the scattering coefficient μ_s and anisotropy factor g [1]. A valid method with which these measurements can be done have many important biomedical implications, such as identifying vulnerable atheromatous lesions during percutaneous coronary interventions [2] or distinguishing a tumor from the surrounding healthy tissue for photodynamic treatment [3].

Optical coherence tomography (OCT) is an imaging technology measuring the backscattering properties of tissues [4]. In OCT, the light reflected off a sample is interfered with a reference wave utilizing a technique known as low-coherence interferometry. An interference signal can only arise when the optical pathlength difference between the two arms of a Michelson interferometer is within the coherence length of the source. Thus, the axial resolution in OCT is proportional to the temporal coherence length of the source, and with a broadband source it is possible to obtain a resolution as high as 0.5 μm in tissue [5]. As a fiber-based technology, OCT can be readily integrated into many catheter-based endoscopic applications [6].

OCT signals are mainly influenced by the scattering properties of the examined sample, i.e., μ_s and g . These are macroscopic physical properties unique to the tissue, which play a vital role in the modeling of OCT signals. By properly modeling an OCT signal as a function of depth so that multiple scattering events are included, and fitting the depth profile of coherent backscattered light in an OCT image (also called depth-scan or A-scan) to such model, it is possible to extract out both μ_s and g . Preliminary clinical investigations [7-10] indicated that additional diagnostic information based on the optical properties could be extracted from OCT images, although the model in Refs. [7,10] considered the single-scattering case only, where only one parameter can be extracted. Ref. [7] describes the basic steps necessary to include multiple-scattering effects in the modeling, which would result in fitting two parameters instead of one, as in Refs. [8,9]. Still, the model used in Ref. [8] is restricted in its ability to handle complex geometries, which is an inherent advantage of the model used for this study [11]. Additionally, OCT has the important advantage that images can be obtained *in vivo* from which optical properties may be extracted thereby enabling *in situ* assessment of the tissue and/or lesion. This feature, if successfully implemented, holds considerable promise for future clinical utility.

Our objectives in this study were twofold: firstly, to demonstrate that the curve fitting algorithm we employed, which is based on a general theoretical analysis taking into account multiple scattering effects [11], compared well with controlled experimental measurements and theoretical calculations. This evaluation part of the study was conducted on a set of tissue phantoms using integrating sphere measurements to determine optical scattering properties. Secondly, we applied the OCT extraction method on normal and atherosclerotic human aortic samples in a preliminary *ex vivo* study in order to demonstrate that the technique may provide a basis for distinguishing between different tissues by their optical properties.

In the present paper, we first demonstrate how our curve-fitting algorithm can integrate an established theoretical model that includes multiple-scattering effects in the OCT signal [11] with OCT images and hereby quantify the scattering properties of the imaged sample. Next, we show that this technique can accurately determine these parameters by means of the evaluation study. Finally, we present a preliminary *ex vivo* analysis of normal and atherosclerotic human arteries as an example illustrating how this technique may be applied.

2. OCT

2.1 OCT system and measurements

The OCT system used for this study (Fig. 1) employed a broadband source with a center wavelength of 1300 nm (AFC, Inc., model BBS 1310), providing a subsequent axial resolution of ~ 10 μm in tissue. The sample arm unit consisted of a handheld probe that the user holds in contact with the sample. A computer controlled transverse scanning module and an integrated digital video camera were incorporated into the probe unit. The digital video camera was used to visually assist transverse scanning. In the reference arm, fast scanning was achieved with use of a Fourier domain rapid-scanning optical delay line [12]. An InGaAs (New Focus, Inc., model 2017) detector measured the interference pattern between the two arms of the interferometer. During the first part of the study, an optical circulator between the source and the 50/50 beam splitter was included in the setup, which was also connected to a second detector to allow for dual balanced detection that increased signal-to-noise ratio (SNR) [13]. The electronic signal emerging from the detector was amplified and high-pass filtered. Detection of the interferometric envelope was implemented in hardware using a programmable logic device. Thereafter, the signal was digitized and stored on a computer.

The OCT system was used to capture depth interferometric information from the investigated samples resulting in images with 690 axial (z) pixels (4.16 μm spacing) and 400

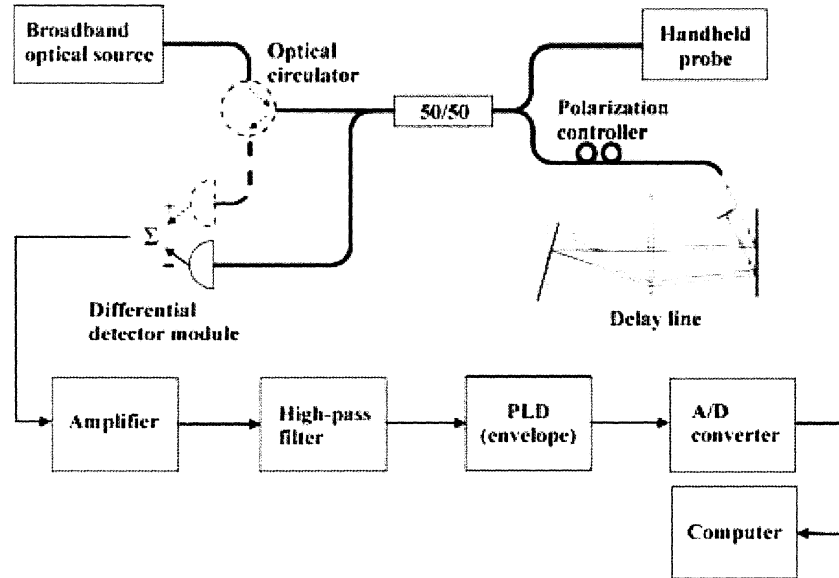


Fig. 1: The OCT system. The optical circulator and a second detector (dashed line) were only used in the first part of the study. PLD: programmable logic device.

transverse (x) pixels (10 μm spacing). In all the images, light was focused on the surface of the scattering medium. Corresponding digital photographs of the sample and the scanned region were automatically taken along with every OCT image. Image acquisition time from start of scanning was 5-6 seconds. The dynamic range of the system was >100 dB.

2.2 OCT Model

A model that analyzes the heterodyne OCT signal as a function of depth has been developed by Thrane et al [11]. Based on the extended Huygens-Fresnel principle [14], this model takes into account multiple scattering effects, and thus the depth profile of the OCT signal is a function of both μ_s and g as well as other parameters. This model is general and capable of handling different sample arm geometries, i.e., dynamic vs. fixed focusing. Furthermore, it is based on ABCD matrix formalism [15], and may therefore easily be applied to a multiple-layered geometry of scattering media, such as is frequently the case with tissue.

As detailed in Ref. [11], the mean square of the heterodyne signal current $\langle i^2(z) \rangle$ at probing depth z measured by an OCT system is a product of two factors, i.e., $\langle i^2(z) \rangle = \langle i^2 \rangle_0 \Psi(z)$. Here $\langle i^2 \rangle_0$ is the mean square heterodyne signal current in the absence of scattering and $\Psi(z)$ is the heterodyne efficiency factor describing the signal degradation due to the scattering. The factor $\langle i^2 \rangle_0$ is defined as $\langle i^2 \rangle_0 = \alpha^2 P_R P_S \sigma_b / \pi w_H^2$ with α being the power to current conversion factor, P_R and P_S the power of the reference and input sample arm beams, σ_b the effective backscattering cross-section, and w_H the 1/e irradiance radius at the probing depth in the absence of scattering, respectively. More precisely, w_H is defined as [11]:

$$w_H^2 = w_0^2 \left(A - \frac{B}{f} \right)^2 + \left(\frac{B}{k w_0} \right)^2, \quad (1)$$

where A and B are elements from the ABCD ray-matrix for light propagation from the lens plane to the probing depth in the sample. For the case where the focal plane of the sample beam is fixed on the surface of the sample, $A=1$ and $B=f+z/n$. The quantity w_0 represents the 1/e irradiance radius of the input sample beam at the lens plane, $k=2\pi/\lambda$ where λ is the center wavelength of the source, f is the focal length of the lens, and n is the mean index of refraction of the sample.

The factor of interest in the above equation for $\langle i^2(z) \rangle$ is the heterodyne efficiency factor $\Psi(z)$, which contains the scattering effects. Specifically, it has been shown [11] that

$$\Psi(z) = \exp(-2\mu_s z) + \frac{4 \exp(-\mu_s z) [1 - \exp(-\mu_s z)]}{1 + w_s^2 / w_H^2} + [1 - \exp(-\mu_s z)]^2 \frac{w_H^2}{w_s^2}. \quad (2)$$

The first term in Eq. (2) represents the single scattering contribution, the third term represents the contribution from multiple scattering events, while the second term is the cross-term. Also, w_s is the 1/e irradiance radius at the probing depth in the presence of scattering [11], that is,

$$w_s^2 = w_0^2 \left(A - \frac{B}{f} \right)^2 + \left(\frac{B}{k w_0} \right)^2 + \left(\frac{2B}{k \rho_0(z)} \right)^2, \quad (3)$$

with $\rho_0(z)$ being the lateral coherence length. A derivation of $\rho_0(z)$ [11,16] shows that

$$\rho_0(z) = \sqrt{\frac{3}{\mu_s z} \frac{\lambda}{\pi \theta_{rms}} \left(\frac{nB}{z} \right)}, \quad (4)$$

where θ_{rms} represents the root-mean-square scattering angle, defined as the half-width at e^{-1} maximum of a Gaussian curve fit to the main frontal lobe of the scattering phase function [17]. As multiple-scattering effects play an important role in the OCT signal in this model [11], a second parameter, θ_{rms} , may also be fitted. The above four equations constitute the model used in our fitting algorithm. It should be pointed out that the calculation of the OCT signal was carried out from closed-form expressions, which is another major advantage of the new algorithm: the measured depth-profile may be fitted to a closed-form expression, thereby reducing computational burden.

Of note, the anisotropy factor g in the model used in this investigation is defined slightly differently than the mean value of the cosine of the deflection angle ($g = \langle \cos \theta \rangle$) [1]. Instead, the model [11] uses the effective anisotropy factor, $g_{eff} = \cos \theta_{rms}$. Typically, $g_{eff} \geq g$. As a result of this, the g value obtained from experimental measurements with the integrating sphere cannot be directly compared to the g_{eff} extracted from OCT images. Instead, the extracted g_{eff} was compared to $\cos \theta_{rms}$ as derived from a Mie calculation of the scattering phase function [1].

2.3 Extraction algorithm

We have developed an algorithm based on Eqs. (1-4) consisting of a set of Matlab codes for the purpose of these analyses. The principles of how optical scattering properties are evaluated from a given image are illustrated in Fig. 2. Fig. 2(A) shows a detailed geometry of the sample arm unit during measurements, and Fig. 2(B) presents a typical raw OCT image of a tissue phantom. First, the user selected a transverse region of interest (ROI, orange dashed inset in Fig. 2(B)) from a given image, consisting of several adjacent depth-scans. These adjacent A-scans were averaged along the lateral direction and linear smoothing was applied using a 5-pixel kernel. This yielded a smoothed, averaged curve with a high SNR that is given in Fig. 2(C). The number of longitudinal pixels to which the model would be fit to was chosen from this curve (magenta dashed inset in Fig. 2(C)). Pixels near the interface between the scattering and non-scattering media (immediately to the left of the inset in Fig. 2(C)) representing a specular reflection were excluded from the fit. At this point, initial value guesses for μ_s and θ_{rms} were entered by the user. Finally, Fig. 2(D) shows a comparison of data points fit to

$\sqrt{\langle i^2(z) \rangle}$, returned along with the scattering coefficient μ_s , the root-mean-square scattering angle, θ_{rms} ($g_{eff} = \cos \theta_{rms}$), and error estimates.

Of note, the mean square heterodyne signal current $\langle i^2 \rangle_0$, which is proportional to the effective back-scattering cross section σ_b , is also fitted in our algorithm. Assuming an absolute measurement of the OCT signal, σ_b could be extracted. This is, however, often cumbersome in practice. As μ_s and g are representatives of the shape of the OCT signal as a function of depth, these two parameters adequately describe the tissue. Also noteworthy is that the scattering cross-section and the effective back-scattering cross-section are linked through $\sigma_b = \sigma_s(180^\circ)$ and the cross-sections are related to their corresponding coefficients through the density of scattering particles [1]. Finally, we have chosen to fit μ_s instead of μ_b since these values are readily available in the literature for many different tissues.

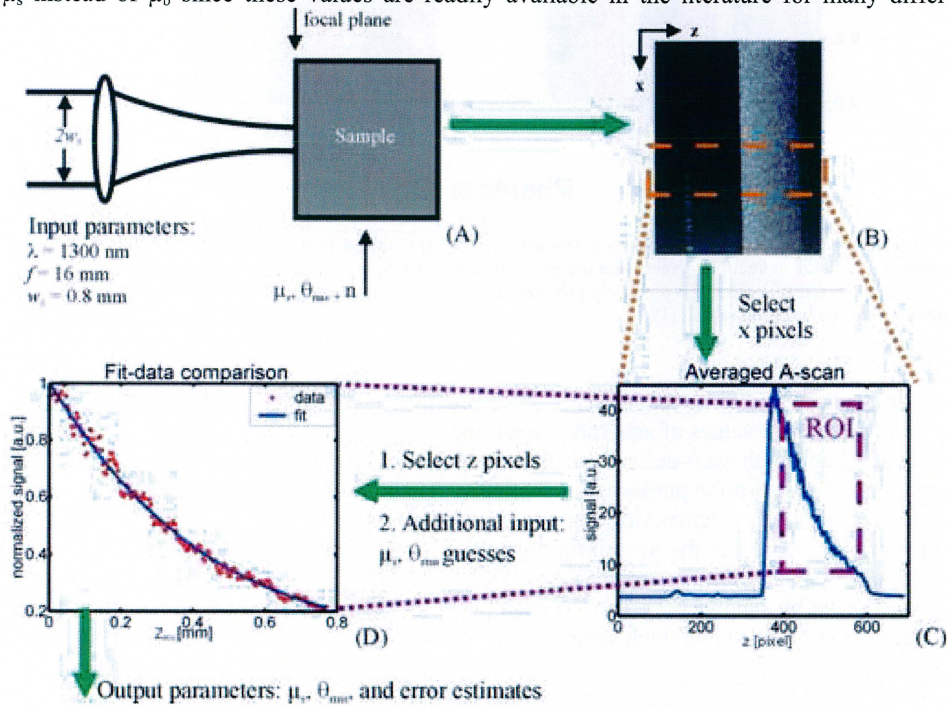


Fig. 2: A schematic representation of the principles of the extraction algorithm. The sample arm geometry and input parameter values from our OCT setup are shown in (A). These parameters were used to generate an image (B) and were also employed during curve fitting (C-D). A transverse ROI was selected in (B, inset), averaged, smoothed, and plotted in (C). The axial pixels of the ROI were chosen in (C, inset), and shown as points in (D). z_{ROI} represents the probing depth within the region of interest in (D). The fit was performed on the resulting data-points using μ_s and θ_{rms} initial value guesses as additional input. The algorithm returned μ_s , θ_{rms} , the fit's error estimates, and a plot comparing the fit to the data points (D).

3. Evaluation study

In order to establish the reliability of our new algorithm for extracting optical properties of highly scattering media, experiments on tissue phantoms with well-controlled optical properties were carried out. Specifically, this verification involved several phantoms with different scattering properties measured with a well-established method for obtaining optical properties from such samples, i.e., the integrating sphere method and inverse adding-doubling (IAD) [18]. To adequately compare the extracted g_{eff} values, the scattering phase function of 1300 nm light in those phantoms was calculated using basic principles from Mie theory [1].

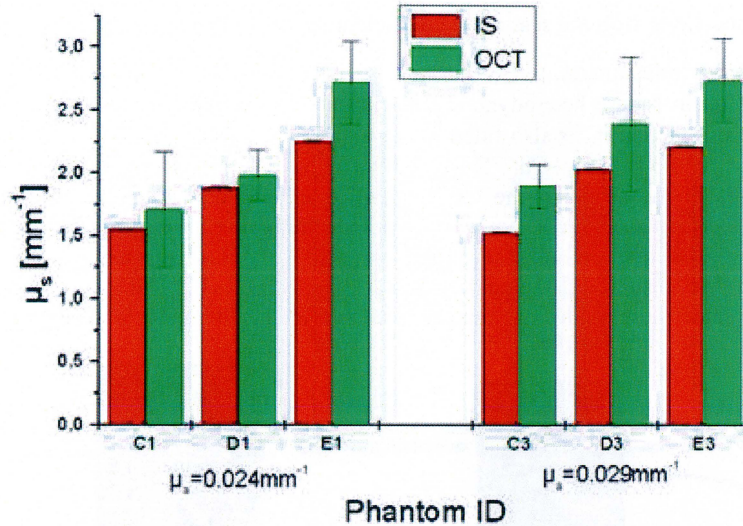


Fig. 3: A comparison of μ_s values (means \pm standard deviation) obtained from measurements on tissue phantoms with OCT extractions (green) and the integrating sphere (IS, in red). Note a step wise increase on two separate sets of 3 phantoms purposely prepared to exhibit such an increase. Details about phantom nomenclature can be found in Ref. [19].

3.1 Phantoms

For these experiments, we used six phantoms from a previous investigation [19] with three distinct values of μ_s and two distinct values of absorption coefficient μ_a , respectively. The phantoms consisted of epoxy resin ($n=1.55$) with well-defined quantities of scattering material and absorbing pigment added for scattering and absorption purposes, respectively. Titanium IV Oxide (TiO_2 , $n=2.55$) powder, with a particle size of $1 \mu\text{m}$ (Sigma-Aldrich) was used as a scattering material and toner from the photocopying machine served as the absorbing pigment. In all phantoms used, it was ensured that absorption effects were negligible compared to those from scattering. Mounting the phantoms in a slab geometry was achieved by sandwiching 1 ml of each phantom between two microscope slides before the epoxy hardened yielding 1.0 mm thick samples with a cross section measuring $3 \times 3 \text{ cm}^2$ [19].

3.2 Integrating sphere measurements

Our measurements of the diffuse reflectance and transmittance were performed using an integrating sphere (Labsphere model RT-060-SF) with the broadband source (AFC) operating at a center wavelength of 1300 nm also used for OCT imaging. Light was guided to the sphere using a single-mode optical fiber and collected by an IR detector supplied by the sphere manufacturer. The beam arriving at the transmission port was 2.3 mm in diameter, with a port diameter of 25.4 mm. A chopper rotating at 730 Hz modulated the beam, and was synchronized with a lock-in amplifier on the detector side to increase SNR. Both diffuse reflectance and diffuse transmittance measurements were done three times each with sample orientation randomized. Our integrating sphere data was processed in version 1 of the inverse adding-doubling (IAD) code [18] using four fluxes per iteration.

3.3 Fitting routine

Each phantom was imaged twice. Based on experience, the true scattering parameters of a phantom are most accurately and reliably determined by performing multiple fits with different sets of input parameters (Fig. 2(C-D)) in each. Specifically, ROIs from different areas of the image need to be evaluated using various sets of initial value guesses for μ_s and θ_{rms} for each ROI. Also, the number of z pixels in an ROI should be maximized and kept constant. As a consequence of this, the OCT data was evaluated in the following manner: In every image there were five ROIs with fifteen curve fitting attempts per ROI. Curve fitting attempts in a single ROI only differed by the combinations of μ_s and θ_{rms} guesses used. A random number generator determined the transverse boundary pixels for each ROI. The fitted length was chosen to be 0.77 mm (186 pixels), the maximum that could be used in all the images accounting for phantoms imaged at a small angle. Phantoms whose optical depth (i.e., $\mu_s \times$ scattering layer thickness) did not exceed 1.3 as determined with the integrating sphere and thus did not definitively enter the multiple-scattering regime were excluded.

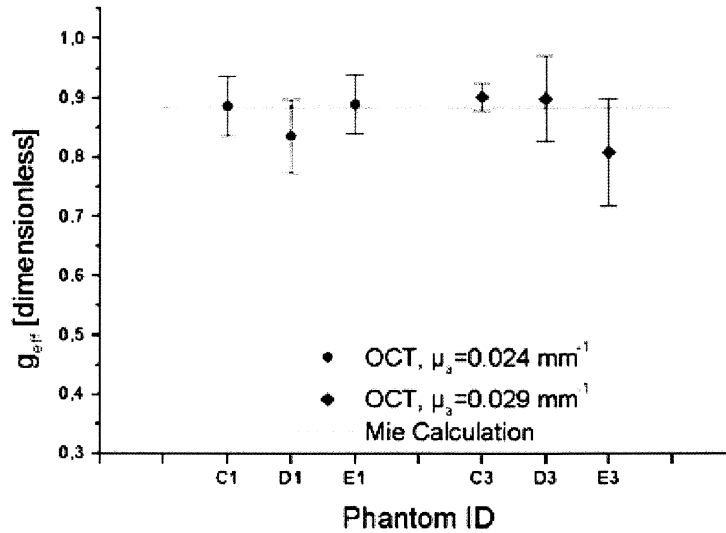


Fig. 4: A comparison of g_{eff} value (means \pm standard deviations) from OCT extractions (points) and the Mie calculation (line). Overlap in results is seen for every phantom. Details regarding phantom nomenclature can be found in Ref. [19].

3.4 Results and Discussion

A graphical comparison of μ_s obtained from OCT extractions and from the IAD code is shown in Fig. 3. Error bars representing the standard deviation on the measurements are not readily visible on the sphere data since the standard deviation did not exceed 0.25% of the mean. A Mie calculation using the code from Bohren & Huffman for homogeneously shaped spherical particles [1] was performed to obtain a theoretical $g_{\text{eff}}=0.885$. A comparison of g_{eff} derived from OCT extractions to the theoretical result is shown in Fig. 4.

As shown in Figs. 3 and 4, the extraction algorithm generated consistent and reliable results for the tissue phantoms investigated. Every value of g_{eff} extracted overlapped with the 0.885 obtained from the Mie calculation within the error bars (Fig. 4). Moreover, a step-wise increase in μ_s was clearly observed with two different phantom sets (3 phantoms/set) using *both* techniques. While the error bars in three of six phantoms overlapped with the value returned from the IAD algorithm, the difference in the remaining three did not exceed 13% of the IAD returned value. One can notice, however, that the OCT-technique seems to slightly overestimate the scattering coefficient for these particular samples.

In examining the potential sources of error in the OCT extractions, the following should be considered: The integrating sphere measures optical properties of scattering media on a macroscopic scale as an average throughout the sample, while optical property extractions from an OCT image involves averaging over a much smaller region. Thus, inevitable phantom inhomogeneities on a μm scale could have affected our results. Also, IAD does not take wavelength as one of its inputs [18], or in other words, is designed for monochromatic light where samples exhibit uniform optical properties. The source used in this experiment had a 3 dB bandwidth of 60 nm, which could have an influence on the experiments and thus the returned IAD data. Furthermore, phantom albedos (~ 0.97) were slightly outside the recommended range of 0.4-0.95 for achieving the highest accuracy with the IAD algorithm [20], and this too could have slightly offset the IAD data points.

Considering the fine overall agreement between extracted values using our new algorithm and the IAD algorithm, we conclude that our new algorithm is capable of extracting optical properties with sufficient reliability.

4. Preliminary *ex vivo* study

Recently, OCT has shown promise for imaging of coronary atherosclerotic plaques [21-24]. At present, however, visual differentiation between the general histopathological types of plaques, i.e., fibrous, fibrocalcific, and lipid-rich lesions, in OCT images is inherently qualitative and subjective. Several features of atherosclerotic plaque histopathology, i.e., reorganization and disruption of intimal collagen fibers, are expected to produce marked changes in the tissue optical scattering properties (μ_s and g_{eff}). Thus, to exemplify how our OCT algorithm may provide quantitative information about complex tissue pathology, we performed a preliminary *ex vivo* investigation in human atherosclerotic lesions.

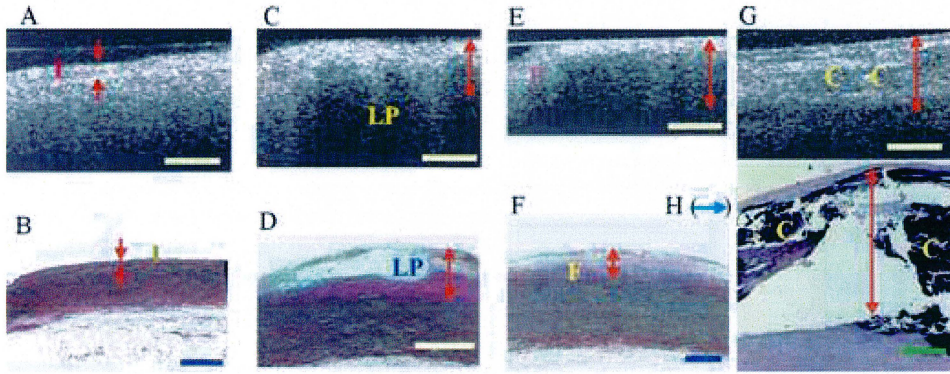
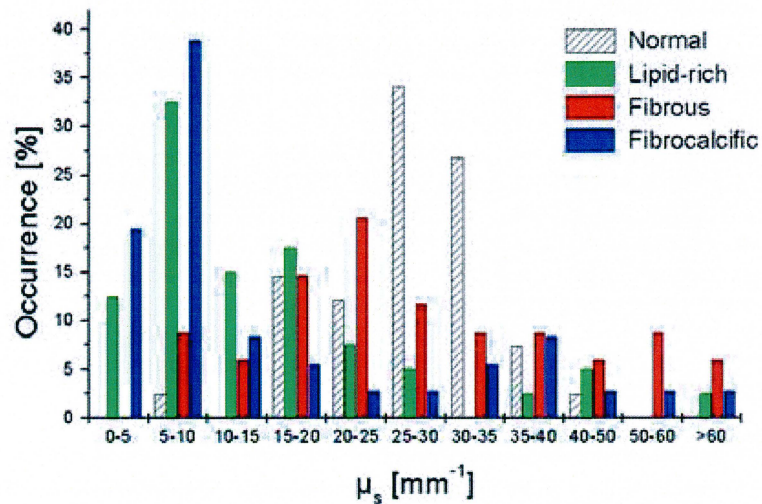


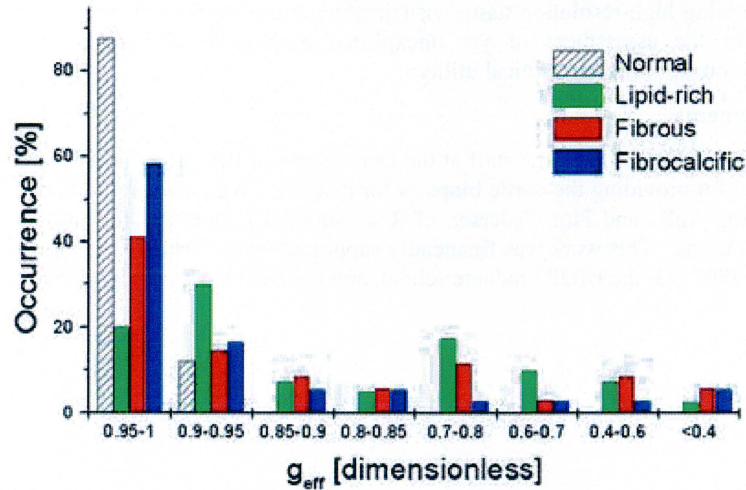
Fig. 5: Correlation of raw OCT images (A, C, E, and G) and histopathology (B, D, F, and H). Normal intima labeled 'I' in (A-B). Lipid-rich lesion (C-D), with a lipid pool marked 'LP'. Fibrous plaque (E-F), with fibrous area marked 'F'. Fibrocalcific lesion (G-H), with the calcifications denoted 'C'. Rupture artifacts caused by the decalcifying process are clearly seen in (H). The arrows represent the intima in (A-F) and the fitting region in (G-H), respectively. Bars=500 μm .

4.1 Curve fitting and imaging

Fourteen (4 normal, 4 lipid-rich, 3 fibrous, and 3 fibrocalcific) aortic segments were obtained within four hours of autopsy and imaged with OCT in phosphate buffered saline. During OCT imaging, the OCT probe was in contact with a glass cuvette inside of which the biopsies were mounted. Regions corresponding to those imaged by OCT were marked and located on digital photos. The samples were routinely paraffin embedded and sliced at the regions defined by the digital photographs. Sections were stained (hematoxylin and eosin or combined elastin and van Gieson Hansen staining) and corresponding areas of the intima were identified in OCT images and histological sections, respectively, using Table 1 in Ref. [21] as a guide. The OCT images were laterally divided into ROIs spanning approximately 20-30 A-scans or 200-300 μm . Altogether, the images were subdivided into 151 ROIs, including 41 normal, 40 lipid-rich, 34 fibrous, and 36 fibrocalcific ROIs, with each ROI being systematically selected for the criterion of the ROI spanning an area with uniform scattering properties. To facilitate interpretation, the extracted data were grouped into intervals based on the respective values of μ_s and g_{eff} . For μ_s , the intervals spanned 5 mm^{-1} for values from 0 to 40 mm^{-1} , and 10 mm^{-1} for values over 40 mm^{-1} . Since human soft tissue is generally very forward scattering, g_{eff} range intervals of 0.05 were chosen for g_{eff} values near 1, but the interval range was larger for the limited number of g_{eff} values below 0.8.



(A)



(B)

Fig. 6: Distributions of μ_s (A) and g_{eff} (B) for normal arteries and lipid-rich, fibrous, and fibrocalcific atherosclerotic plaques, respectively. In (A), μ_s for normal samples (striped) were centered between 15 and 40 mm^{-1} , but were centered at lower values for lipid-rich (green) and fibrocalcific (blue) plaques, and were randomly distributed for fibrous plaques (red). In (B), g_{eff} values were generally higher in normal intimas than in atherosclerotic lesions.

4.2 Initial results

OCT images were correlated with the corresponding histological sections using Table 1 in Ref. [21] as a guide and representative samples are shown in Fig. 5. Qualitatively, images obtained by OCT and microscopy demonstrated similar gross histopathological features that allowed for reasonable differentiation between normal vessels and lipid-rich, fibrous, and fibrocalcific plaques, respectively. The distribution of μ_s and g_{eff} for ROIs of normal arteries and the three overall atherosclerotic lesion types is shown in Fig. 6. Our preliminary data suggested that very similar optical properties were observed in images of normal samples (diagonal lines) but not in those representing atherosclerotic lesions. In normal arteries, almost 90% of g_{eff} values were concentrated between 0.95 and 1, whereas more than 50% of atherosclerotic lesion ROIs were below 0.95. Approximately 95% of the normal arterial samples had μ_s between 15 and 39 mm^{-1} , while μ_s was below 15 mm^{-1} in about 60% of lipid-rich and fibrocalcific plaques. Furthermore, fibrous lesions demonstrated very considerable variations in μ_s .

To our knowledge, the above preliminary data represent the first quantitative analysis of the optical scattering properties, i.e., the scattering coefficient and the anisotropy factor, of the normal and diseased human aortic intima *in vitro* at 1300 nm. The study indicates that the presented algorithm may provide a basis for extension of the OCT technique beyond qualitative image assessment towards tissue characterization based on physical principles. Techniques for detection of unstable atherosclerotic lesions have generated enormous interest in the field of vascular biology, and the future clinical utility of such methods is dependent on minimizing subjective and operator-dependent bias in the acquisition and interpretation of data [2]. We therefore suggest that the current OCT algorithm is an important step in this direction and that further studies are warranted to define the validity of the described method for characterization of atherosclerotic lesions.

5. Conclusion

The current study demonstrated that with use of the outlined algorithm, the optical scattering properties of tissue may be obtained from optical coherence tomography images. The evaluation study on phantoms showed that OCT is capable of accurately determining the optical scattering properties, i.e., the scattering coefficient μ_s and effective anisotropy parameter g_{eff} , of highly scattering media, obtaining results in agreement with a well-established experimental method. Using this technique, we were able for the first time to conduct a preliminary investigation that quantitatively compared the optical scattering properties of the human arterial intima *ex vivo*. Furthermore, our preliminary *ex vivo* tissue data indicated that differences in scattering properties data may exist between normal and atherosclerotic arterial segments and that optical scattering data provided by OCT can potentially

contribute to plaque characterization. The OCT technique presented here opens many new avenues of research combining high-resolution tissue visualization and scattering properties measurements. This may allow for the assessment of yet unexplored biophysical properties of tissues and holds considerable promise for future clinical utility.

Acknowledgements

The authors would like to thank the staff at the Department of Pathology, Rigshospitalet, Denmark, for inviting us and for providing the aortic biopsies for imaging. We also want to thank Andreas Tycho of OCT Innovation ApS., and Finn Pedersen of Risø National Laboratory for helping with the imaging and sample handling. This work was financially supported by the Danish Technical Research Council, grant number 9901433, the BIOP graduate school, and the Danish Heart Foundation.

References

- 1 C. F. Bohren and D. R. Huffman, *Absorption and scattering of light by small particles* (John Wiley & Sons, Inc., New York, NY 1983).
- 2 Z. Fayad and V. Fuster, "Clinical imaging of the high-risk or vulnerable atherosclerotic plaque," *Circ. Res.* **89**, 305-316 (2001).
- 3 J. C. Kennedy, R. H. Pottier, and D. C. Pross, "Photodynamic therapy with endogenous protoporphyrin IX: Basic principles and present clinical experience," *J. Photochem. Photobiol. B* **6**, 143-148 (1990).
- 4 D. Huang, E. A. Swanson, C. P. Lin, J. S. Schuman, W. G. Stinson, W. Chang, M. R. Hee, T. Flotte, K. Gregory, C. A. Puliafito, and J. G. Fujimoto, "Optical coherence tomography," *Science* **254**, 1178-1181 (1991).
- 5 J. A. Zagzebski. *Essentials of ultrasound physics* (Elsevier, New York: 1996).
- 6 K. Takada, I. Yokohoma, K. Chida, and J. Noda, "New measurement system for fault location in optical waveguide devices using an interferometric technique", *Appl Opt* **26**, 1603-1606 (1987).
- 7 B. Povazay, K. Bizheva, A. Unterhuber, B. Hermann, H. Sattmann, A. F. Fercher, W. Drexler, A. Apolonski, W. J. Wadsworth, J. C. Knight, P. S. J. Russel, M. Vetterlein, and E. Scherzer, "Submicrometer axial resolution optical coherence tomography," *Opt. Lett.* **27**, 1800-1802 (2002).
- 8 G. J. Tearney, B. Bouma, and J. G. Fujimoto, "High-speed phase- and group-delay scanning with a grating-based phase control delay line," *Opt. Lett.* **22**, 1811-1813 (1997).
- 9 S. H. Yun, G. J. Tearney, B. E. Bouma, B. H. Park, J. F. deBoer, "High-speed spectral domain optical coherence tomography at 1.3 μm wavelength", *Opt Expr* **11**, 3598-3604 (2003).
- 10 G. J. Tearney, S. A. Boppart, B. Bouma, M. E. Brezinski, N. J. Weissman, J. F. Southern, and J. G. Fujimoto, "Scanning single-mode fiber optic catheter-endoscope for optical coherence tomography," *Opt. Lett.* **21**, 543-545 (1996).
- 11 J. M., Schmitt, S. H., Xiang, K. M., Yung, "Speckle in optical coherence tomography", *J. Biomed. Opt.*, **4**, 95-107, 1999
- 12 J. M. Schmitt and G. Kumar, "Turbulent nature of refractive index variation in biological tissue", *Opt Lett* **21**, 1310-1312 (1996).
- 13 Ed. A. J. Welch and M. J. C. van Gemert, *Optical-thermal response of laser-irradiated tissue*. (Plenum, New York: 1995).
- 14 Oregon medical laser center website, <http://omlc.ogi.edu>.
- 15 C. C. Cheng and M. G. Raymer, "Propagation of transverse optical coherence in random multiple-scattering media," *Phys. Rev. A* **62**, 1-12 (2000).
- 16 A. Ishimaru. *Wave propagation and scattering in random media* (IEEE Press, New Jersey, 1997).
- 17 PW Atkins, *Physical Chemistry* (W.H. Freeman and Co., 1978)
- 18 D. J. Griffiths, *Introduction to Electrodynamics*, Third Edition (Prentice Hall, New Jersey, 1999).
- 19 H.T. Yura and L. Thrane, personal communication, 2003.
- 20 J. M. Schmitt, A. Knüttel, and R. F. Bonner, Measurement of optical properties of biological tissues by low-coherence reflectometry, *Appl. Opt.* **32**, 6032-6042 (1993).
- 21 J. M. Schmitt, A. Knüttel, M. Yadlowsky, and M. A. Eckhaus, "Optical-coherence tomography of a dense tissue: statistics of attenuation and backscattering," *Phys. Med. Biol.* **39**, 1705-1720 (1994).
- 22 L. Thrane, H. T. Yura, and P. E. Andersen, "Analysis of optical coherence tomography systems based on the extended Huygens-Fresnel principle," *J. Opt. Soc. Am. A* **17**, 484-490 (2000).
- 23 M. J. Yadlowsky, J. M. Schmitt, and R. F. Bonner, "Multiple scattering in optical coherence microscopy", *Appl. Opt.* **34**, 5699-5707 (1995).
- 24 L. S. Dolin "A theory of optical coherence tomography", *Radiophys Quant Electr* **41**, 850-873 (1998).
- 25 Y. Pan, R. Birngruber, and R. Engelhardt, "Contrast limits of coherence-gated imaging in scattering media", *Appl. Opt.* **36**, 2979-2983 (1997).
- 26 D. J. Smithies, T. Lindmo, Z. Chen, S. Nelson, and T. E. Milner, "Signal attenuation and localization in optical coherence tomography studied by Monte Carlo simulations", *Phys Med Biol*, **43**, 3025-3044, (1998).
- 27 J. M. Schmitt and A. Knüttel, "Model of optical coherence tomography of heterogeneous tissue", *J. Opt. Soc. Am. A* **14**, 1231-1242 (1997).

-
- 28 I. Dror, A. Sandrov, and N. S. Kopeika, "Experimental investigation of the influence of the relative position of the scattering layer on image quality: The shower-curtain effect", *Appl Opt* **37**, 6495-6499 (1998).
- 29 H. T. Yura, "Signal-to-noise ratio of heterodyne lidar systems in the presence of atmospheric turbulence", *Opt. Acta* **26**, 627-644 (1979).
- 30 R. F. Lutomirski and H. T. Yura, "Propagation of a finite optical beam in an inhomogeneous medium," *Appl. Opt.* **10**, 1652-1658 (1971).
- 31 N. M. Shakhova, V. M. Gelikonov, V. A. Kamensky, R. V. Kuranov, and E. V. Turchin, "Clinical aspects of the endoscopic optical coherence tomography: a methods for improving the diagnostics efficiency," *Laser Physics* **12**, 23-32 (2002).
- 32 L. Thrane. *Optical coherence tomography: Modeling and applications*. PhD thesis. Risø National Laboratory (2001).
- 33 M. J. C. Van Gemert, S. L. Jacques, H. J. C. M. Sterenborg, and W. M. Star, "Skin optics", *IEEE Trans. Biomed. Eng.* **36**, 1146-1154 (1989).
- 34 A. E. Siegman, *Lasers* (University Science Books, Mill Valley, CA 1986).
- 35 D. Levitz, L. Thrane, M.H. Frosz, P. E. Andersen, C. B. Andersen, J. Valanciunaite, J. Swartling, S. Andersson-Engels, and P. R. Hansen. "Determination of optical scattering properties in highly-scattering media in optical coherence tomography images". *Opt Expr.* **12**, 249-259 (2004).
- 36 H. T. Yura, L. Thrane, and P. E. Andersen, "Closed form solution for the Wigner phase-space distribution function for diffuse reflection and small angle scattering in a random medium," *J. Opt. Soc. Am. A* **17**, 2464-2474 (2000).
- 37 A. M. Rollins and J. A. Izatt, "Optimal interferometer designs for optical coherence tomography," *Opt. Lett.* **24**, 1484-1486 (1999).
- 38 D. Levitz, C. B. Andersen, M. H. Frosz, L. Thrane, P. R. Hansen, T. M. Jørgensen, and P. E. Andersen "Assessing blood vessel abnormality via extracting scattering properties from OCT images" in European Conference in Biomedical Optics (ECBO), W. Drexler, ed. Proc. SPIE **5140**, 12-19 (2003).
- 39 R.C. Gonzales and R. L. Woods. *Digital Image Processing*, second edition (Prentice Hall, New Jersey: 2002).
- 40 W. H. Press, B.P. Flannery, S. A. Teukolsky, and W. T. Vetterling. *Numerical recipes in C: The art of scientific computing*, (Cambridge, New York: 1992).
- 41 Online Matlab documentation, 2004. www.mathworks.com.
- 42 A. Tycho, T. M. Jørgensen, H. T. Yura, and P. E. Andersen "Derivation of a Monte Carlo method for modeling heterodyne detection in optical coherence tomography systems" *Appl. Opt.* **41**, 6676-6691 (2002).
- 43 A. Tycho. *Optical coherence tomography: Monte Carlo simulation and improvement by optical amplification*. PhD thesis, Center for communications, optics and materials, (2002).
- 44 J. W. Pickering, S. A. Prahl, N. van Wieringen, J. F. Beek, H. J. C. M. Sterenborg, and M. J. C. van Gemert, "Double-integrating-sphere system for measuring the optical properties of tissue", *Appl Opt*, **32**, 399-410 (1993).
- 45 S. A. Prahl, Inverse Adding-Doubling Software. 1999. <http://omlc.ogi.edu/software/iad/index.html>.
- 46 M. Firbank and D. T. Delpy, "A design for a stable and reproducible phantom for use in near infra-red imaging and spectroscopy", *Phys Med Biol*, **38**, 847-853, (1993).
- 47 M. Firbank, M. Oda, and D. T. Delpy, "An improved design for a stable and reproducible phantom material for use in near-infrared spectroscopy and imaging", *Phys Med Biol*, **40**, 955-961, (1995).
- 48 J. Swartling, *Biomedical and atmospheric applications of optical spectroscopy in scattering media*. PhD Thesis, Lund Institute of Technology (2002).
- 49 J. Swartling, J. S. Dam, and S. Andersson-Engels, "Comparison of spatially and temporally resolved diffuse-reflectance measurement systems for determination of biomedical optical properties," *Appl. Opt.* **42**, 4612-4620 (2003).
- 50 A. Enejder, *Light scattering and absorption of tissue- models and measurements*. PhD Thesis, Lund Institute of Technology, 1997.
- 51 D. D. Royston, R. S. Poston, and S. A. Prahl, "Optical properties of scattering and absorbing materials used in the development of optical phantoms at 1064 nm," *J. Biomed. Opt.* **1**, 110-116 (1996).
- 52 L.-H. Wang, S. L. Jacques, and L.-Q. Zheng, "MCML -Monte Carlo modeling of photon transport in multi-layered tissues", *Comput Methods Programs Biomed*, **47**, 131-146, (1995).
- 53 MCML software on Oregon Medical Laser Center website, 1995. <http://omlc.ogi.edu/software/mc>

-
- 54 M. H. Kalos and P. A. Whitlock. *Monte Carlo methods I: Bascis*. (Wiley, New York: 1986).
- 55 L. Thrane, M. H. Frosz, T. M. Jørgensen, A. Tycho, H. T. Yura, and P. E. Andersen, "Extraction of optical scattering parameters and attenuation compensation in optical coherence tomography images of multi-layered tissue structures, *Opt. Lett.* (in press).
- 56 World Health Organization website, 2003, www.who.org.
- 57 M.J. Davies, "A macro and micro view of coronary vascular insult in ischemic heart disease", *Circulation* **82**, 38-46 (1990).
- 58 E. Falk, "Plaque rupture with severe pre-existing stenosis precipitating coronary thrombosis. Characteristics of coronary atherosclerotic plaques underlying fatal occlusive thrombi", *Br Heart J* **50**, 127-134 (1983).
- 59 R. Virmani, F. D. Kolodgie, A. P. Burke, A. Farb, S. M. Schwartz, "Lessons from sudden coronary death: a comprehensive morphological classification scheme for atherosclerotic lesions". *Arterioscler THromb Vasc Biol* **20**, 1262-1275 (2000).
- 60 American Heart Association website, 2004, www.americanheart.org.
- 61 I. K. Jang, B. E. Bouma, D. H. Kang, S. J. Park, S. W. Park, K. B. Seung, K. B. Choi, M. Shishkov, K. H. Schlendorf, E. Pomerantsev, S. L. Houser, H. T. Aretz, and G. J. Tearney, "Visualization of coronary atherosclerotic plaques in patients using optical coherence tomography: comparison with intravascular ultrasound," *J Am Coll Cardiol* **39**, 604-609 (2002).
- 62 H. Yabushita, B. E. Bouma, S. L. Houser, H. T. Aretz, I. K. Jang, K. H. Schlendorf, C. R. Kauffman, M. Shishkov, D. H. Kang, E. F. Halpern, and G. J. Tearney, "Characterization of human atherosclerosis by optical coherence tomography," *Circulation* **106**, 1640-1645 (2002).
- 63 G. J. Tearney, H. Yabushita, S. L. Houser, H. T. Aretz, I. K. Jang, K. H. Schlendorf, C. R. Kauffman, M. Shishkov, E. F. Halpern, and B. E. Bouma, "Quantification of macrophage content in atherosclerotic plaques by optical coherence tomography," *Circulation* **107**, 113-119 (2003).
- 64 B. E. Bouma, G. J. Tearney, H. Yabushita, M. Shishkov, C. R. Kauffman, D. DeJoseph Gauthier, B. D. MacNeill, S. L. Houser, H. T. Aretz, E. F. Halpern, and I. K. Jang, "Evaluation of intracoronary stenting by intravascular optical coherence tomography," *Heart* **89**, 317-321 (2003).
- 65 G. J. Tearney, H. Yabushita, S. L. Houser, H. T. Aretz, I. Jang, K. Schlendorf, C. R. Kauffman, M. S. Shishkov, E. F. Halpern, B. E. Bouma, "Optical coherence tomography provides accurate measurement of fibrous cap thicknesses in atherosclerotic plaques" in *Lasers in Surgery: Advanced Characterization, Therapeutics, and Systems XIII*, Ed. K. W. Gregory. Proc. SPIE **4949**, 2003.
- 66 J. W. Villard, M. D. Feldman, J. Kim, T. E. Milner, and G. L. Freeman, "Use of a Blood Substitute to Determine Instantaneous Murine Right Ventricular Thickening With Optical Coherence Tomography", *Circulation* **105**, 1843 – 1849 (2002).
- 67 H. T. Yura and S. G. Hanson, "Effects of receiver optics contamination on the performance of laser velocimeter systems", *J. Opt. Soc. Am. A* **13**, 1891-1902 (1996).
- 68 H. T. Yura and S. G. Hanson, "Optical beam wave propagation through complex optical systems", *J. Opt. Soc. Am. A* **4**, 1931-1948 (1987).
- 69 H. T. Yura, S. G. Hanson "Second-order statistics for wave propagation through complex optical systems", *J. Opt. Soc. Am. A* **6**, 564-575 (1989).
- 70 J. W. Goodman, *Statistical Optics*, (Wiley, New York: 1985).
- 71 E. Rubin and J.L. Farber, *Essential Pathology*, second edition, J. B. Lippincott Company, 1995.